

MAGNETIC RESONANCE IMAGING-BASED COMPUTATIONAL MODELS OF SOLID
TUMORS

By

GREGORY PISHKO

A DISSERTATION PRESENTED TO THE GRADUATE SCHOOL
OF THE UNIVERSITY OF FLORIDA IN PARTIAL FULFILLMENT
OF THE REQUIREMENTS FOR THE DEGREE OF
DOCTOR OF PHILOSOPHY

UNIVERSITY OF FLORIDA

2011

© 2011 Gregory Pishko

To my mom and dad

ACKNOWLEDGMENTS

There are so many people to acknowledge and thank. Most importantly, I would like to thank my parents for sacrificing and providing me everything that I needed to be where I am today. I appreciate all the support that my aunts, uncles, and cousins provided. My girlfriend provided me with a lot of emotional support and food to get me through some tough times.

As far as research goes, I would like to thank Dr. Malisa Sarntinoranont for giving me the opportunity to work in her lab with financial assistance. Garrett Astary deserves a very special thank you for his dedication to imaging mouse tumors with me—sometimes very late at night. Without his help this project would have not been possible. I would like to thank all of my lab mates that I've worked with over the past four and half years. An extra special thanks is deserved to Dr. Jung Hwan Kim, Sung Jin Lee, Magdoom Mohammed, and Jingya Zhang. I would like to extend a big thanks to my committee members: Dr. Brian Sorg, Dr. Hugh Fan, and Dr. Tran-Son-Tay. Additionally, I would like to thank Dr. Thomas Mareci for assistance with MR imaging, Marda Jorgensen at MBI Cell & Tissue Analysis Core (CTAC), and Dr. Dietmar Siemann and his lab: Dr. Lori Rice, Sharon Lepler, and Chris Pampo. The research in this dissertation was funded in part by the University of Florida's Research and Graduate Programs Opportunity Fund.

TABLE OF CONTENTS

	<u>page</u>
ACKNOWLEDGMENTS.....	4
LIST OF TABLES.....	7
LIST OF FIGURES.....	8
ABSTRACT	11
CHAPTER	
1 INTRODUCTION	13
1.1 Background.....	13
1.2 Previous Studies and Motivation.....	15
2 DEVELOPMENT AND SENSITIVITY ANALYSIS OF COMPUTATIONAL MODEL WITH HETEROGENEOUS VASCULATURE AND POROSITY	20
2.1 Introduction	20
2.2 Materials and Methods.....	24
2.2.1 Animal Preparation	24
2.2.2 Magnetic Resonance Imaging (MRI)	24
2.2.3 Vascular Permeability and Porosity Maps	25
2.2.4 3D Porous Media Model	27
2.2.5 Computational Model.....	30
2.2.6 Sensitivity Analysis	31
2.2.6.1 Hydraulic conductivity of tissue (K)	33
2.2.6.2 Vascular hydraulic permeability (L_p).....	34
2.2.6.3 Surface area per unit volume (S/V).....	35
2.2.6.4 Porosity (ϕ).....	36
2.2.6.5 Diffusion coefficient (D).....	36
2.3 Results.....	37
2.3.1 Interstitial Fluid Transport.....	37
2.3.2 Tracer Transport.....	39
2.4 Discussion and Conclusions	41
2.5 Acknowledgements.....	49
3 PATIENT-SPECIFIC COMPUTATIONAL MODELS OF SMALL SOLID TUMORS: A VALIDATION STUDY	61
3.1 Introduction	61
3.2 Materials and Methods.....	66
3.2.1 Animal Preparation	66
3.2.2 Magnetic Resonance Imaging (MRI)	66

3.2.3 Histology.....	68
3.2.4 Image Segmentation	69
3.2.5 Arterial Input Function, Vascular Permeability Maps, and Porosity Maps	69
3.2.6 3D Porous Media Mathematical and Computational Model.....	70
3.3 Results.....	72
3.3.1 Segmentation, Leakiness, and Histology.....	72
3.3.2 Interstitial Fluid Transport.....	73
3.3.3 Tracer Transport.....	73
3.4 Discussion and Conclusions	76
4 PATIENT-SPECIFIC COMPUTATIONAL MODELS OF LARGE SOLID TUMORS: AN EXPERIMENTAL COMPARISON	93
4.1 Introduction	93
4.2 Materials and Methods.....	96
4.2.1 Animal Preparation	96
4.2.2 Magnetic Resonance Imaging (MRI)	97
4.2.3 Histology.....	98
4.2.4 Image Segmentation	98
4.2.5 Arterial Input Function, Vascular Permeability Maps, and Porosity Maps	99
4.2.6 3D Porous Media Mathematical and Computational Model.....	99
4.3 Results.....	100
4.3.1 Segmentation, Leakiness, and Histology.....	100
4.3.2 Interstitial Fluid Transport.....	101
4.3.3 Tracer Transport.....	101
4.4 Discussion and Conclusions	104
5 CONCLUSIONS AND FUTURE WORK	115
LIST OF REFERENCES	121
BIOGRAPHICAL SKETCH.....	130

LIST OF TABLES

<u>Table</u>	<u>page</u>
2-1A Tissue and vascular parameters used in simulations	50
2-1B Tissue and vascular parameters used in simulations	50
2-2 Summary of chapter 2 sensitivity analysis	50
4-1 Dynamic contrast-enhanced magnetic resonance imaging parameters	106
4-2 Diffusion weighted imaging parameters.....	106

LIST OF FIGURES

<u>Figure</u>	<u>page</u>
1-1 Normal vs. tumor microvasculature	18
1-2 Examples of tumor necrosis	19
2-1 Block diagram of the mathematical methodology and experimental verification for the patient-specific tumor model.....	51
2-2 Geometric reconstruction of tumor and host tissue	52
2-3 Uptake and washout of average Gd-DTPA concentration, $C_{t,avg}(t)$, in tumor tissue at seven time points for the first 19 min.....	53
2-4. Signal enhancement in vessel and tumor periphery	54
2-5 Maps from slice 5 of MR data set of A) K^{trans} and B) ϕ with histograms.....	55
2-6 IFP sensitivity analysis for varying transport properties (Table 2-1B)	56
2-7 Tissue-averaged IFV sensitivity analysis for varying transport properties (Table 2-1B).....	57
2-8 Comparison of experimental and simulated Gd-DTPA distribution patterns in slice 5 for $t = 5, 30,$ and 60 min for baseline transport values in Table 2-1B.	58
2-9 Gd-DTPA distribution along bisecting tumor line at early, intermediate, and late time points	59
2-10 Gd-DTPA distribution along bisecting line through two additional KHT sarcomas.....	60
3-1 Orientation of MR slices with respect to the mouse anatomy (top view).....	81
3-2 CFD compatible meshes	82
3-4 Tumor segmentation of MRI data for small KHT sarcomas.....	83
3-5 H&E staining and example of estimating tumor area.....	84
3-6 Leakiness (K^{trans}) maps of small KHT sarcomas.....	85
3-7 Example of MECA-32 staining for KHT-3.	86
3-8 Interstitial fluid pressure for small KHT sarcomas.....	87
3-9 Interstitial fluid velocity for small KHT sarcomas.....	88

3-10	Comparison of simulated and experimental average Gd-DTPA in tumor	89
3-11	Comparison of error versus time quantified for simulations and experiment for KHT sarcomas.....	90
3-12	Simulated tracer transport for small KHT sarcoma (KHT-1).	91
3-13	Comparison of experimental and simulated concentration profiles across small KHT sarcomas	92
4-1	Tumor segmentation with corresponding H&E staining of small KHT sarcomas.....	107
4-2	H&E staining of large KHT sarcomas for A) KHT-4, B) KHT-5, C) KHT-6, and D) KHT-7	108
4-3	Example of MECA-32 staining for KHT-6	109
4-4	Leakiness (K^{trans}) maps of large KHT sarcomas.....	110
4-5	Interstitial fluid pressure for large KHT sarcomas.....	111
4-6	Interstitial fluid velocity for large KHT sarcomas.....	112
4-7	Experimental Gd-DTPA concentration, C_t , distribution in large KHT sarcomas at time equals 30 min.	113
4-8	Simulated tracer transport for large KHT sarcomas.....	114

LIST OF ABBREVIATIONS

ADC	Apparent Diffusion Coefficient
AIF	Arterial Input Function
CA	Contrast Agent
CFD	Computational Fluid Dynamics
DCE-MRI	Dynamic Contrast-Enhanced Magnetic Resonance Imaging
DTI	Diffusion Tensor Imaging
DWI	Diffusion-Weighted Imaging
Gd-DTPA	Gadolinium-Diethylene-Triamine Penta-Acetic Acid
IFP	Interstitial Fluid Pressure
IFV	Interstitial Fluid Velocity
MR	Magnetic Resonance
MW	Molecular Weight
SE	Spin Echo
TE	Time of Echo
TR	Time for Recovery

Abstract of Dissertation Presented to the Graduate School
of the University of Florida in Partial Fulfillment of the
Requirements for the Degree of Doctor of Philosophy

MAGNETIC RESONANCE IMAGING-BASED COMPUTATIONAL MODELS OF SOLID
TUMORS

By

Gregory Pishko

August 2011

Chair: Malisa Sarntinoranont
Major: Mechanical Engineering

The solid tumor environment is characterized by inherently unique heterogeneities. Specifically, tumors can have hyperpermeable, chaotic vessel networks that result in the non-uniform distribution of drug. These networks further restrict drug penetration by imposing a high pressure within the tumor due to increased efflux of plasma fluid. Regions of necrosis can play a role in reducing the uniformity of drug distribution since these regions tend to have altered tissue properties and lack vasculature.

The purpose of this study was to provide a methodology for an image-based computational model of a solid tumor that could be used to predict distribution of a tracer for specific tumors at three stages of tumor growth. Simulations were compared to experimental concentrations in tissue measured from magnetic resonance imaging (MRI).

First, an image-based computational model was developed that incorporates 3D maps of vascular leakiness and porosity for small non-necrotic murine KHT sarcomas with high leakiness ($n = 3$). Maps were constructed using early temporal MRI data ($t = 19$ min). These models provided descriptions of extravasation and delivery of an MR

visible tracer (Gd-DTPA) at later time points ($t = 1$ hr). A sensitivity analysis of the image-based computational model showed the high leakiness tumors to be dominated by transvascular exchange. The strength of the model to capture distribution of Gd-DTPA concentration within the tumor was demonstrated.

Second, the computational model was applied to small tumors with low leakiness for a validation study ($n = 3$). The low leakiness prevented the creation of porosity maps using early time points, so a constant porosity was assumed. The porous media model was determined to be a superior model to the two-compartment model for predicting uptake and washout behavior of average Gd-DTPA concentration in tumor. The porous media can account for the role of convection in tracer clearance in tumors with low leakiness.

Third, a computational model was developed to account for heterogeneous perfusion of Gd-DTPA due to both vasculature and fluid-filled, avascular necrotic regions within large, mature tumors ($n = 4$). The porous media model's ability to predict tracer transport was limited by the sparseness of the leakiness maps, which reduced the tracer sources in the model and complicated accurate prediction of transient behavior and distribution of Gd-DTPA. Because of the slow leakiness, DCE-MRI data can be collected at a lower temporal resolution and higher number of averages to provide more accurate mapping and transport predictions.

This study provided a framework for an MRI-based tumor model that predicts the heterogeneity of Gd-DTPA perfusion based on vasculature and necrosis for individual tumors. A predictive patient-specific computational model of solid tumors could be useful for individualized chemotherapeutic dose optimization and cardiotoxic limitation.

CHAPTER 1 INTRODUCTION

1.1 Background

Solid tumors describe a particular type of neoplasm that exist as firm tissue masses. The term “solid tumor” can take on a broad meaning, but often times it is used in reference to a particular cancerous disease that takes the form of a solid tumor such as breast, prostate, colon, or lung cancers. These cancers alone represent the estimated 712,100 of the 1,479,350 new cases and 277,280 of the 562,340 deaths in 2010 [1]. Because solid tumors represent a significant portion of cancer cases, more effective treatment could make a noticeable reduction of the negative impacts—emotional, physical, and financial—of cancer at large.

Solid tumors are understood to have transport obstacles that hinder systemically delivered drugs and can stymie the overall effectiveness of the treatment since it is difficult to deliver to all cells in a tumor. The inherent uniqueness of each tumor, created in part by tumor angiogenesis, compound treatment difficulties. Uniqueness can be witnessed with tumor angiogenesis, which is responsible for the creation of vessel networks that are abnormal when compared to vessel networks of healthy tissue (Figure 1-1). The abnormalities are marked by a disorganized vessel network as well as non-uniform microvascular permeability or vessel leakiness [2]. These abnormalities along with impaired lymphatic function are partly responsible for creating a macroscopically observable elevated tumor pressure. Elevated tumor pressures can work against drugs exiting the vessel and entering into the tissue en route to destroy cancer cells. While pressure in normal tissue is approximately 0 kPa, researchers have measured elevated intratumoral pressure [3-7] . Also, intratumoral pressure has been shown to vary within

a given tumor line. For example, Gutmann, R., et al. [6] found tumor pressure to range from 0.5 – 4.4 kPa in squamous cell carcinoma. Each tumor has unique microvascular blood flow, interstitial hydraulic conductivity, and interstitial matrix elasticity, which contribute to variations of intratumoral pressures [8]. Heldin et al. showed that high intratumoral pressure inhibited drug penetration [9]. Also, elevated tumor pressures have been shown to be predictors of disease progression after radiotherapy in patients with cervix cancer [8]. Long-term studies of cervical cancer have reported that intratumoral pressures have greater impact on predicting survival than tumor hypoxia (significantly lower cellular oxygen levels) [10].

It is necessary for tumor blood vessels to supply surrounding cells in solid tumors with proper nutrients. When the concentration of nutrients falls below a critical value, tumor cells can no longer remain viable. This can result in a region of necrosis within the tumor or an area where cells slowly swell and disintegrate. This process creates distinct regions of viable and necrotic cells within solid tumors (Figure 1-2). Essentially, these regions can become avascular in addition to the changes in the tissue matrix due to cellular alterations. Thus, many solid tumors exhibit tissue heterogeneity in addition to vascular heterogeneity.

Systemically delivered drugs are typically distributed non-uniformly due to the intricacies of the heterogeneous tumor environment. As mentioned earlier, high intratumoral pressure results in poor uptake. Regions closer to the tumor core, where interstitial pressure approaches the microvascular pressure, are more likely to exhibit poor uptake. In addition, tumor angiogenesis inherently creates non-uniform vessel density and leakiness, which increases the likelihood of non-uniform drug distribution.

Furthermore, necrotic regions can lack vasculature altogether and act as a reservoir for drugs, reducing the exposure of viable tumor cells to therapeutics. The extent of said non-uniformities can vary from patient to patient based on these phenomena. This dissertation focuses on incorporating these features into an image-based model.

1.2 Previous Studies and Motivation

Mathematical tumor models have provided the groundwork by which transvascular exchange, transport of interstitial fluid (extracellular plasma fluid), and transport of macromolecules can be noninvasively investigated. Macromolecular therapeutic agents such as monoclonal antibodies and encapsulated drugs have provided impetus for exploration of transport barriers in the tumor environment. For example, previous tumor models have been used to understand the role of increased interstitial pressure on the transport of three macromolecules of different sizes (IgG, F(ab')₂, and Fab) [11, 12]. In this porous media model, Baxter and Jain used an idealized spherical tumor geometry with homogeneous vessel density and leakiness properties to elucidate the difficulty of uniform macromolecular delivery.

Baxter and Jain accounted for heterogeneous tissue properties by including a necrotic core to study the case of a non-uniformly perfused tumor [13]. The tumor was modeled with a necrotic core that did not have a vascular network. Their model noted that a necrotic core had an effect on solute distribution of large, slow-diffusing molecules. One of the limitations of this model is its inability to capture vessel “hotspots”, where there might be leakier and more densely packed vessels. Though these models have corroborated experimental data and elucidated other tumor phenomena, they lack the ability to describe tumors on a patient-by-patient basis.

This dissertation focuses on the creation of a 3D computational tumor model to predict interstitial solute transport. The model essentially integrates more reality into solid tumor models than previously achieved by using an image-based approach. Reality is sought in the form of tissue boundaries as well as heterogeneous vessel and tissue properties. Magnetic resonance imaging (MRI) can be used to non-invasively acquire these properties for specific tumors, but there exists some limitations to obtaining heterogeneous vessel and tissue properties as the tumor grows and matures. Vascular remodeling can reduce the vessel leakiness (or permeability) over time and high fluid-filled regions can develop due to cell death at more advanced stages of tumor growth. In order to adapt the model to these scenarios, the model is investigated at three stages of tumor maturation: small tumors with high leakiness, small tumors with low leakiness, and large tumors with low leakiness and necrosis. Additionally, reduced vessel leakiness may increase the importance of interstitial convection and diffusion relative to transvascular exchange of systemically injected solute. This results from transvascular exchange occurring over a much longer time scale when vessel permeability is low.

Vessel and tissue properties are obtained via dynamic MRI data. It is the goal of this dissertation to use less than 20 minutes of the MRI data to acquire model inputs: heterogeneous permeability of vessels and extracellular volume fraction of the tissue. These inputs acquired from early time point data are used to predict solute distribution with the 3D computational model at later time points. For small high leakiness tumors, MRI can be used to account for both spatially varying permeability of the vessels and extracellular volume fraction of the tissue. Further along in tumor development, the

remodeled vasculature may result in less permeable vessels. At this stage only spatially varying permeability can be obtained and a constant extracellular volume fraction must be assumed. In more advanced tumors with necrosis, only spatially varying permeability can be obtained due to the low leakiness of the tumor. However, high fluid-filled regions can be detected with MRI and can be accounted for in the 3D porous media model as regions of higher diffusivity and extracellular volume fraction. It is necessary to investigate the model throughout these stages in order to develop a model that can be used for these typical tumor environments. Doing this will improve upon previous tumor models by creating a methodology of a range of realistic tumor environments thereby providing a framework by which drug doses could be individualized based on a patient's specific tumor environment.

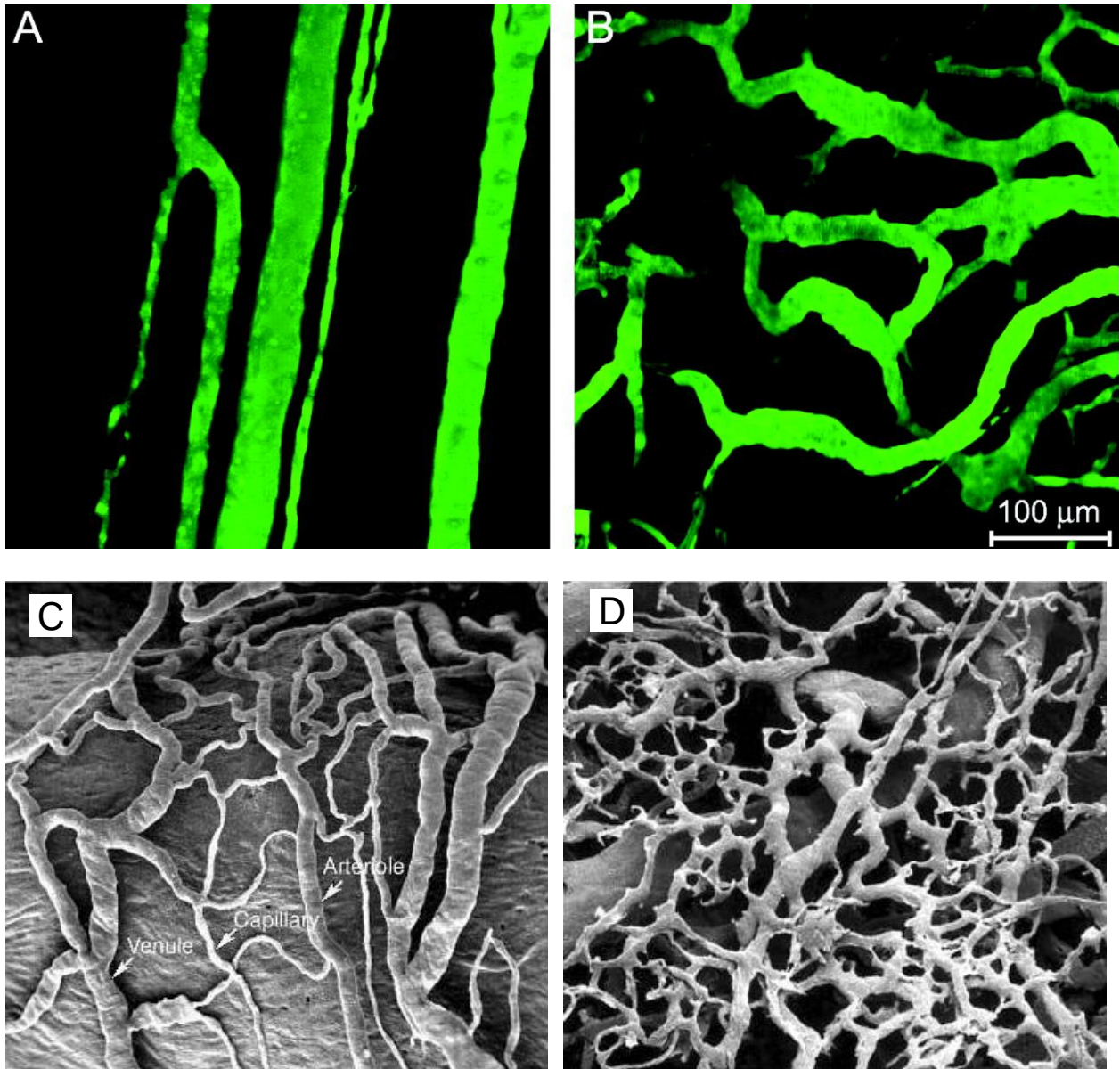


Figure 1-1. Normal vs. tumor microvasculature. A) Normal microvasculature is organized with relatively constant vessel diameter. B) Tumor vasculature is marked by disorganization, chaotic branches and varying diameter [2]. SEM corrosion cast of C) normal microvasculature and D) tumor microvasculature [14].

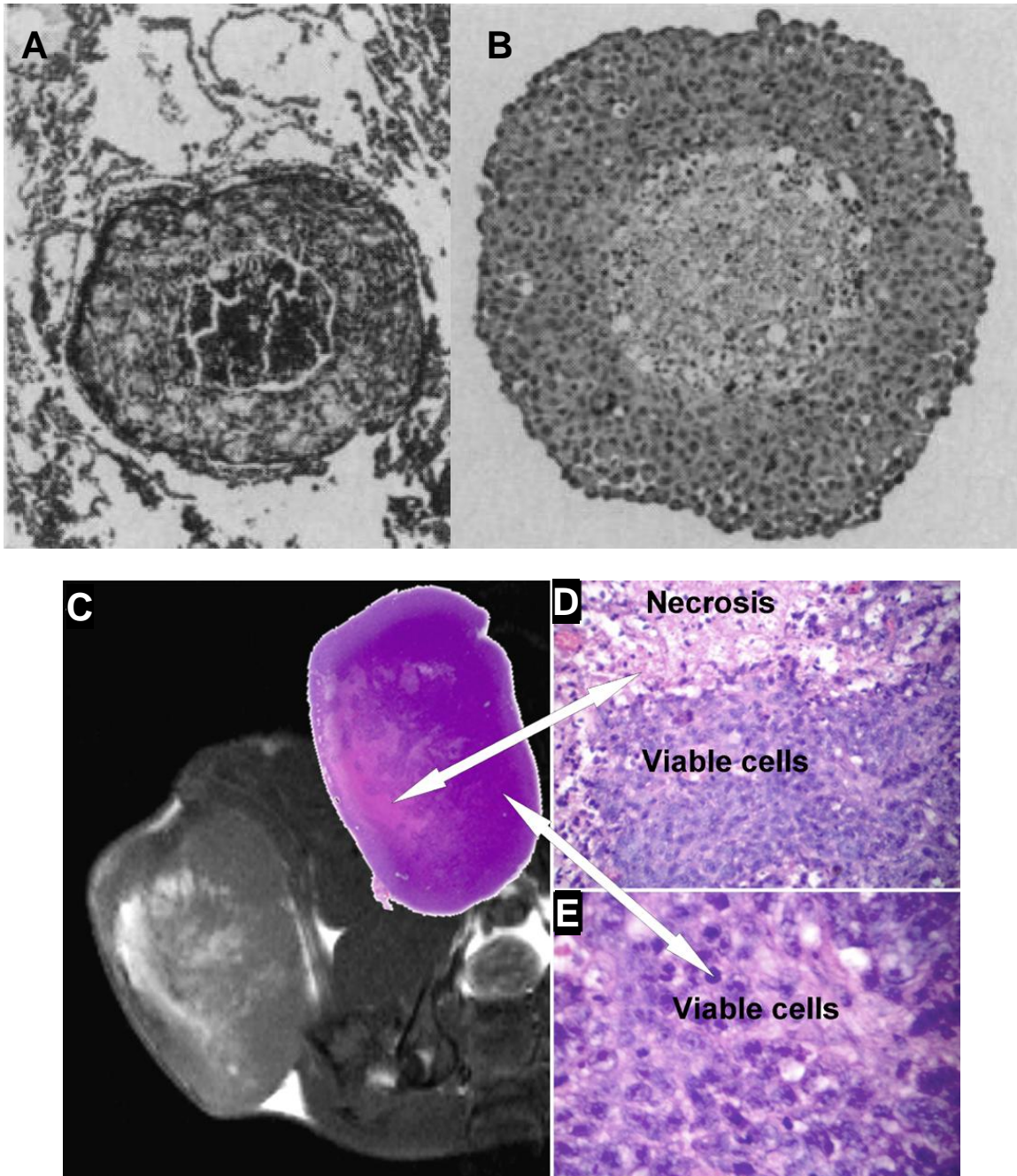


Figure 1-2. Examples of tumor necrosis. A) Necrosis surrounded by well-vascularized site of 1.5 mm human adenocarcinoma of colon. B) Histological section through center of CaSki spheroid that shows viable rim surrounding necrotic center [13]. C) MR image of tumor that shows heterogeneous uptake. D) A region with necrosis and a high concentration of viable cells. E) Viable cells well outside the necrotic region [14].

CHAPTER 2 DEVELOPMENT AND SENSITIVITY ANALYSIS OF COMPUTATIONAL MODEL WITH HETEROGENEOUS VASCULATURE AND POROSITY

2.1 Introduction

Solid tumors are understood to have transport obstacles that hinder systemic delivery of drugs and can stymie the overall effectiveness of treatment, since it is difficult to deliver drugs to all cells in a tumor [15]. The inherent uniqueness and heterogeneity of each tumor vascular network, created in part by tumor angiogenesis, compound treatment difficulties. Tumor angiogenesis is responsible for the creation of vessel networks that are abnormal when compared to networks in healthy tissue. The abnormalities are marked by a disorganized vessel network, as well as non-uniform microvascular permeability or vessel leakiness [2]. In this dissertation and commonly in literature, permeability and leakiness are synonymous. These abnormalities along with impaired lymphatic function are partly responsible for creating an elevated interstitial internal tumor pressure. Elevated tumor pressures can work against drugs exiting blood vessels and entering into the parenchyma en route to destroy cancer cells. Furthermore, each tumor has unique microvascular blood flow, interstitial hydraulic conductivity, and interstitial matrix elasticity, which contribute additionally to variations of intratumoral pressures and flows [8]. The net result is heterogeneous extravasation and distribution of therapeutic agents into tissue, dependent upon specific tumor environments, following systemic injection.

Early mathematical tumor models have provided the groundwork by which transvascular exchange, transport of interstitial fluid (extracellular plasma fluid), and transport of macromolecules can be noninvasively investigated. For example, tumor models have been used to understand the role of interstitial pressure on the transport of

a systemically delivered solute [12, 13]. Baxter and Jain (1989) used a continuum porous media approach to tumor tissue to solve interstitial and solute transport (IgG, F(ab')₂, and Fab). Solving for an idealized spherical tumor, they found elevated interstitial fluid pressure (IFP) to be a significant barrier: (1) elevated IFP reduced the driving force for extravasation of fluid and macromolecules in tumors; (2) spatially-varying IFP resulted in non-uniform filtration of fluid and macromolecules from blood vessels; (3) elevated IFP lead to an experimentally verifiable, radially outward interstitial fluid velocity (IFV) which opposes the inward diffusion of interstitial solute such as tracers, macromolecules, or drugs [11, 12].

Other researchers have further investigated tumor models using a continuum approach. El-Kareh and Secomb studied the effects of uniformly increased vessel permeability on transport of macromolecules within a spherical tumor geometry [16]. In later studies, Baxter and Jain expanded upon their own spherical tumor model by including a necrotic core without functioning vessels [13]. The goal was to establish a more realistic case of a non-uniformly perfused tumor by including the concept of heterogeneous tissue properties. They found that the necrotic core did not reduce the central interstitial pressure in the tumor and had an effect on solute distribution of large, slow-diffusing molecules.

Mathematical descriptions of tumor transport have been adapted to numerous treatment situations and have shown the potential to impact clinical practices. Eikenberry modeled delivery of doxorubicin to a solid tumor comprised of multiple tumor cords and showed the potential for predictability of dose efficacy and cardiotoxicity [17]. Smith and Humphrey elucidated the role of transvascular exchange during the

administration of drug via intratumoral convective-enhanced delivery (CED) [18]. Their model suggested that transvascular exchange reduction procedures would increase convective flow thereby aiding infusion therapies.

Recent computational fluid dynamics (CFD) approaches to tumor drug delivery, by integrating more patient specificity with the aid of medical imaging data, have created a new realm of personalized clinical possibilities. Tan, et al. used patient MRI data to reconstruct the 3D geometry of a resected brain region where the main part of the tumor was removed [19]. In this simulation, the resected region was implanted with poly (lactide-co-glycolide) (PLGA) wafers loaded with 1% Etanidazole. Elevated pressure was predicted in the resected region, as well as in the remaining tumor tissue. Our group has also presented an image-based model, which includes *in vivo* heterogeneous vasculature data since the extent of vessel non-uniformity can vary from patient to patient [20]. This current study has two aims: (1) to expand upon the CFD modeling approach by incorporating spatially variable tissue porosity (volume fraction of extracellular extravascular space (EES) over total tissue volume) in addition to variable vessel permeability and (2) to compare simulated tracer distribution to experimental concentration data derived from MRI.

In this study, heterogeneous tissue and vascular properties are modeled by incorporating spatially-varying porosity and vascular permeability maps created from two-compartment analysis of early-time point (19 min) dynamic contrast-enhanced (DCE) -MRI data. DCE-MRI allows signal enhancement measurements of MR contrast agent (CA) uptake and washout in the KHT sarcoma-bearing hind limbs of mice ($n = 3$). This chapter looks at small sarcomas with highly permeable vessels. Signal

enhancement was measured following the systemic delivery of the low molecular weight, extracellular CA, gadolinium-diethylenetriamine pentaacetic acid (Gd-DTPA), and was used to quantify concentration of Gd-DTPA in tumor and healthy tissue in each voxel of MR data on a voxel-by-voxel basis. Porosity and permeability maps, derived from these data, were incorporated into a 3D porous media model to predict interstitial fluid and tracer transport in tumor and host tissue at later time points. A sensitivity analysis was conducted based on a range of literature values using the data of one mouse: (1) to select an arterial input function (AIF) (the time-dependent CA concentration in arterial blood plasma) based on consistency of the first 19 min of experimental and simulated tracer transport and (2) to investigate the effects of baseline tissue and vascular transport properties on interstitial fluid and tracer transport. The optimal AIF and baseline transport properties were used to simulate interstitial fluid and tracer transport for two additional KHT sarcomas. Magnitude and distribution of experimental and simulated tracer concentration in tumor was compared for all three tumors.

An image-based solid tumor model may be used to optimize and evaluate treatment strategies for patient-specific therapies. The computational model presented here provides the necessary first steps toward that application. First, the simulation of CA uptake and washout in the tumor environment provides a foundation from which the model can be expanded to investigate transport of reactive drugs. Second, sensitivity analyses of these models provide a better understanding of the underlying transport processes and the effects of vascular and tissue properties within realistic tumor

geometry. Third, by comparing simulations to experimental data, elements of the tumor model can be refined to create more accurate image-based models of drug delivery.

Content in this chapter is based on a paper submitted to the *Annals of Biomedical Engineering* in collaboration with Garrett Astarly (Department of Biomedical Engineering), Thomas Mareci (Department of Biochemistry and Molecular Biology), and Malisa Sarntinoranont (Department of Mechanical and Aerospace Engineering).

2.2 Materials and Methods

2.2.1 Animal Preparation

Animal models provide means to investigate *in vivo* systemic delivery of CA and create permeability and porosity maps. The patient-specific model was based on three C3H female mouse (Jackson Laboratories, Bar Harbor, ME) that was inoculated with 10^5 murine KHT sarcoma cells in the gastrocnemius muscle. Tumors were grown for 7 days to a hind limb diameter between 6.0–7.5 mm. During imaging, mice were anesthetized using a gas mixture of 98% oxygen, 2% isoflurane and given a $0.1\text{--}0.2$ mmol kg⁻¹ of body weight (bw) bolus tail vein injection of Gd-DTPA (Omniscan, GE Healthcare Inc., Princeton, NJ) CA at a constant rate (~ 0.4 mL min⁻¹, 0.23 mL). Animal experiments were performed within the principles of the Guide for the Care and Use of Laboratory Animals and approved by the University of Florida Institutional Animal Care and Use Committee (IACUC).

2.2.2 Magnetic Resonance Imaging (MRI)

The MRI experiment was performed using a Bruker Avance imaging console (Bruker NMR Instruments, Billerica, MA) connected to Magnex Scientific 11.1 T horizontal bore magnet system (Varian, Inc., Magnex Scientific Products, Walnut Creek California). The hind limb of the mouse was placed in a 1.5 cm inside diameter, transmit

and receive, volume coil. Multiple T_2 -weighted spin echo (SE) scans (TR = 2000 ms, TE = 15, 30, 45, 60 and 75 ms) were acquired for the calculation of T_2 values. Tumor boundaries could be manually segmented for each slice [21]. Segmented images were used for geometric reconstruction of the tumor and host tissue volumes. A variable time for recovery (TR) SE sequence (TR = 5000, 2000, 1000, 500 and 250 ms, TE = 15 ms, field of view (FOV) = 2 cm × 1 cm × 1 cm, 11 slices, matrix size = 192 × 96, 2 averages 2), was acquired for calculation of native tissue T_1 values used in CA concentration calculations. Serial DCE-MR images, consisting of T_1 -weighted SE sequence (TR/TE = 330 ms/9.4 ms, FOV = 2 cm × 1 cm × 1 cm, 11 slices, matrix = 192 × 96, NA = 6, total acquisition time = 2 min 6 s) were collected before and after CA administration. T_1 -weighted SE sequence with a short TE was used to avoid noise in the measured signal that can occur under hypoxic conditions [22] with sequences sensitive to T_2 effects.

2.2.3 Vascular Permeability and Porosity Maps

Vascular leakiness was described using endothelial transfer coefficient (K^{trans}) values. K^{trans} values were estimated using a two-compartment model approach, where the two compartments are the blood plasma and EES. From DCE-MRI data, K^{trans} values were quantified on a voxel-by-voxel basis by: (1) estimating CA concentration in tissue via the relationship between concentration and signal intensity [23] and (2) using a Tofts and Kermode model to fit to the CA kinetics within the first 19 min. Previous DCE-MRI data showed that peak tissue concentration was reached within 5 min post-injection for fast enhancing breast tumor ($K^{\text{trans}} > 0.1 \text{ min}^{-1}$) and that this time window was acceptable to properly fit K^{trans} [24]. The 19-minute time window was chosen for our study because of slower enhancing peripheral tumor tissue (peak time at ~17 min). It was assumed that change in CA concentration in tissue is dominated by a fast

transvascular exchange at early time points. Though, over longer time scales interstitial convection and diffusion may play an important role in the distribution of CA within the tumor space requiring a continuum approach to make accurate predictions.

A linear relationship between contrast agent concentration and T_1 was assumed. An average of the pre-contrast images was used to solve for baseline (pre-injection) signal values, and the transverse-relaxation contribution to signal was assumed to be unity. Then, concentrations of Gd-DTPA in tissue were solved at each time point using the standard spin-echo signal equation [23]

$$C_t = \frac{1}{R_1} \left[\frac{1}{TR} \ln \frac{S(0)}{S(0) - S(C_t) \cdot (1 - e^{-TR/T_{10}})} - \frac{1}{T_{10}} \right] \quad (2-1)$$

C_t is the volume-averaged tissue concentration of Gd-DTPA determined by MRI; R_1 is the longitudinal relaxivity of the contrast agent; TR is the recovery time; T_{10} is the relaxation time without contrast agent; $S(C_t)$ and $S(0)$ are signal intensities at CA concentrations C_t and zero respectively; TR, T_{10} , $S(0)$, and $S(C_t)$ are known values; and R_1 was approximated as $2.7 \text{ L mmol}^{-1} \text{ s}^{-1}$ (based on Gd-DTPA relaxivity in rat muscle [25] at 6.3 T).

Tofts-Kermode two-compartment model [26] incorporates basic physiological phenomena to describe the transport of systemically injected contrast agents into tissue space. The two-compartment model can be described by

$$\frac{dC_t}{dt} = K^{\text{trans}} C_p - \frac{K^{\text{trans}}}{\phi} C_t \quad (2-2)$$

where t is time; C_p is the AIF that describes the time course of Gd-DTPA concentration in the blood plasma; ϕ is the volume fraction of EES or porosity (also

referred to as v_e in tumor perfusion studies). The volume fraction of plasma in each voxel was assumed small compared to ϕ . Transvascular transport of Gd-DTPA solely into the EES at early post-infusion times was assumed. C_p following a bolus injection was represented by a biexponential decay [26] that was normalized:

$$C_p(t) = d \left[a_1 e^{-m_1 t} + a_2 e^{-m_2 t} \right] \quad (2-3)$$

where a_1 and m_1 represent the amplitude and rate constant, respectively, of the fast equilibrium between plasma and extracellular space; a_2 and m_2 represent the amplitude and rate constant of the slow component of the clearance; d is the dose of the bolus injection. Solving Equation 2-2 by substitution of Equation 2-3 in terms of concentration of CA in tissue, C_t , produces

$$C_t(t) = K^{\text{trans}} d \left\{ \frac{a_1}{\frac{K^{\text{trans}}}{\phi} - m_1} e^{-m_1 t} + \frac{a_2}{\frac{K^{\text{trans}}}{\phi} - m_2} e^{-m_2 t} - \left(\frac{a_1}{\frac{K^{\text{trans}}}{\phi} - m_1} + \frac{a_2}{\frac{K^{\text{trans}}}{\phi} - m_2} \right) e^{-\frac{K^{\text{trans}}}{\phi} t} \right\} \quad (2-4)$$

MR experimental concentrations determined by Equation 2-1 were used to fit Equation 2-4 in order to solve K^{trans} and ϕ at each voxel within the tumor boundary to generate 3D maps. K^{trans} and ϕ parameters were fit using a nonlinear regression in MATLAB (MATLAB Version 7.1, The MathWorks, Inc., Natick, MA). Only physically relevant ranges were considered ($K^{\text{trans}} \geq 0$ and $0 \leq \phi \leq 1$) where $R^2 > 0.5$. Values of K^{trans} were set to zero and $\phi = 0.3$ in voxels where the fit was poor ($R^2 \leq 0.5$). This occurred in ~5% of voxels within the tumor.

2.2.4 3D Porous Media Model

The 3D porous media tumor model accounts for the CA-distribution time dependence on the underlying plasma flow and diffusion within the interstitial space of

tissue. Each point in space in this porous media model contains a tissue and vascular component. The vascular components provide a source or sink for both plasma fluid and tracer per unit tissue volume. The filtration rate of plasma fluid per unit volume (J_v/V) across the vessel wall is described by Starling's law [12]

$$\frac{J_v}{V} = L_p \frac{S}{V} (p_v - p_i - \sigma_T (\pi_v - \pi_i)) \quad (2-5)$$

where L_p is the vessel permeability, S/V is microvascular surface area per unit volume, p_v is the microvascular pressure, p_i is the IFP, σ_T is the average osmotic reflection for plasma protein, π_v is osmotic pressure in microvasculature, and π_i is osmotic pressure in interstitial space. Since we were interested in capturing vascular heterogeneity, it was necessary to include vessels that were non-uniformly permeable to both plasma fluid and CA. K^{trans} values directly describe the leakiness of vessels to CA. In order to account for heterogeneous plasma fluid leakiness, K^{trans} values were normalized by the average K^{trans} within the tumor, \bar{K}^{trans} , and this normalized value was used to scale J_v/V in order account for plasma leakiness heterogeneities. This was done assuming that patterns of leakiness are similar for both tracer and plasma fluid.

The tissue continuum was modeled as a porous media. In tissue, the continuity equation [12] and Darcy's law were used to solve IFP and tissue-averaged IFV (\mathbf{v}) and were given by

$$\nabla \cdot \mathbf{v} = \frac{K^{\text{trans}}}{\bar{K}^{\text{trans}}} \frac{J_v}{V} - L_{pL} \frac{S_L}{V} (p_i - p_L) \quad (2-6)$$

and

$$\mathbf{v} = -K \nabla p_i, \quad (2-7)$$

respectively. The first term on the right hand side of Equation 2-6 describes a volumetric source due to the vasculature; the second term on the right hand side is a sink due to lymphatic vessels. $L_{pL}S_L/V$ is the lymphatic filtration coefficient, p_L is pressure in the lymphatic vessels, and K is the tissue hydraulic conductivity. Lymphatic function was assumed in host tissue only with $p_L = 0$ kPa. Darcy's law is commonly applied to tumors, perfused muscle tissues, and flow in soft connective tissues [27]. K is small in these types of tissues such that the role of viscosity is more important at the fluid-solid interface of the porous media than within the fluid.

Transport of interstitial Gd-DTPA was solved using the convection and diffusion equation for porous media [28]:

$$\frac{\partial C_t}{\partial t} + \frac{\mathbf{v}}{\phi} \cdot \nabla C_t - D_{\text{eff}} \nabla^2 C_t = K^{\text{trans}} \left(C_p - \frac{C_t}{\phi} \right) - \frac{L_{pL}S_L}{V} (p_i - p_L) \frac{C_t}{\phi} \quad (2-8)$$

where D_{eff} is the effective diffusion coefficient for Gd-DTPA in tissue. The second and third term on the left describe convective flux and diffusive flux, respectively. The transvascular source term on the right is a modified form of the Kedem-Katchalsky equation where diffusion dominates the transfer of solute across the microvessel wall; the sink term on the right accounts for lymphatic drainage of solute in normal tissue.

A block diagram (Figure 2-1) shows the flow of the mathematical methodology and experimental comparison, which attempts to summarize the fundamental goals of the chapter: 1) test the sensitivity of interstitial fluid transport (Equations 2-6 and 2-7) to changes in interstitial fluid transport parameters, 2) test the sensitivity of tracer transport (Equation 2-8) to changes in tracer transport parameters, and 3) compare the simulated tracer transport results with experimental tracer measurements. The first step in accomplishing these goals was to obtain DCE-MRI signal enhancement data for *in vivo*

tumor. That provided *in vivo* Gd-DTPA concentration in tissue over the course of the experiment (60 min) using Equation 2-1. The first 19 min of the data was used to select an AIF from a range of common literature AIFs (slow, intermediate, and fast). The model relies on this input, which described the decay of Gd-DTPA concentration in the blood plasma following a bolus systemic injection over time using Equation 2-3. This function can affect the magnitude and distribution of K^{trans} and ϕ maps, which in turn affects interstitial fluid and tracer transport. The first 19 min of average concentration of simulated Gd-DTPA in tumor (tracer transport) was compared with its experimental counterpart. The slow AIF provided the most consistent results between simulated and experimental average concentration of Gd-DTPA in tumor; therefore, this AIF was used in the sensitivity analysis of Equations 2-6, 2-7, and 2-8. The results of modeled tracer transport (Equation 2-8) was compared with experimental tracer transport by comparing 1) Gd-DTPA distribution along a line bisecting the tumor at early ($t = 5$ min), intermediate ($t = 30$ min), and later ($t = 60$ min) time points, and 2) uptake and washout of average Gd-DTPA within the tumor.

2.2.5 Computational Model

From MR slices, tumor and hind limb geometries were manually segmented (MATLAB v.7, Natick, MA) based on contrast differences in T_2 values (Figure 2-2A). Triangulated mesh surfaces were generated to create tumor and host tissue boundaries (Amira 4.1.1, San Diego, CA) and were converted to parametric representation, non-uniform rational B-spline surfaces (NURBS) (Geomagic Studio, Research Triangle Park, NC). Meshes for the volumes of host tissue and tumor were created (Gambit, Fluent, Lebanon, NH; Figure 2-2B). The meshes were composed of $\sim 2,700,000$ 4-node

tetrahedral elements. The large number of elements aided the porous media solver with convergence for solutions with steep pressure gradients at the tumor boundary in the CFD software package (FLUENT 6.3, Fluent, Lebanon, NH).

Prediction of tumor tracer distribution was a two-step process. First, steady-state interstitial plasma fluid flow was solved (Equation 2-6). Then, tracer transport (Equation 2-8) was solved over 1 h. Boundary conditions were such that the solute was assumed to exit at the cut ends at the same rate as the interstitial plasma fluid. Additionally, the skin boundary was assumed to be impermeable to tracer and plasma while the cut ends of the leg were considered far enough away from the tumor boundary and therefore set to a normal tissue pressure [6, 11], $p_i = 0$ kPa. Initial tissue concentration was zero for the tracer solution.

2.2.6 Sensitivity Analysis

The model was dependent on vascular and tissue transport parameters, and AIF. In this chapter, animal-specific AIF was not known, so a sensitivity of AIF using three test cases from literature was first conducted to determine a model AIF that best represents the experiments AIF. Simulated average tracer uptake and washout in the tumor is compared to experiment for the three test cases. The modeled AIF that provided similar average tracer uptake and washout in the tumor to experimental observation was selected as the AIF in the interstitial transport sensitivity analysis (Equations 2-6, 2-7, & 2-8). In the interstitial transport analysis, known vascular and tissue transport parameters (L_p , K , $L_{pL}S_L/V$, D_{eff} , and initial concentration of Gd-DTPA in blood plasma) were varied to determine the effects on unknowns: interstitial pressure (p_i) and velocity (\mathbf{v}). Values in Table 2-1A were considered known values and used for all simulations; these values were not varied in the sensitivity analysis. Some of these

values were selected based on the model presented by Baxter and Jain (1989); these particular parameters are not well measured in literature and are often used by other models of interstitial flow within tumors [19, 20, 29]. Table 2-1B contains the nominal baseline values for the sensitivity analysis that were selected based on or near the ranges obtained from literature.

Three AIFs were considered in order to estimate the time course of CA concentration in blood plasma: a fast decay [30] where $a_1 = 9.2 \text{ kg bw L}^{-1}$, $a_2 = 4.2 \text{ kg bw L}^{-1}$, $m_1 = 0.004 \text{ s}^{-1}$, and $m_2 = 0.0008 \text{ s}^{-1}$; an intermediate decay [31] where $a_1 = 13.0 \text{ kg bw L}^{-1}$, $a_2 = 16.0 \text{ kg bw L}^{-1}$, $m_1 = 0.005 \text{ s}^{-1}$, and $m_2 = 0.00043 \text{ s}^{-1}$; a slow decay [26, 32] where $a_1 = 4.0 \text{ kg bw L}^{-1}$, $a_2 = 4.8 \text{ kg bw L}^{-1}$, $m_1 = 0.002 \text{ s}^{-1}$, and $m_2 = 0.0002 \text{ s}^{-1}$. Given that dose was 0.2 mmol kg^{-1} , a_1 and a_2 were scaled so that $C_p(t=0)$, C_{p0} , was 2.0 mM based on the dilution calculation (from the measured concentration of the bolus injection of Gd-DTPA and the estimated blood volume of the mouse based on body weight) [33]. K^{trans} and ϕ maps were created for each AIF and used to simulate interstitial fluid flow and the first 19 min of tracer transport. The slow AIF was selected for the sensitivity analysis because the average Gd-DTPA concentration in tumor tissue, $C_{t,\text{avg}}$, behavior was most similar to the experimental data (Figure 2-3). K^{trans} and ϕ maps created based on the slow AIF were used for sensitivity analysis (Figure 2-5).

Other parameters of interest in this sensitivity analysis were as follows: tumor vessel permeability ($L_{p,t}$), normal tissue permeability ($L_{p,n}$), $L_{pL}S_L/V$, D_{eff} , and ratio of tumor hydraulic conductivity to normal tissue hydraulic conductivity (K_t/K_n). K_t/K_n was chosen to account for the relative difference in hydraulic conductivity of normal and tumor tissue as measured experimentally. C_{p0} was also analyzed to observe the effects

of over- or under-estimating this value. Sensitivity analysis was conducted by using high and low values with respect to the baseline values. Permeability, $L_{pL}S_L/V$, and K_t/K_n values were set such that the high case was 2 × baseline and the low case was 0.5 × baseline. D_{eff} were set such that high case 10^1 × baseline and low case was 10^{-1} × baseline. The high case for C_{p0} was 2.5 mM and low case was 1.5 mM.

2.2.6.1 Hydraulic conductivity of tissue (K)

Hydraulic conductivity describes the ease at which a fluid can pass through a saturated porous material. The hydraulic conductivity of several types of tumors as well as various types of healthy tissue has been experimentally measured.

Tumor tissue (K_t). Hydraulic conductivity has been found to vary across tumor lines, within a specific tumor line, and can depend on the experimental setup. The values for tumor tissue range from 1×10^{-15} to 1×10^{-12} m²/Pa-s. In a 1D experiment using a permeability chamber ($P = 392$ to 8332 Pa) with one O-ring, K_t was measured to be 1.8×10^{-13} m²/Pa-s in human colon adenocarcinoma (LS174T) [34]. For the same tumor line, $K_t = 1.3 \times 10^{-13}$ to 2.3×10^{-13} m²/Pa-s in a low flow rate experiment with in vivo flow rates of 0.1 to 0.14 μ l/min [35]. Netti and cohorts found $K_t = 3.9 \times 10^{-13}$ m²/Pa-s in vitro for LS174T [36]. K_t for rat fibrosarcoma MCA-R tissue ex vivo was found to be 1.0×10^{-14} m²/Pa-s for a pressure of 2000 Pa [37]. In a 1D experiment using a permeability chamber ($P = 392$ to 8332 Pa) with one O-ring, Morris hepatoma 5123 tissue found $K_t = 3.0 \times 10^{-14}$ m²/Pa-s. They also found $K_t = 3.0 \times 10^{-15}$ to 8.0×10^{-15} m²/Pa-s for the same tumor line with in vivo data using an unsteady flow model [15]. Dog squamous cell carcinoma was K_t found to be 1.8×10^{-12} m²/Pa-s [38]. Rat hepatocarcinoma tissue in vitro and in vivo found K_t to be m²/Pa-s [39]. Netti et al.

completed a series of experiments to determine K_t of multiple tumor lines. K_t was estimated from the transient stress relaxation rate using a poroviscoelastic model. Each specimen was compressed 25 μm in ramps of 15 s and allowed to relax for 20 min. For human soft tissue sarcoma (STS-26T), $K_t = 7 \times 10^{-14} \text{ m}^2/\text{Pa}\cdot\text{s}$; for mouse mammary carcinoma (MCA-IV), $K_t = 1.9 \times 10^{-12} \text{ m}^2/\text{Pa}\cdot\text{s}$; for human glioblastoma (U87), $K_t = 4.9 \times 10^{-13} \text{ m}^2/\text{Pa}\cdot\text{s}$ [36].

Healthy tissue (K_n). The values for healthy tissue hydraulic conductivity range from 1.5×10^{-15} to $1.8 \times 10^{-12} \text{ m}^2/\text{Pa}\cdot\text{s}$. Hydraulic conductivity in rat stratum corneum (outer most layer of the epidermis) was measured to be $6.4 \times 10^{-15} \text{ m}^2/\text{Pa}\cdot\text{s}$ [15]. Zakaria et al. measured K_n by applying an interstitial pressure gradient across unsupported abdominal wall muscle over a pressure range: 200 Pa ($K_n = 1.1 \times 10^{-13} \text{ m}^2/\text{Pa}\cdot\text{s}$) to 1066 Pa ($K_n = 5.9 \times 10^{-13} \text{ m}^2/\text{Pa}\cdot\text{s}$) [40]. K_n for *in vivo* subcutaneous connective tissue was measured to be $1.8 \times 10^{-12} \text{ m}^2/\text{Pa}\cdot\text{s}$ [41]. Fleischman et al. noted K_n as low as $1.5 \times 10^{-15} \text{ m}^2/\text{Pa}\cdot\text{s}$ [42].

2.2.6.2 Vascular hydraulic permeability (L_p)

Vascular hydraulic permeability describes the transvascular filtration rate of plasma. Measurements of vascular hydraulic permeability are less extensive than hydraulic conductivity of tissue.

Tumor vascular hydraulic permeability ($L_{p,t}$). Vessels from rat mammary adenocarcinoma (R3230AC) tumors were measured by Sevick and Jain. This was accomplished by directly measuring capillary filtration coefficient along with vascular surface area to back out the values of $L_{p,t}$ between 1.0×10^{-10} and $3.5 \times 10^{-10} \text{ m}^2/\text{Pa}\cdot\text{s}$

[43]. Jain et al. measured $L_{p,t}$ of mouse mammary carcinoma MCalV vessels to be 1.9×10^{-10} m/Pa-s [44].

Healthy vascular hydraulic permeability ($L_{p,n}$). In a normal vessel whole organ experiment for rabbit, $L_{p,n}$ was measured to be 0.78×10^{-13} m/Pa-s [45]. In a normal vessel whole organ experiment for human, $L_{p,n}$ was measured to be 0.726×10^{-13} m/Pa-s [46]. A normal vessel single frog pial microvessel $L_{p\sigma}$ was fitted to a monoexponential function that described rising dye concentration within occluded segment. The fit provided $L_{p,n} = 2.06 \times 10^{-13}$ m/Pa-s [47]. Permeability for normal single rat brain vessels was measured by Kimura et al. [48]. Specifically, they measured the volume flux of water per unit surface area across the arteriole wall occluded vessel. Pressures were varied from 2666 Pa to 9333 Pa. L_p was derived from slope of J_v/S versus applied pressure. They found: mean $L_p = 13.5 \times 10^{-13}$ m/Pa-s and median $L_p = 6.0 \times 10^{-13}$ m/Pa-s [48]. Normal capillaries in skeletal muscle of rats was found: $L_p = 2.7 \times 10^{-12}$ m/Pa-s [49]. Lymph vessel rat mesenteric postcapillary venules were cannulated with micropipettes attached to a water manometer to control hydrostatic perfusion to find $L_p = 3.6 \times 10^{-11}$ [50].

2.2.6.3 Surface area per unit volume (S/V)

Surface area per unit volume is purely a dimensional quantity, which is calculated as the vessel surface area to volume of vessel contained within the surface area.

One of the earliest studies of this parameter found S/V of peripheral capillary membranes to be 7000 m^{-1} [51]. For vessels in human brain tissue, S/V was found to be 6000 — 14000 m^{-1} [52]. S/V was found to be 5700 m^{-1} and 19000 m^{-1} in white and grey matter, respectively [46]. Murine mammary carcinomas C3H/Bi small tumors (0.035

cm³) S/V was measured to be 26500 m⁻¹ and 15000 m⁻¹ for large tumors (>0.5 cm³) [53]. S/V for human colon adenocarcinoma (LS174T) *in vivo* was measured at 24000 m⁻¹ [54].

2.2.6.4 Porosity (ϕ)

Porosity is a dimensionless quantity that describes the fraction of void space in a representative volume. It is exactly calculated as the volume of void space over the total volume of the representative volume. While porosity was not explicitly a part of this sensitivity analysis, the literature search provides some context for the values obtained using DCE-MRI in this chapter.

Porosity of renal allograft interstitial fibrosis was established by using a histomorphometric method. Approximately 200 points were randomly selected in a field for each biopsy. Ratio of overlying interstitium points were then calculated and ranged from 0.1 to 0.6 [55]. Using a DCE-MRI approach with a two-compartment model porosity was found to be 0.28 in MDA PCa 2b tumor and 0.16 in skeletal muscle [56]. For normal rat brain tissue, mean ϕ was measured to be between 0.20 and 0.22 [57]. Porosity in muscle tissue was measured to be 0.08 using DCE-MRI methods [58, 59].

2.2.6.5 Diffusion coefficient (D)

The diffusion coefficient is a constant of proportionality that describes the transport of molecules (solute) through an area due to Brownian motion with a driving force that is the concentration gradient of solute.

Diffusion coefficient for Gd-DTPA in healthy human articular cartilage was measured to be 1.4×10^{-10} m²/s [60]. For a tissue surrogate, 10% PVA-C hydrogel, D for Gd-DTPA was measured to be 2.6×10^{-10} m²/s [61].

2.3 Results

2.3.1 Interstitial Fluid Transport

The solution of Equations 2-6 and 2-7 results in interstitial fluid transport; this provides two unknowns, p_i and \mathbf{v} , throughout tissue space. For the baseline simulation of interstitial fluid transport, pressure was predicted to be higher within the tumor than outside the tumor. The pressure contour in Figure 2-6A shows higher IFP ($p_{i, \max} = 1.4$ kPa) within the tumor than the surrounding host tissue for the baseline simulation. Pressure varied within the tumor from 0.86 kPa at the boundary to 1.4 kPa in the tumor core (slightly skewed towards the left from mid-tumor in Figure 2-6A). The pressure fell sharply ($|\Delta p_{i, \max}| = 0.79$ kPa mm⁻¹) at the tumor boundaries Figure 2-6B. Outward flow of interstitial fluid from the tumor was observed (Figure 2-7A). The magnitude of volume-averaged fluid velocity was predicted to be highest at or near the boundary of the tumor 0.59 $\mu\text{m s}^{-1}$ and 0.41 $\mu\text{m s}^{-1}$ at both ends of the bisecting line (Figure 2-7A & Figure 2-7B). Approximately 1 mm into the host tissue, fluid velocity was reduced by 75% to 0.1 $\mu\text{m s}^{-1}$ and continued to decrease to the cut ends (~ 0.03 $\mu\text{m s}^{-1}$).

In both the high and low cases of the sensitivity analysis, interstitial hypertension was observed within the tumor with a decrease in pressure at the tumor-tissue interface (Figure 2-6B). The high $L_{p,t}$, $L_{p,n}$, and low $L_{pL} S_L/V$, K_t/K_n cases all resulted in intratumoral pressures that were greater than the baseline simulation. Percentage increase in intratumoral pressures from the baseline was highest for the high $L_{p,t}$ case. Decreases in the pressure gradient at the tumor-tissue interface from the baseline simulation were observed in the low K_t/K_n , $L_{pL} S_L/V$, $L_{p,t}$ and high $L_{p,n}$ cases. The low $L_{p,t}$ and high K_t/K_n resulted in a flattening of intratumoral IFP profile. Percent difference in intratumoral

pressure and pressure gradient at the tumor-tissue interface for all cases with respect to the baseline deviations are calculated in Table 2-2.

Volume-averaged velocity of interstitial fluid was predicted to be highest near the boundary of the tumor in all cases of the sensitivity analysis (Figure 2-7B). Volume-averaged velocity at the boundary was reduced by > 100% near the cut ends in all cases. High $L_{p,t}$, K_t/K_n and $L_{p,n}$, and low $L_{p,n}$ and K_t/K_n cases all resulted in tumor boundary tissue-averaged IFVs that were greater than the baseline simulation. The highest increase in velocity was witnessed for the high $L_{p,t}$ case, which corresponded to a peak volume-averaged velocity of $\sim 0.8 \mu\text{m s}^{-1}$ at the tumor-tissue interface. $L_{p,n}$ had little effect on the velocity at the tumor boundary (< 2 % difference from baseline).

Tumor vessel permeability, $L_{p,t}$, had the greatest impact on the interstitial fluid solution. Changes in $L_{p,t}$ resulted in a >30% difference from the baseline when looking at three behaviors: intratumoral pressure, tumor-tissue pressure gradient, and magnitude of velocity at the tumor-tissue interface. Normal vessel permeability, $L_{p,n}$, was the least sensitive parameter in terms of impact on the interstitial fluid solution. Though the low and high C_{p0} cases resulted in respectively higher and lower K^{trans} values than the baseline (within the tumor), interstitial fluid transport for the low and high C_{p0} cases was identical to the baseline.

Baseline simulations for the two additional KHT sarcomas resulted in lower interstitial peak pressures (0.50–0.75 kPa) and boundary pressure gradients ($|\Delta p_{1,\text{max}}| = 0.15 \text{ kPa mm}^{-1}$) than the data set used for the sensitivity analysis; however, the pressure distribution pattern was similar. Subsequently, outward flow of interstitial fluid

was observed with the highest magnitude of volume-averaged fluid velocity near the boundary of the tumor ($0.35 \mu\text{m s}^{-1}$).

2.3.2 Tracer Transport

The effect of AIF upon average Gd-DTPA concentration, $C_{t,avg}(t)$, in tumor tissue was examined and compared to experimental data obtained from MRI for the first 19 min (Figure 2-3). Three simulations of tracer transport were conducted which corresponded to three AIFs. The aim was to determine the best AIF based on agreement between experimental and simulated $C_{t,avg}(t)$ behavior at early time points. The simulated curves showed higher peak concentration than the MR measured concentration. Peak concentrations were 11%, 30%, and 30% higher than the experimental peak for slow, intermediate, and fast respectively. Assuming monoexponential decay for the tumor volume-averaged washout behavior, decay rates were as follows: -0.029 min^{-1} (experimental), -0.050 min^{-1} (fast), -0.034 min^{-1} (slow), and -0.045 min^{-1} (intermediate). The slow AIF produced peak concentration and washout behavior in tumor similar to experimental observation (Figure 2-4). Signal enhancement in the lateral marginal vein (Figure 2-4A) was detected in one preliminary data set (mouse with xenografted renal cell carcinoma). The vessel was indicated by high signal enhancement ($>500\%$) in the first scan after the bolus injection of contrast agent in the serial DCE-MR imaging sequence (Figure 2-4B). The transient behavior of signal enhancement in this ROI showed to be similar to the biexponential decay of the slow AIF. This clearance behavior was quite different from the behavior seen in fast enhancing, high uptake regions in the tumor periphery (Figure 2-4C).

The baseline simulation showed increased Gd-DTPA deposition on the left half of the tumor (Figure 2-8), which corresponded to the leakier, left side of the tumor (Figure

2-5A). Clearance of Gd-DTPA due to transvascular exchange was observed in the tumor from 5 to 60 min. Tracer transport simulations showed qualitative spatial distribution and transient behavior similar to that of the experimental data. Also, tracer transport was less sensitive than interstitial fluid transport to changes in model parameters in Table 2-1B (Figure 2-9). However, tracer transport was sensitive to changes in C_{p0} .

Considerable overlap along the bisecting tumor line was observed for the baseline simulation and simulations of high and low model parameters from Table 2-1B (Figure 2-9). The consistency of the distribution pattern along the tumor line resulted in a high Pearson product-moment correlation coefficient (PMCC), r , for all simulated cases ($r > 0.99$ for $t = 5, 30, 60$ min). Concentration deviations from the baseline within the tumor were estimated; root mean squared (RMS) errors, ε , were found to be small for all cases ($0.03 \times 10^{-5} \text{ mM} < \varepsilon < 4.4 \times 10^{-5} \text{ mM}$), but for the high and low C_{p0} cases ($80 \times 10^{-5} \text{ mM} < \varepsilon < 260 \times 10^{-5} \text{ mM}$) over the 1 hr simulation (Table 2-3). The high and low C_{p0} cases along the tumor line resulted in C_t lower and higher than the baseline case at $t = 5$ min, respectively. High and low $L_{p,t}$, $L_{p,n}$, $L_{pL}S_L/V$, K_t/K_n and D_{eff} cases exhibited a similar washout behavior to $C_{t,\text{avg}}(t)$ of the baseline case ($\sim -0.03 \text{ min}^{-1}$). Variations in experimental and numerical error made it difficult to correlate the small changes in ε to relative sensitivity for the tissue and vascular parameters.

The results of the sensitivity analysis showed agreement between simulated and experimental C_t for the first 30 min ($\varepsilon = 0.46 \times 10^{-3} \text{ mM}$ at $t = 5$ min; $\varepsilon = 0.58 \times 10^{-3} \text{ mM}$ at $t = 30$ min) for all cases but high and low C_{p0} ($1.8 \times 10^{-3} \text{ mM} < \varepsilon < 3.9 \times 10^{-3} \text{ mM}$). At $t = 60$ min, all cases over-predicted C_t ($0.5 \times 10^{-3} \text{ mM} < \varepsilon < 1.8 \times 10^{-3} \text{ mM}$) within the

tumor (Figure 2-9C). Even though C_t was over-predicted, sensitivity analysis simulations showed similar patterns of Gd-DTPA concentration distribution to experimental patterns ($r > 0.89$) within the tumor. Including the host tissue in the correlation reduced $r = 0.42$ at $t = 60$ min. This was due to later peak C_t (> 17 min) in the experimental data observed at two regions of the host tissue (2-3 mm and 16-20 mm; Figure 2-9).

Because tracer transport was less sensitive to changes in transport parameters, baseline values were used to predict transport in the two additional KHT sarcomas (Figure 2-10). Similar simulated and experimental distribution patterns of Gd-DTPA concentration were observed at $t = 5$ and 30 min ($r > 0.78$) within the tumor (Figure 2-10A–D); however, the correlation in the tumor was not as strong ($r > 0.58$) at $t = 60$ min (Figure 2-10E–F). Magnitude of simulated Gd-DTPA concentration along the bisecting line through a tumor was greater than experimental magnitudes at $t = 60$ min ($0.5 \times 10^{-3} < \varepsilon < 2.1 \times 10^{-3}$ mM; Figure 2-10E–F). Furthermore, the average Gd-DTPA concentration within the entire tumor volume for the simulations were greater than experiments at $t = 60$ min for all three tumors. The largest percent difference of average Gd-DTPA concentration within the tumor volume (700%) occurred in the tumor shown in Figure 2-10B–F. Relative concentration error was $< 38\%$ in the other two tumors. The results of the sensitivity analysis in chapter 2 have been summarized in Table 2-2.

2.4 Discussion and Conclusions

This study presents the first image-based tumor model, with both heterogeneous vasculature and tissue porosity, which predicts interstitial fluid and solute transport within tissue. The model exhibits two important interstitial transport characteristics: it predicts interstitial hypertension, and increased velocities at the host tissue-tumor interface. A high correlation was observed ($r > 0.89$) between predicted and

experimental spatial deposition of Gd-DTPA along a bisecting line within the tumor after 1 h in the tumor used to develop the model. Also, transient behavior (washout rates) of Gd-DTPA in the tumor showed good agreement between the simulation and experiment. The two additional KHT sarcomas used to test the developed model showed varied outcomes in terms of predicting the average concentration of Gd-DTPA at 1 h. Namely, experimental and simulated concentration distribution and magnitude correlated well for one modeled tumor while errors were significant in the other.

In previous studies, intratumoral IFP has been investigated and hypertension has been simulated [12, 19, 20, 62] and measured [3-7]. IFP values have been shown to vary within a tumor line and to be proportional to tumor volume by Gutmann et al. [6]. In their study, a pressure range of 0.5 – 4.4 kPa for squamous cell carcinomas was observed. The baseline intratumoral pressure simulated in this image-based model fell within the low end of this range. This could be in part due to tumor size. The tumor volumes in the current study were smaller (~95%) than the non-metastatic smallest tumors investigated by Gutmann's group. In our model, a smaller tumor would be expected to have a lower intratumoral IFP. Smaller tumors have fewer vessels than larger tumors so they have fewer available fluid sources. Previous models of idealized tumors predicted increased velocities at the tumor boundary [63]. For an isolated tumor with a diameter of 2 cm, fluid velocity at the boundary was approximately $0.1\text{--}0.2 \mu\text{m s}^{-1}$. In the presented model, velocity at tumor boundary in the baseline simulation was predicted to be higher ($0.35\text{--}0.60 \mu\text{m s}^{-1}$).

It should be noted that solute transport in this study was limited to a low molecular weight MR visible tracer, Gd-DTPA. The transport of low molecular weight tracers is

less likely to be convective when compared to macromolecular tracers or therapeutic agents. Despite these limitations, image-based models using Gd-DTPA as an interstitial tracer offers a few advantages: (1) DCE-MRI using Gd-DTPA is well understood, documented, and it is a clinically used approach to understand the tumor environment; (2) DCE-MRI using Gd-DTPA provides qualitative and quantitative (e.g., vascular leakiness maps) data; (3) Gd-DTPA is similar molecular weight to some chemotherapeutic drugs (e.g. doxorubicin = 543 g mol⁻¹); (4) Gd-DTPA extravasates more effectively than macromolecules and does not bind, hence it provides a best case scenario for the evaluation of smaller macromolecular drug transport.

For solute transport simulations, the model presented in this study exhibited a similar extent of heterogeneity (70–80% difference in maximum and minimum concentrations) at early time points (5–6 min) along a bisecting tumor line as a previous Gd-DTPA transport model from our group [20]. However, there are two markedly different tracer transport behaviors between our two studies. In the previous study, along the entire extent of the bisecting tumor line, Gd-DTPA concentration increased and the concentration profile flattened over the course of 30 min. The current study observed an overall decrease across the bisecting line for this same time course and a less dramatic flattening. These differences are due to improvements upon the previous model that were the result of three key refinements made in the present model: (1) a faster decaying AIF than the previous model provided for transvascular sink terms during the first 30 min of the simulation; (2) the incorporation of both spatially varying porosity and K^{trans} allowed for more finely tuned kinetic behavior than the previous fixed

porosity model; (3) lower effective diffusivity contributed to less dramatic flattening of the tracer concentration profile.

The sensitivity analysis pointed out aspects of the model—parameters, source terms, and measurements—that most effect transport. This knowledge can be used to simplify the model by reducing the number of input parameters. Also, the sensitivity analysis was conducted with *a priori* knowledge of the experimental data. This allowed the investigation of changes in model parameters with respect to the experimental concentration data, which made it possible to measure model error and indicate possible reasons for the error.

Interstitial fluid flow was most sensitive to vessel permeability with $L_{p,t}$ having the most profound impact on IFP and boundary fluid velocity. These permeability values scale pressure differences that exist across vessel walls and directly affect volumetric source and sink terms of the continuity equation. Non-invasive, patient-specific measurements of $L_{p,t}$ might be necessary in order to make more accurate predictions of intratumoral pressure and tumor boundary convection using an image-based modeling approach. Alternatively, non-invasive measurements of IFP distribution in tumors [64] could be imported into this model to better estimate transport parameters such as $L_{p,t}$ and calculate transport. With the validation of predicted intratumoral IFP, these models could be used to predict disease progression after radiotherapy in patients with cervix cancer [65]. Long-term studies of cervical cancer have reported that intratumoral pressures have greater impact on predicting survival than tumor hypoxia [10].

Gd-DTPA tracer transport was relatively insensitive to changes in vascular and tissue transport parameters. When modeling low molecular weight tracers or drugs in smaller tumors (~6–7 days for KHT sarcoma cells), it is likely that tracer transport is dominated by transvascular exchange, rather than convection or diffusion, at the simulated time scale. In the case of transvascular exchange-dominated tumors, accurate AIF and C_{p0} measurements are the most important parameters for accurate prediction of concentration in tissue at later time points. For larger tumors, this may not be the case due to the increase of tumor tissue heterogeneity, which will occur as the tumor develops necrotic regions. Because the transvascular exchange term is dominant, due to the frequency of high K^{trans} ($\geq 0.1 \text{ min}^{-1}$) values in the tumor, it might not be important to have a continuum porous media approach which accounts for convection and diffusion in the interstitial space of smaller high leakiness tumors at the simulated time scale; a two-compartment model may suffice (Equation 2-2). However, it should be noted that the low average porosity in all three tumors (~0.1) could have masked the role of convection and diffusion. It has been suggested by other researchers that low porosity values (< 0.2) in the tumor obtained from DCE-MRI may be indicative of convective tracer clearance and not physiologically low extracellular volume fraction [64]. A continuum porous media approach is likely necessary to model cases of lower leakiness where the transvascular exchange term is less dominant and porosity values less obtainable using early DCE-MRI time points. In these cases diffusion and convection can have greater impact on interstitial molecules and porosity values would have to be obtained DCE-MRI independent methods or fixed. Moreover,

the continuum model would be necessary to model transport of macromolecular agents that require convective transport over smaller time scales.

The insensitivity of vascular and tissue transport parameters resulted in no considerable spatial changes in time, yet temporal and spatial distribution of baseline simulation and experiment Gd-DTPA in tissue was comparable. This underscores the importance of spatially heterogeneous leakiness and porosity in the transvascular exchange mechanism for solute transport in patient-specific tumor models as well as proper estimation of baseline C_{p0} . The low and high C_{p0} case illustrated the importance of proper dose measurement. There are two potential sources of error, which can lead to incorrect estimation of original values of C_{p0} . First, Omniscan Gd-DTPA is highly concentrated (287 mg mL^{-1}) and requires a ~ 30 -fold dilution for one dose. Second, the mouse blood volume per weight requires estimations based on the mean literature value from a range of values ($63\text{--}80 \text{ mL kg}^{-1}$). For example, the combination of these two factors could lead to an over-estimation of C_{p0} if Gd-DTPA is over-diluted and/or the actual mouse blood volume per weight is greater than the estimated mean value. When comparing predicted concentrations with MR data, it should be noted that sources of error also exist in the MRI-derived *in vivo* concentration values. R_1 , which inversely scales the concentration estimated from MRI, was based a literature value that was measured in rat muscle at 6.3 T. This could be a direct source of error when comparing magnitudes of simulated (baseline) and experimental concentration, if the actual R_1 varies from implemented literature value. Also, concentration measurements are dependent upon T_{10} maps that were created by fitting a monoexponential curve to 5 data points measured from a variable TR SE sequence. Errors can occur from the fit as

well as motion between TRs. Motion was minimal since movement was not observed between scans. Additionally, there is background noise that comes from all of the electrical components used for imaging. The background noise can lead to less accurate measurements of low concentrations (< 0.01 mM). Furthermore, the noise has the potential to reduce the number of properly K^{trans} fitted voxels, which happened infrequently ($< 5\%$ of tumor voxels).

Another limitation of the model was the use of an AIF based on literature values. This potentially lowers the patient specificity of the model. In this study, AIF was selected from a range of literature values based on a comparison of simulated and experimental transient behavior of $C_{t,\text{avg}}(t)$ in tumor tissue at early time points. Though the slow AIF resulted in an acceptable correlation for one data set, it may not have been the experimental AIF for all data sets. This fact was likely the cause of the large simulated and experimental concentration discrepancies at later time points seen in Figure 2-10B–F. K^{trans} magnitudes and patterns, to a lesser degree, can be altered based on the type of AIF used. This could lead to variations of tracer deposition, since K^{trans} is essentially a kinetic parameter that drives the tracer transport source term. In the future, more accurate models can be obtained by measuring patient-specific AIFs to create more accurate 3D K^{trans} and ϕ maps, as well as source terms in tracer transport which include a C_p term.

The image-based patient-specific framework of this study offers opportunities to fine-tune the model for a variety of applications. The model can be adjusted to incorporate a wider variety of tumor environments. For example, the image-based model can be expanded to include necrotic regions. A larger range of uptake and

washout behaviors can be observed in larger necrotic tumors which cannot be characterized by K^{trans} and ϕ used in the standard two-compartment model [66]. In addition, diffusion-weighted imaging could be used to detect regions of increased diffusion, which have been shown to be correlated with regions of necrosis [67-69]. These regions can be modeled as avascular and highly diffusive porous regions within the framework of the presented computational model. Additional patient-specificity can be captured with tensorial descriptions of K and D_{eff} to account for preferential interstitial fluid and tracer transport. This method has been employed to predict transport in central nervous system tissue with the aid of diffusion tensor imaging [70-72]. The prediction of patient-specific interstitial fluid flow could also be incorporated into a multiscale model to predict shear stresses on tumor cells within the extracellular matrix. Brinkman's equation can be used instead of Darcy's law to solve momentum in the tumor microenvironment because it allows for a no-slip boundary condition [73]. Since shear stresses on tumor cells have been found to induce a G₂/M cell cycle arrest and inhibit cell differentiation [74], tissue remodeling could potentially be predicted with this type of multiscale model. In order to predict transport of a therapeutic drug, the model could also be expanded to account for binding and degradation of drug by including a rate of binding term in the tracer transport equation. The model presented in this study could account for binding or degradation of extravasated solute with the knowledge of its degradation constant in tissue, β [19]. For example, a first-order elimination term, βC_t , can be subtracted from the right-hand side of Equation 2-8.

2.5 Acknowledgements

We would like to thank Dr. Dietmar Siemann, Dr. Lori Rice, and Chris Pampo for providing the murine KHT sarcoma cells and tumor inoculation. This research was funded by the University of Florida's Research and Graduate Programs Opportunity Fund. MR data was obtained at the Advanced Magnetic Resonance Imaging and Spectroscopy facility in the McKnight Brain Institute of the University of Florida.

Table 2-1A. Tissue and vascular parameters used in simulations

Variable	Parameter	Value
S/V (m^{-1})	Microvascular surface area per unit volume	20000 ^t ; 7000 ⁿ [12, 19]
p_V (Pa)	Microvascular pressure	2300 [75] 3230 ^t [76]; 1330 ⁿ [12, 19]
π_i (Pa)	Osmotic pressure in interstitial space	2670 [76]
π_V (Pa)	Osmotic pressure in microvasculature	2670 [76]
σ_T	Average osmotic reflection coefficient for plasma	0.82 ^t ; 0.91 ⁿ [12, 13]

Table 2-1B. Tissue and vascular parameters used in simulations

Variable	Parameter	Value	Literature range
L_p ($m Pa^{-1} s^{-1}$)	Vessel permeability	2×10^{-11} ^t 3×10^{-12} ⁿ	2.1×10^{-11} [3] – 3.5×10^{-10} [42] ^t 7.3×10^{-14} [36] – 3.6×10^{-11} [50] ⁿ
$L_{pL} S_L / V$ ($Pa^{-1} s^{-1}$)	Lymphatic filtration coefficient	1×10^{-7}	8×10^{-8} – 2×10^{-6} [4]
K ($m^2 Pa^{-1} s^{-1}$)	Hydraulic conductivity	1.9×10^{-12} ^t 3.8×10^{-13} ⁿ	7.0×10^{-14} [35] – 1.8×10^{-12} [20] ^t 6.4×10^{-15} [45] – 1.8×10^{-12} [21] ⁿ
D_{eff} ($m^2 s^{-1}$)	Effective coefficient of diffusion	1×10^{-9}	6.9×10^{-9} [15] – 2.6×10^{-10} [18]

t: tumor tissue; n: normal host tissue

Table 2-2. Summary of chapter 2 sensitivity analysis

Parameter	Pressure	Boundary Velocity	Concentration
$L_{p,t}$	Increase	Increase	No change
$L_{p,n}$	No change	No change	No change
$L_{pL} S_L / V$	Decrease	Increase	No change
K_t / K_n	Decrease	Increase	No change
C_{p0}	No change	No change	Decrease
D_{eff}	No change	No change	No change

The table describes the result of pressure, boundary velocity, and concentration within the tumor (increase, decrease, or no change) due to an increase in the parameter from the baseline value.

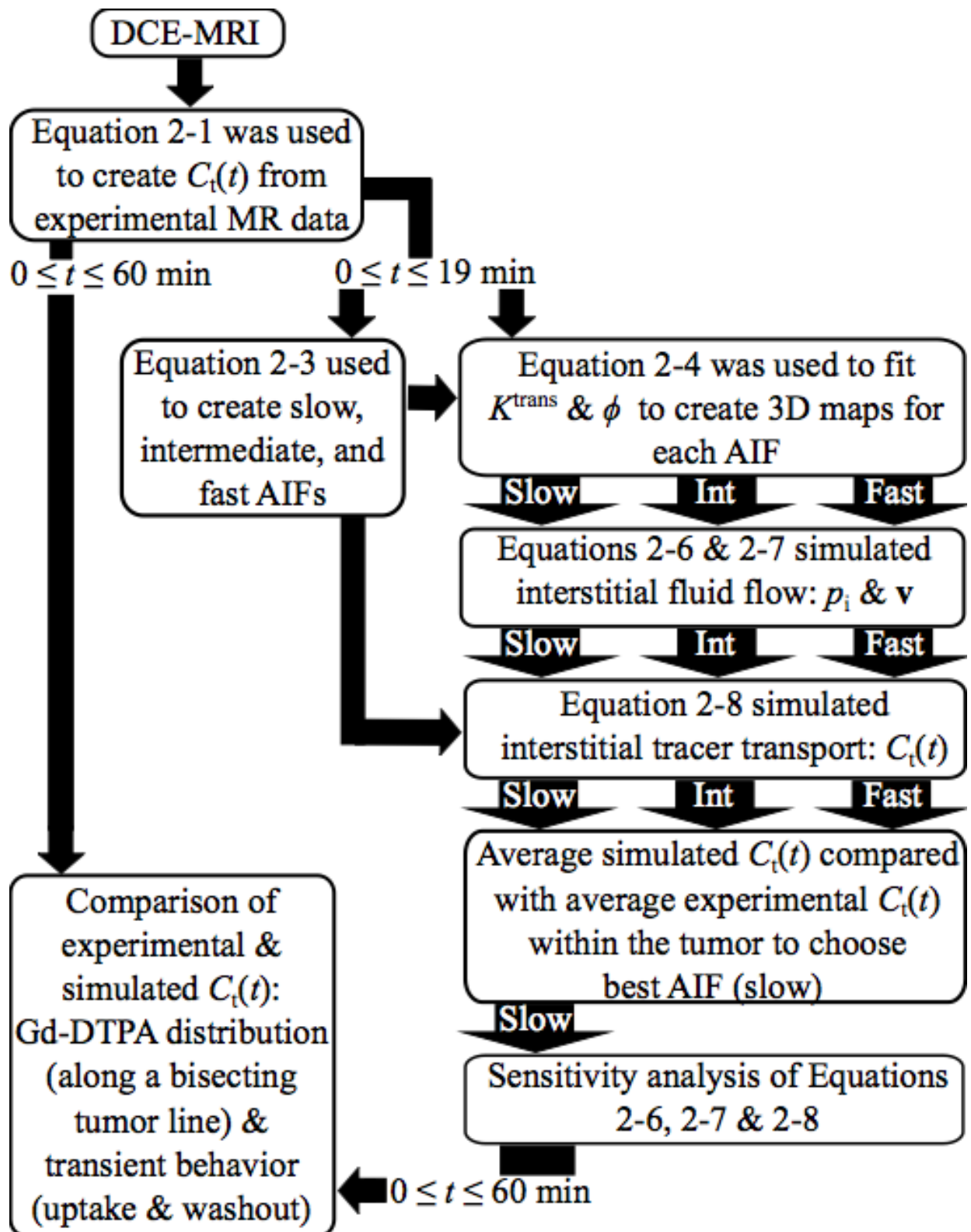


Figure 2-1. Block diagram of the mathematical methodology and experimental verification for the patient-specific tumor model.

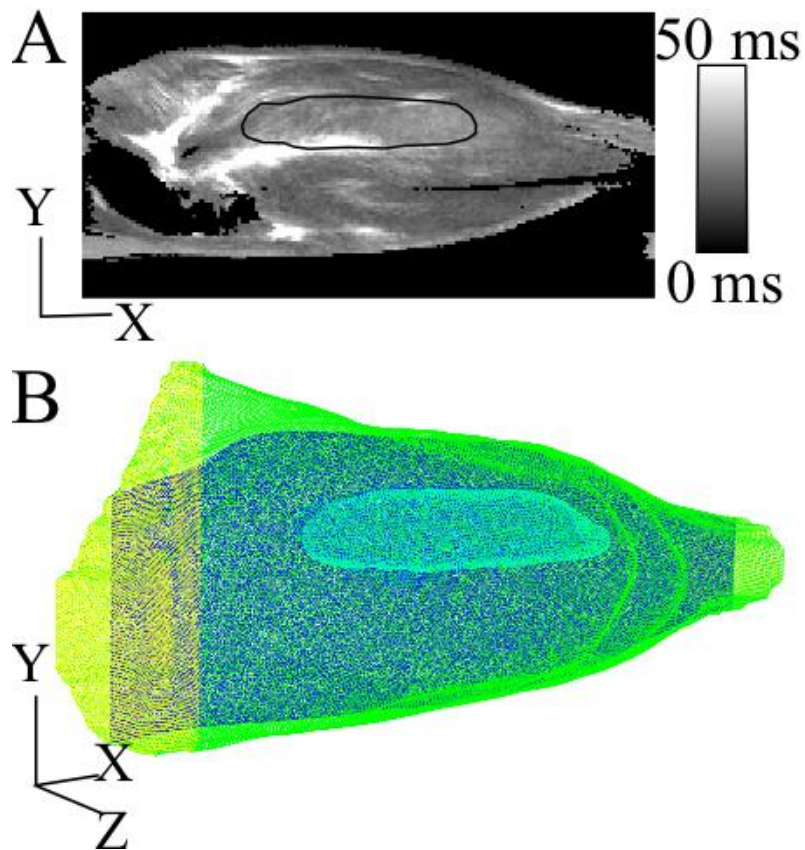


Figure 2-2. Geometric reconstruction of tumor and host tissue. Based on A) T_2 maps (slice 5, middle of tumor of MR data set). Segmented tumor boundary is outlined in black. B) CFD-compatible mesh of reconstructed hind limb that includes tumor (*light blue*), skin boundary (*green*), cut ends (*yellow*), and representation of slice 5 of the MR data (*dark blue*).

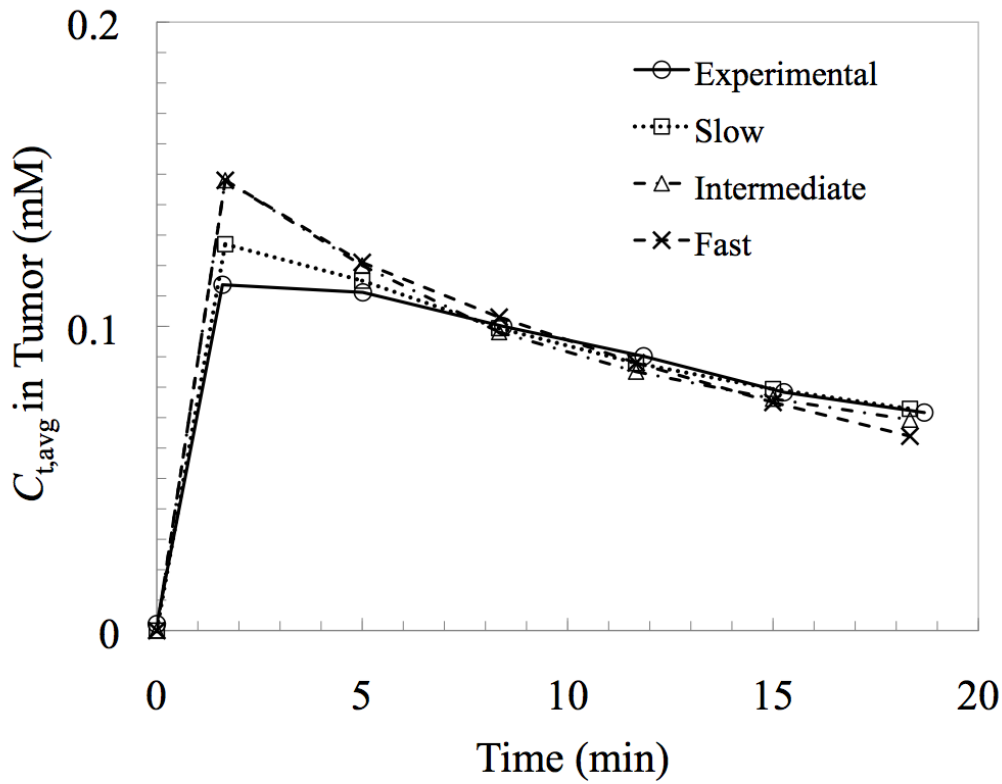


Figure 2-3. Uptake and washout of average Gd-DTPA concentration, $C_{t,avg}(t)$, in tumor tissue at seven time points for the first 19 min. Comparison between $C_{t,avg}(t)$ based on experimental (*uptake rate* = $0.071 \text{ mM min}^{-1}$; *monoexponential washout rate* = -0.029 min^{-1}) and simulations implementing slow ($0.076 \text{ mM min}^{-1}$; -0.034 min^{-1}), intermediate ($0.089 \text{ mM min}^{-1}$; -0.045 min^{-1}), and fast ($0.089 \text{ mM min}^{-1}$; -0.050 min^{-1}) AIFs.

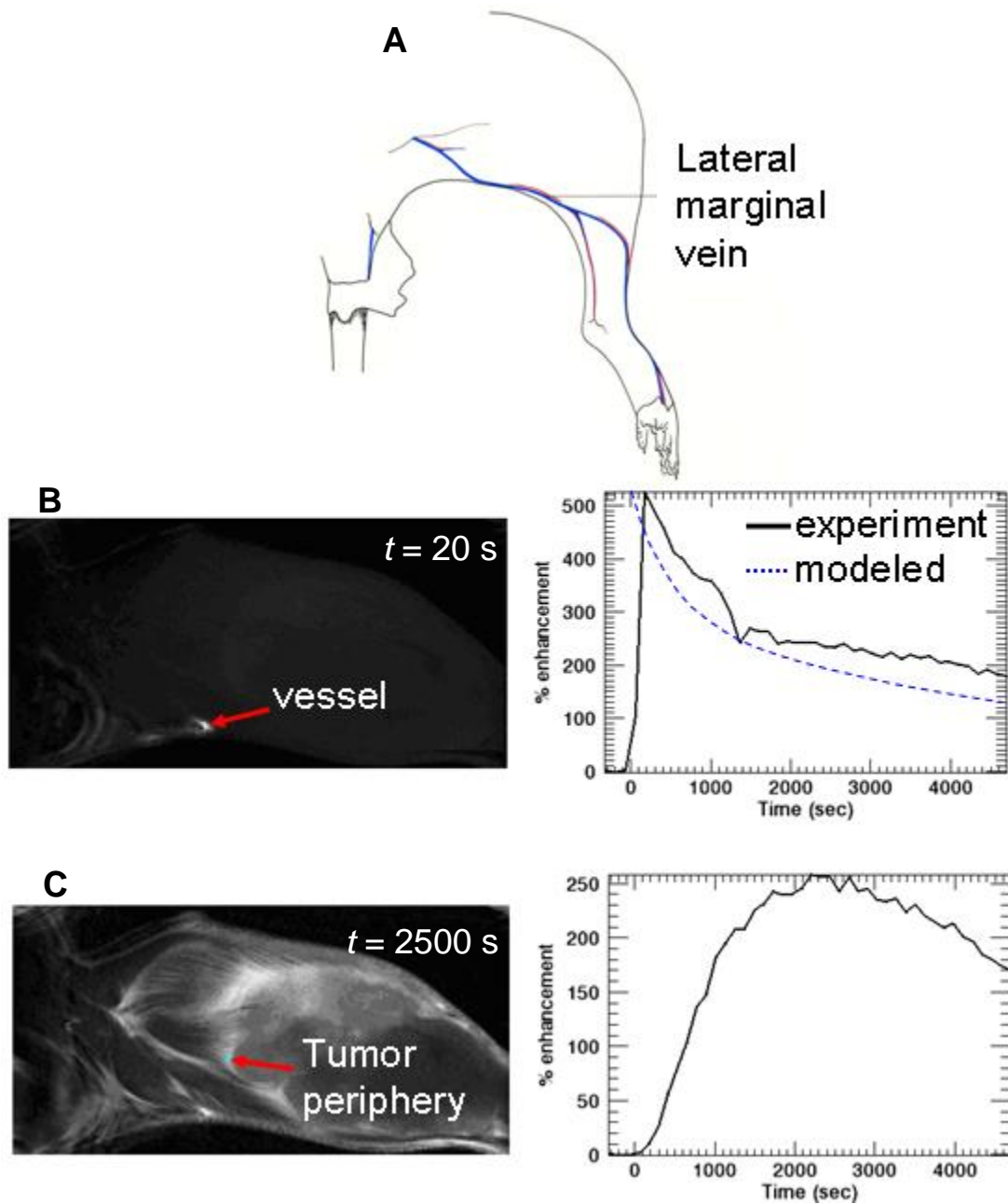


Figure 2-4. Signal enhancement in vessel and tumor periphery. A) Dorsal surface of right hind limb of mouse [*The Anatomy of the Laboratory Mouse*, Margaret J. Cook, <http://www.informatics.jax.org/cookbook/chapters/foreword.shtml>]. B) First post-scan of T_1 -weighted DCE-MR image and *experimental* signal enhancement in vessel region of interest (ROI) compared with the *modeled* slow AIF. C) Post-scan (2500 s) of T_1 -weighted DCE-MR image and corresponding signal enhancement in tumor periphery ROI.

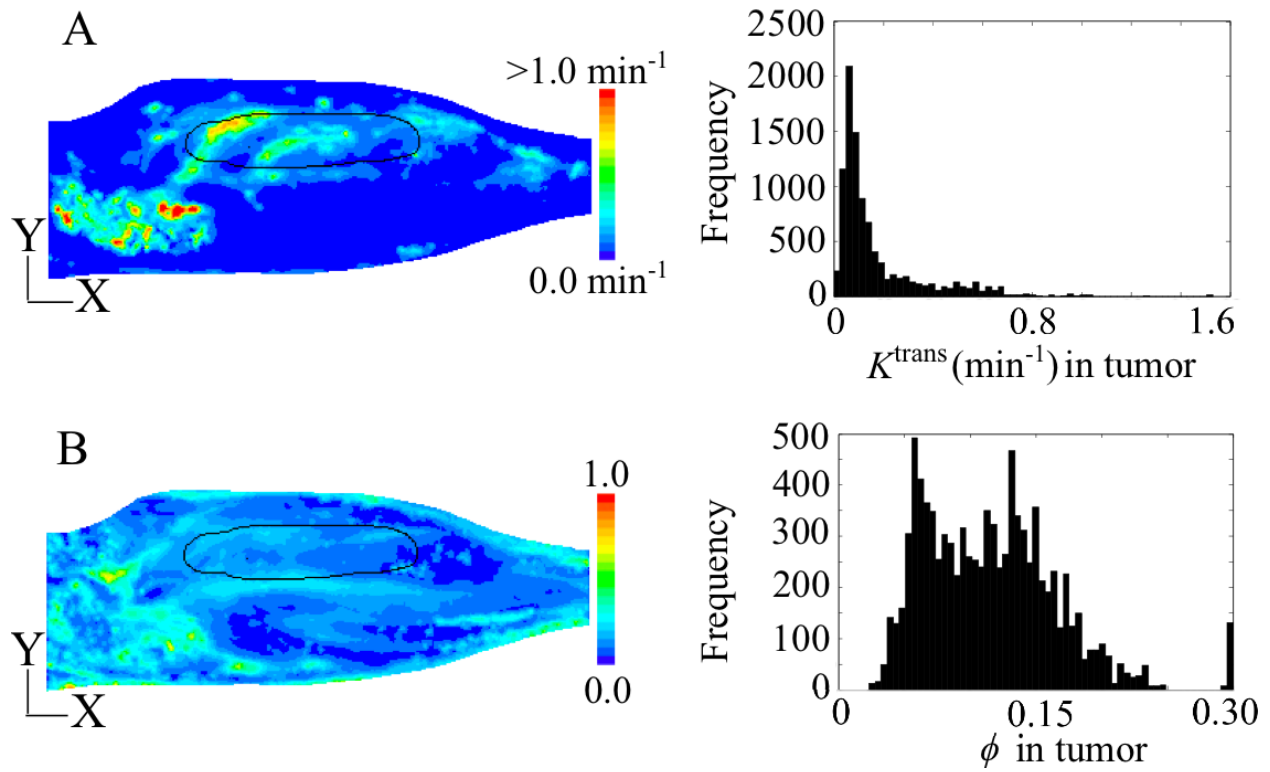


Figure 2-5. Maps from slice 5 of MR data set of A) K^{trans} and B) ϕ with histograms. Maps were implemented in the CFD-compatible mesh based on the slow AIF. Areas of greatest leakiness and porosity, respectively, are in red.

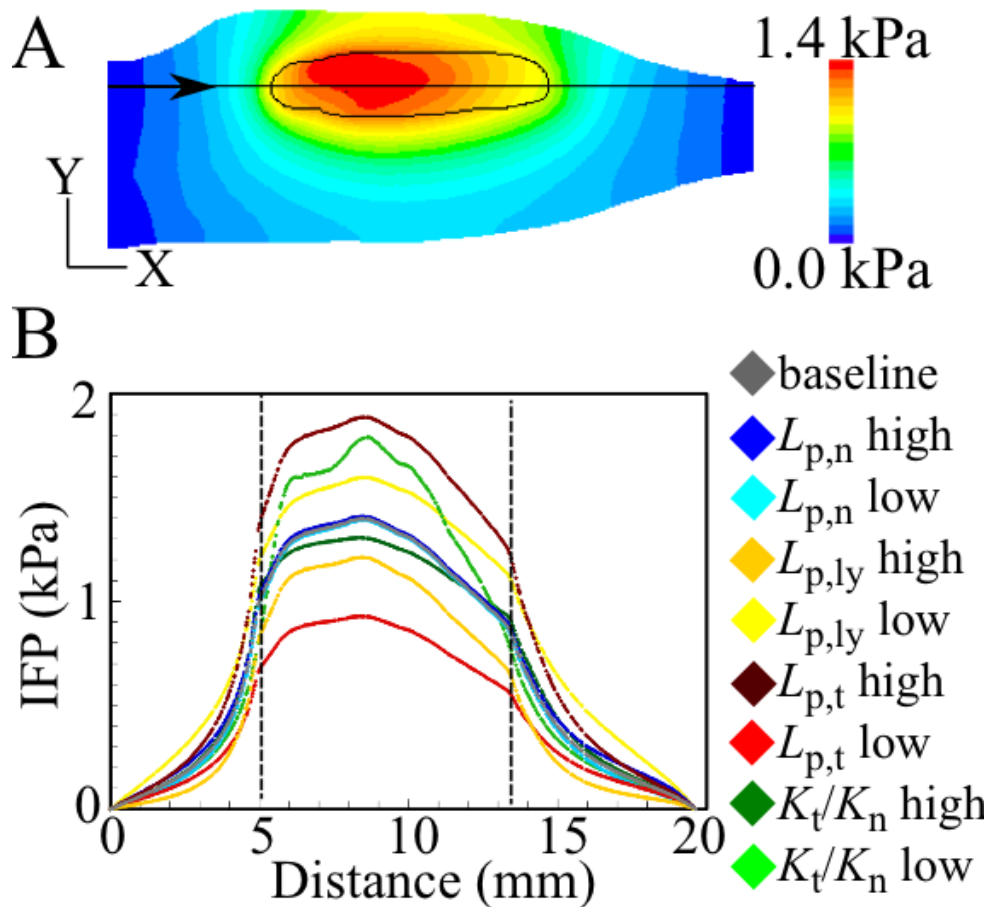


Figure 2-6. IFP sensitivity analysis for varying transport properties (Table 2-1B); A) IFP contours for the baseline case; B) IFP along the black line bisecting the tumor in the direction of the arrow in Figure 2-6A (dashed lines indicates tumor boundary).

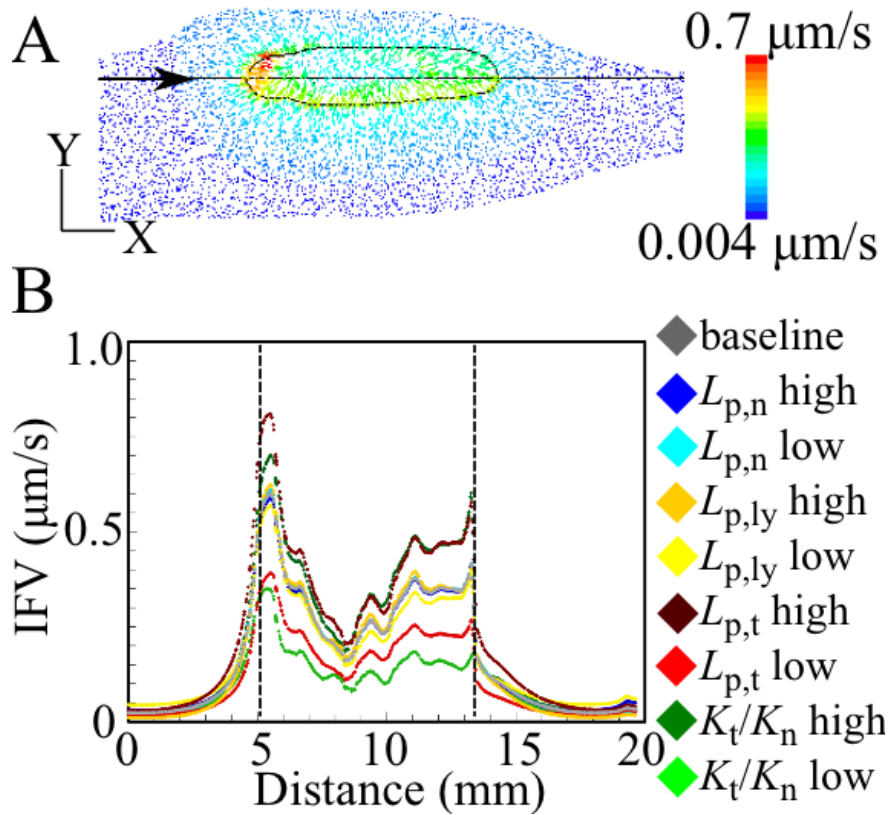


Figure 2-7. Tissue-averaged IFV sensitivity analysis for varying transport properties (Table 2-1B); A) Vector field for the baseline case; B) IFV along the black line bisecting the tumor in the direction of the arrow in Figure 2-7A. (dashed line indicates tumor boundary).

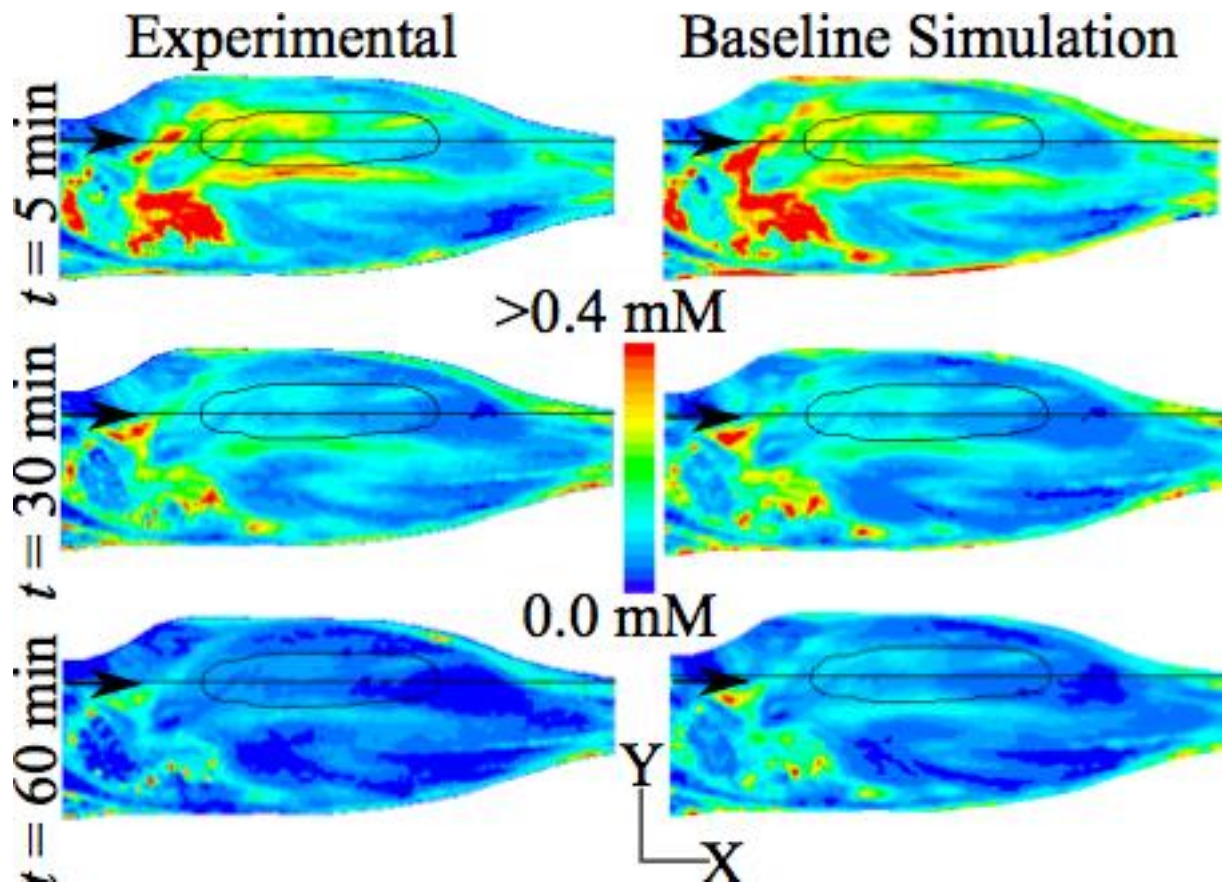


Figure 2-8. Comparison of experimental and simulated Gd-DTPA distribution patterns in slice 5 for $t = 5, 30,$ and 60 min for baseline transport values in Table 2-1B.

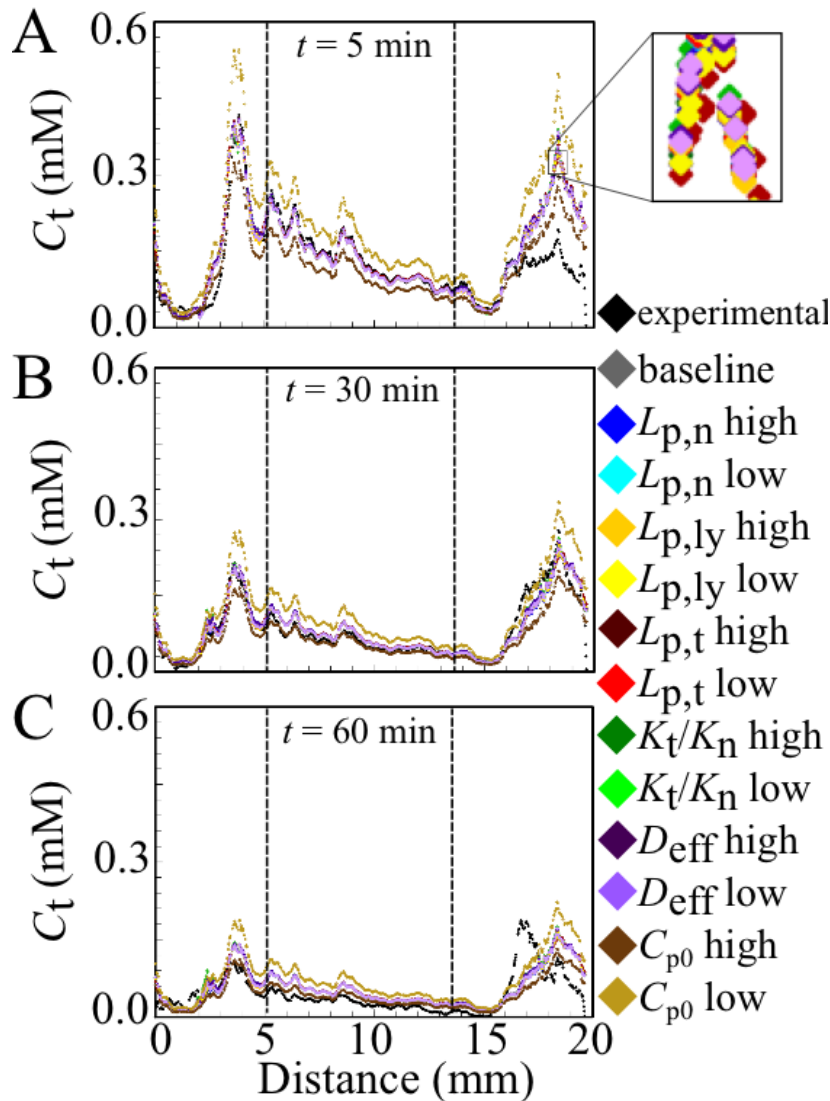


Figure 2-9. Gd-DTPA distribution along bisecting tumor line at early, intermediate, and late time points. The distribution is along the bisecting tumor line in the direction of the arrow as defined in Figure 2-8. Simulation from sensitivity analysis of parameters in Table 2-1B and C_{p0} as compared with experimental distribution for A) $t = 5$, B) $t = 30$, and C) $t = 60$ min. Simulated data shows considerable overlap except for simulations based on high and low C_{p0} .

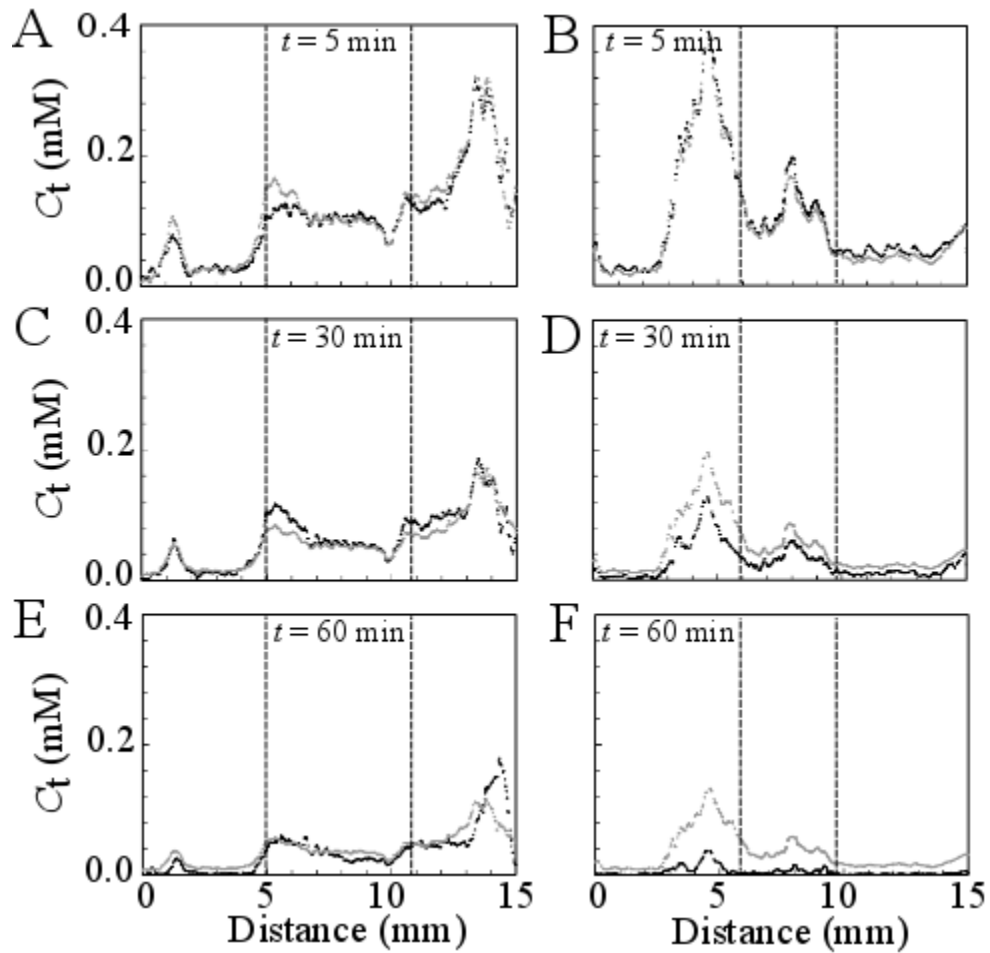


Figure 2-10. Gd-DTPA distribution along bisecting line through two additional KHT sarcomas. Simulated Gd-DTPA distribution (*grey*) compared with experimental distribution (*black*) for two tumors at A) and B) $t = 5$, C) and D) $t = 30$, and E) and F) $t = 60$ min, respectively. Dashed lines indicate tumor boundary.

CHAPTER 3 PATIENT-SPECIFIC COMPUTATIONAL MODELS OF SMALL SOLID TUMORS: A VALIDATION STUDY

3.1 Introduction

The previous chapter presented a patient-specific methodology for predicting interstitial fluid and tracer transport within a young, non-necrotic tumor. Transport was predicted using a porous media computational model and parameters that govern transport were investigated, via a sensitivity analysis, in order to document their effects on the transport solution. More specifically, tracer transport sensitivity analysis was conducted in the context of experimental data. The sensitivity analysis showed the dominance of transvascular exchange due to the high leakiness in the young tumors. The developed model was then applied to two additional young tumors in order to investigate the model's ability to predict tracer transport in other tumors. The main strength of the model is the ability to capture a distribution profile which compares well to the experimental profile—an advancement on our previously presented work [20]. This is largely a product of the porosity maps. A correlation was observed between predicted and experimental spatial deposition of Gd-DTPA within the tumor over the course of the experiment. Also, transient behavior of Gd-DTPA in the tumor showed good agreement between the simulation and experiment for two of the data sets. The degree of mismatches in late time point transient behavior, resulting in concentration magnitude differences, was likely proportional to errors in modeled and experimental AIF and interstitial flow.

The results and conclusions of the young, low interstitial fluid pressure (IFP) tumors with high leakiness presented in chapter 2 bolster those of low IFP tumors in the work of Hassid and cohorts (2006) [64]. Their study presented a simple two-

compartment model to estimate the transvascular exchange rate and porosity of low and high IFP tumors: MCF7 human breast and H460 lung cancer tumor, respectively, from magnetic resonance imaging (MRI) data. For lower IFP tumors (IFP ~ 1.9 kPa), they found that the simple two-compartment model described reasonable values of transvascular exchange and porosity, while less reasonable values were produced for higher IFP tumors (IFP ~ 3.7 kPa) suggesting the need to extend image-based physiologic models to include phenomena such as convection and diffusion for tumors with higher IFPs. Chapter 2 aimed to present an extension by testing such a model by investigating small tumors (IFP = 0.50–1.4 kPa) with high leakiness. Consequently, MRI-estimated transvascular exchange was the dominant term in the tracer spatial and transient behavior. While this term was dominant, there was a subtle difference in experimental and simulated clearance rate, which aside from mismatches in AIF could be caused by an underprediction of convection or lymphatic function causing an overprediction of Gd-DTPA in the tumor tissue. This chapter aims to further investigate and expand upon the image-based porous media tumor model by:

- Presenting a validation study of the model for young tumors by investigating an additional three tumors.
- Simplifying the computational approach by using a voxelized (Cartesian) mesh.
- Presenting histology that shows extent of tumor infiltration and vascularization to inform model assumptions (e.g., tumor size) and inputs (e.g., leakiness map trends, cellular density).

The results in Chapter 2 showed the importance of both K^{trans} and ϕ maps on the Gd-DTPA concentration distribution in time. The inclusion of both of these maps improved previously presented results [77]. Namely, better spatial and transient behavior of tracer concentration in tissue was observed. The addition of the K^{trans} and ϕ

maps corresponded to mathematical representations of the physiological environment in the patient-specific tumor model. The K^{trans} maps were important to provide the spatially varying leakiness due to non-uniformly distributed leaky vessels, which created non-uniformly, distributed interstitial fluid and tracer sources. The ϕ maps were important to provide non-uniformly distributed extracellular volume fraction due to varying cell density in *in vivo* tissue, which regulates the ability of interstitial fluid to dilute extravasated tracer in each voxel. With the incorporation of these maps, tracer concentration in tissue was found to be dominated by transvascular exchange for these particular small tumors ($< 37 \text{ mm}^3$) with high leakiness. With that said, there were two curious findings: 1) later time point comparisons of simulated and experimental data yielded slight inconsistencies of Gd-DTPA concentration in tissue and 2) the DCE-MRI method of determining porosity values may have underestimated the actual value of *in vivo* porosity. This suggested that physiological phenomena of the 3D porous media model were underestimated. Furthermore, physiological phenomena such as convection and diffusion can have effects on the perceived K^{trans} and ϕ values. The effects of reducing these values are likely to be exacerbated in maturing tumors where vessel remodeling can drastically reduce vessel leakiness. A validation study is the next step forward with the model and allows for these and other concepts to be investigated. For example, it allows the accuracy and consistency of model predictions to be tested against experimental data. In this chapter, that prediction is tracer distribution, magnitude, and transient behavior among a larger sample size. Additionally, this validation study not only allows for the examination of the utility of the 3D porous media model, but it also is a means of investigating a broader sample of tumor characteristics

(e.g., size and leakiness) that might affect the relative importance of terms in the tracer transport equation (i.e., convection, diffusion, and transvascular exchange). For example, the validation study can lend insight into a possible threshold tumor size, pressure, or leakiness, to name a few examples, at which diffusion and/or convection may play a more important role for the distribution of tracer over time. Conversely, tracer concentration in tumor tissue in tumor sizes under that threshold may be able to be approximated sufficiently using a two-compartment model accounting for transvascular exchange.

Tumor size and boundary can affect the estimated location of leakiness with respect to the tumor. This, in turn, can affect the perceived location of tracer or drug delivery in a porous media with a tumor-tissue interface. This study aims to discriminate tumor boundary based on MR measurements of the combination of leakiness pattern and T_2 values, or apparent diffusion coefficient (ADC) maps with a quantitative comparison with literature values of other studies.

MR imaging methods inherently store spatial data on a voxelwise basis. Because of this, MR image-based computational models lend themselves to a numerical solution that is computed using voxelized (Cartesian) meshes. This approach has been used to simulate infusion into the rat spinal cord [70] and rat brain [78]. For solid tumors, interstitial fluid and tracer transport simulations using an unstructured, like the one used in chapter 2, and voxelized mesh were shown to be comparable [79]. Additionally, tracer transport simulations based on chapter 2 data were shown to be consistent with the tracer measurements from the experimental data [80].

For the validation study in this chapter, heterogeneous tissue transport properties have been accounted for by incorporating vascular permeability and porosity maps for an additional three small KHT sarcomas. Permeability maps were created based on uptake of Gd-DTPA in tissue at early time points using dynamic contrast-enhanced magnetic resonance imaging (DCE-MRI). A fixed porosity ($\phi = 0.2$) was used and a K^{trans} scale factor (> 1) was optimized to account for possible reductions in their perceived values due to the interstitial flow. Also, a fixed porosity was used in this study to independently investigate the role of interstitial fluid flow on transient Gd-DTPA behavior in these tumors, so that spatial differences in behaviors would be due to interstitial flow and not porosity. Segmentation of tumor boundaries was conducted based on a combination of early DCE-MRI patterns and T_2 relaxation times ($n = 2$), and diffusion-weighted imaging (DWI) ($n = 1$). Assumptions made in the model about the tumor microenvironment were assessed via histology. Specifically, H&E and MECA 32 staining was used to examine the extent of tumor infiltration of the hind limb muscle, cell density, and extent of vascularization. A voxelized modeling approach was used to solve interstitial fluid and tracer transport for each of these specific tumors. As a part of the validation study, simulated tracer transport was compared to experimental tracer transport. Tracer transport was compared by quantifying peak tumor concentration, spatial distribution across tumor, and average uptake and washout behavior within the tumor. The porous media model was compared to the two-compartment model because the two-compartment model is the most widely used MR image-based model to obtain tracer concentration curves in tumor tissue space and time. Because each tumor has unique characteristics such as size and leakiness, the validation study also has the

potential to elucidate the role that such characteristics might have on the relative importance of convection, diffusion, and transvascular exchange within the tumor.

Garrett Astary (Department of Biomedical Engineering, UF) collected MR data. Jingya Zhang (Department of Biomedical Engineering, UF) sectioned tumors. Marda Jorgensen (MBI Cell & Tissue Analysis Core, UF) provided assistance with staining. Dr. Lori Rice and Sharon Lepler (Department of Radiation Oncology, UF) provided assistance and materials for tumor passage.

3.2 Materials and Methods

3.2.1 Animal Preparation

Three C3H/HeJ female mice (Jackson Laboratories, Bar Harbor, ME) were inoculated with between 1×10^5 to 2×10^5 murine KHT sarcoma cells in the gastrocnemius muscle. Murine KHT sarcoma cells were provided by Dr. Dietmar Siemann's laboratory (University of Florida, Gainesville, FL). The tumor was grown for 5 to 7 days. During animal preparation and imaging, the mouse was anesthetized using a gas mixture of 98% oxygen, 2% isoflurane. The lateral tail vein was catheterized using a Terumo SurFlo 24 Gauge $\times \frac{3}{4}$ " I.V. Catheter (Terumo Medical Corporation, Somerset, NJ) and given a 0.25 mmol/kg of body weight (bw) bolus tail vein injection of Gd-DTPA (Omniscan, GE Healthcare Inc., Princeton, NJ) CA at a constant rate (~ 0.4 ml/min, 0.23 ml). The animal experiment was governed by the principles of the Guide for the Care and Use of Laboratory Animals and approved by the University of Florida Institutional Animal Care and Use Committee (IACUC).

3.2.2 Magnetic Resonance Imaging (MRI)

The MRI experiment was performed using a Bruker Avance imaging console (Bruker NMR Instruments, Billerica, MA) connected to Magnex Scientific 11.1 T

horizontal bore magnet system (Varian, Inc., Magnex Scientific Products, Walnut Creek California). Tumor-bearing hind limbs of three mice were placed in a 1.5 cm inside diameter transmit and receive, volume coil. The animal body was oriented in the prone position with the leg secured to reduce motion. Figure 3-1 shows the approximate anatomical location of the tumors in the hind limb as well as the orientation of the MR slice geometry. Multiple T_2 -weighted spin echo (SE) scans (TR = 2000 ms, TE = 15, 30, 45, 60 and 75 ms; subjects 1 and 2: field of view (FOV) = 2 cm × 1 cm × 1 cm, 10 slices, matrix size = 192 × 96, 2 averages; subject 3: FOV = 2 cm × 1 cm × 1.2 cm, 12 slices, matrix size = 192 × 96, 1 average), were acquired for the calculation of T_2 values. A variable time for recovery (TR) SE sequence (TR = 5000, 2000, 1000, 500 and 250 ms, TE = 15 ms), was acquired for calculation of native tissue T_1 values used in CA concentration calculations. Serial DCE-MR images, consisting of T_1 -weighted SE sequence (subjects 1 and 2: TR/TE = 330 ms/9.4 ms, FOV = 2 cm × 1 cm × 1 cm, 10 slices, matrix size = 192 × 96, 2 averages, total acquisition time = 1 min 4 s; subject 3: TR/TE = 368 ms/9.4 ms, FOV = 2 cm × 1 cm × 1.2 cm, 12 slices, matrix size = 192 × 96, 2 averages, total acquisition time = 1 min 11 s) were collected before and after CA administration.

For DWI, a diffusion-weighted SE sequence was used with a total acquisition time = 33.8 min, FOV = 2.0 cm × 1.0 cm × 1.2 cm, TR = 1500 ms, TE = 21.5 ms, and one average. Low-diffusion-weighted data (70 s mm^{-2}) were acquired in 6 directions, defined by the tessellation of an icosahedron on a unit hemisphere, and high-diffusion-weighted data (520 s mm^{-2}) were acquired in 21 directions. MR data was obtained at the

Advanced Magnetic Resonance Imaging and Spectroscopy (AMRIS) facility in the McKnight Brain Institute (MBI) of the University of Florida.

3.2.3 Histology

After imaging sessions were completed, mice were euthanized and the tissue on the lateral side of the tibia and fibula was resected. This tissue primarily included tumor tissue as well as lateral gastrocnemius and soleus muscles. Tissue was fixed in 10% phosphate buffered formalin between 24 and 48 h, then moved into a histological cassette and placed in 70% ethanol before being embedded in paraffin wax. Tissue-embedded paraffin blocks were sectioned with a thickness of 5 μm using a microtome (HM 325, Microm, Germany). Four consecutive 5 μm sections were cut every 50 μm into the paraffin block. Two sections were hematoxylin and eosin (H&E) stained, processed with an automatic stainer (Leica Auto Stainer XL, Germany). The other two sections were stained with MECA-32 (BD Biosciences, Bedford, MA), a monoclonal antibody with high specificity for mouse endothelium.

A Leica microscope (DM 2500, Germany) was used to view slides and digital images were taken using a digital microscope camera (Optronics, Goleta, CA). Tumor area was estimated in the H&E-stained slides ($\times 1.25$ optical magnification). Vessel density was measured in peripheral and central regions of the tumor in the MECA-32-stained slides ($\times 20$ optical magnification).

Tumor infiltration of the hind limb muscle was investigated with the H&E stained sections by measuring tumor area. Tumor area was estimated using an in-house image analysis code (MATLAB v.7, Natick, MA) that counted tumor (purple) pixels from muscle and the background. Vessel density in the tumor was investigated with the MECA-32

stained sections. Vessel density was determined in the tumor rim and core by counting stained structures in up to 6 fields of 38 mm² at a magnification of ×20. The number of counted fields was limited by the size of the tumor.

3.2.4 Image Segmentation

Segmentation of tumor tissue for the computational model was manually conducted (MATLAB v.7, Natick, MA) based on the combination of contrast differences in T_2 maps from the variable TE SE sequence and peripheral enhancement in DCE-MRI ($n = 2$) or ADC maps ($n = 1$) from DWI. T_2 measurements were guided by that of normal hind limb mouse muscle (range = 18–22 ms) at 11.7 T [81] and with the assumption that T_2 values for tumor are typically higher than normal muscle due to the increased mobility of extracellular water that occurs from apoptosis [82]. Tumor boundary was demarcated in ADC maps based on the observed ADC differences between tumor and muscle [67]. All of the tissue regions outside of the tumor were designated as host muscle in the model.

3.2.5 Arterial Input Function, Vascular Permeability Maps, and Porosity Maps

Chapter 2.2.3 showed the link between vascular leakiness (K^{trans}) maps, porosity (ϕ) maps, and arterial input function (AIF). The shape (rate of clearance) of the biexponential AIF impacted the outcome of the K^{trans} and ϕ maps. The impact of these maps on tracer uptake and wash out was borne out in Figure 2-3. The slow AIF produced the best fit for average concentration within the tumor volume and also showed a similar trend to the measured biexponential in a vessel using DCE-MRI (Figure 2-4B). An imaging protocol was established to obtain the enhancement patterns in a major vessel of the hind limb by setting up the imaging geometry such that a vessel

was contained in a single voxel. The advantage of this was to gain information on the AIF behavior during the same DCE-MR imaging session as the one used to create permeability maps. Post-imaging analysis revealed that no major vessels were captured in imaging sessions. While a signal enhancement curve like that of Figure 2-4B could not be established for individual data sets in this study, it does indicate the likely nature of the AIF for this experimental setup. Additionally, the results of using the slow AIF established similar uptake and washout over the early time points of average Gd-DTPA concentration in tumor (Figure 2-3). For these reasons, a slow AIF [26, 32] was used where $a_1 = 4.0 \text{ kg bw L}^{-1}$, $a_2 = 4.8 \text{ kg bw L}^{-1}$, $m_1 = 0.002 \text{ s}^{-1}$, and $m_2 = 0.0002 \text{ s}^{-1}$ in Equation 2-3; a_1 and m_1 represent the amplitude and rate constant, respectively, of the fast equilibrium between plasma and extracellular space; a_2 and m_2 represent the amplitude and rate constant of the slow component of the clearance.

DCE-MRI data was converted into concentration measurements based on Equation 2-1. K^{trans} maps were created based on early time points (first 15 min) of concentration data using the same two-compartment analysis as described in Equations 2-2 through 2-4 with a fixed porosity of 0.2. Values of K^{trans} were set to zero in voxels where the fit was poor ($R^2 \leq 0.5$). K^{trans} values in pixels that showed no Gd-DTPA uptake ($< 0.005 \text{ mM}$) during the first two post scans were filtered out as well.

3.2.6 3D Porous Media Mathematical and Computational Model

The 3D porous media mathematical model presented in chapter 2.2.4 was used to predict the steady-state interstitial fluid flow and transient Gd-DTPA distribution assuming the tissue as porous media.

The computational modeling times were reduced by using a voxelized (Cartesian) mesh to store the spatially discretized porous media transport solutions instead of an

unstructured mesh (Figure 3-2). Rectangular volumes were created (Gambit, Fluent, Lebanon, NH) that corresponded to the exact dimensions of DCE-MRI data (field of view = $2 \times 1 \times 1 \text{ cm}^3$ for KHT-1 & KHT-2; field of view = $2 \times 1 \times 1.2 \text{ cm}^3$ for KHT-3). Eight-node brick elements were used to create meshes consisting of 205,931 nodal points (KHT-1 & KHT-2) and 243,373 nodal points (KHT-3). The CFD software package (FLUENT 6.3, Fluent, Lebanon, NH) was used to solve porous media transport.

Tissue and transport properties in tumor and host muscle were assigned according to baseline values (Table 2-1) in FLUENT. Prediction of tumor tracer distribution was a two-step process. First, steady-state interstitial plasma fluid flow was solved (Equation 2-6). Then, tracer transport (Equation 2-8) was solved at later time points. The only difference between boundary conditions of unstructured mesh (chapter 2) and the Cartesian mesh was at the skin boundary. In order to maintain a no flux condition for interstitial fluid at the skin, brick elements outside of the muscle regions (exterior cells, Figure 3-2C) were assigned hydraulic conductivity values two orders of magnitude lower than muscle. This low hydraulic conductivity value was assigned in the exterior cells to effectively reduce the interstitial flow in this region to zero. There should be no interstitial flow here because there is no tissue in this region. The convergence problem associated with the porous media solver in FLUENT for low hydraulic conductivity materials was avoided by reducing the under-relaxation factor and step-wise reductions of hydraulic conductivity to reach the final baseline value. Effective diffusion was set to zero in the exterior cells so that tracer flux was zero at the skin boundary.

3.3 Results

3.3.1 Segmentation, Leakiness, and Histology

Segmentation of tumor tissue resulted in increased (13–33%) T_2 values (KHT-1 & KHT-2) and decreased (-44%) ADC value (KHT-3) in tumor regions of interest (ROIs) when compared with normal muscle ROIs (Figure 3-4). Contrast between assumed tumor and muscle was greater in ADC maps than T_2 maps. KHT-3 was found to be the largest (most mature tumor) of the three based on total segmented volume (120 mm³) and most tumor infiltration observed in the H&E stained tumor cross section (area = 4.4 ± 0.9 mm²; Figure 3-5E). KHT-1 and KHT-2 showed less tumor infiltration in both the total segmented tumor volume (KHT-1: 43 mm³; KHT-2: 63 mm³) and area of tumor in the H&E stained-sections (KHT-1: 1.8 ± 0.3 mm²; KHT-2: 1.5 ± 0.7 mm²).

K^{trans} maps showed leakiness heterogeneity in the tumor and surrounding tissue (Figure 3-6). Increased leakiness was observed around the perimeters for all tumors when compared to the tumor mass (> 100%). Average K^{trans} value within the tumor decreased with tumor size. Within the tumor, leakiness variations were not as pronounced, which was corroborated by MECA-32 staining for endothelial cells. For the largest of the three tumors (KHT-3), MECA-32 staining showed the tumor to be well-vascularized at both the rim and center (Figure 3-7) based on the mean number of vessels per mm² at the tumor rim (147 ± 100) and tumor center (158 ± 49). Histological sections of the two smaller tumors were not large enough to distinguish a tumor rim and center.

3.3.2 Interstitial Fluid Transport

Interstitial plasma fluid pressure was predicted to be higher within the tumor than in normal tissue for all three subjects (Figure 3-8). Intratumoral pressures increased with tumor size: KHT-1 (0.62 kPa; Figure 3-8A), KHT-2 (0.85 kPa; Figure 3-8B), and KHT-3 (1.79 kPa; Figure 3-8C). These peak pressures within the tumor fell slightly towards the tumor boundary with the pressure gradient greater than 0.38 kPa mm^{-1} . Subsequently, the largest boundary pressure gradient was observed in KHT-3.

The increased pressure resulted in flow of interstitial fluid directed outward from the tumor boundary. Interstitial velocity of plasma fluid was predicted to be highest at or near the boundary of the tumor (Figure 3-9). Average fluid velocity at the tumor boundary increased with tumor size: KHT-1 ($0.10 \text{ } \mu\text{m s}^{-1}$; Figure 3-9A), KHT-2 ($0.13 \text{ } \mu\text{m s}^{-1}$; Figure 3-9B), and KHT-3 ($0.40 \text{ } \mu\text{m s}^{-1}$; Figure 3-9C). These areas of high velocity correspond to the larger pressure gradients.

3.3.3 Tracer Transport

Experimental Gd-DTPA spatial and transient concentration behavior exemplified the non-uniformity of tracer delivery. Furthermore, differences in behavior between tumors highlighted the patient-specific nature of systemic delivery. Spatially, all three subjects showed increased uptake ($> 80\%$ at peak concentration) at the tumor periphery when compared with the central tumor region. Temporally, uptake within and around tumor tissue was slow. At $t = 8 \text{ min}$, the average concentration of Gd-DTPA in the central tumor region was minimal ($0.02\text{--}0.05 \text{ mM}$), but slowly increased ($> 90\%$) over the next 15 min in this region. Peak concentration was reached at $t \geq 30 \text{ min}$. Peak and washout characteristics varied between tumors, with slower washout corresponding to

increased tumor size. KHT-1 and KHT-2 showed signs of washout at 30 min and 65 min, respectively. The washout rate in the tumor was quicker for KHT-1 (0.11 mM hr^{-1}) than KHT-2 (0.08 mM hr^{-1}). The tumor of KHT-3 did not show Gd-DTPA washout over the imaging time course ($t \leq 1.7 \text{ hr}$).

Peak Gd-DTPA concentration occurred at $t \geq 30 \text{ min}$ for all porous media simulations, with the average peak occurring later in time with increased tumor size. Also, washout rates decreased with increasing tumor size. While transient behavior of the experimental data was similar to the baseline porous media simulations, the magnitude of the concentration within the tissue was underpredicted (Figure 3-10). At peak Gd-DTPA concentration, baseline simulations were underpredicted by less than 35%.

Tracer transport simulations were optimized to provide optimal concentration magnitudes and transient behavior in the tumor with the assumption of constant porosity ($\phi = 0.2$). K^{trans} values were scaled by a constant to account for the perceived reduction in permeability in the case of low transvascular exchange. The transient concentration behavior in the tumor using the porous media model compared better than the two-compartment model over the course of the simulation based on the Pearson product-moment correlation coefficient (PMCC), r , where $r > 0.9$ for the porous media model (Figure 3-10). The two-compartment model performed better as washout was less significant in the tumor. PMCC was lowest for KHT-1 (most washout) with $r = 0.53$ and highest for KHT-3 $r = 0.98$ (least washout). Increasing the K^{trans} scale factor did not change the overall shape of the concentration curves; hence it did not appreciably

change PMCC (< 1%). However, peak Gd-DTPA concentration values increased from the baseline peak value in response to an increase in the K^{trans} scale factor.

By comparing the results of the simulations and experiment through quantifying error versus time, revealed that scaling K^{trans} by a value greater than one resulted in reduced error over the time of the simulation compared with the baseline (Figure 3-11). Root mean squared (RMS) errors, ϵ , of the data in Figure 3-11 shows a decreasing trend of error with increasing K^{trans} scale factor. At early time points (first three), the two compartment model resulted in lower absolute error than the porous media model, but the error increased with time. This was most evident in KHT-1 (Figure 3-10A) and KHT-2 (Figure 3-10B); at the final time points, the two-compartment model resulted in absolute error > 0.05 mM, which was > 100% of the average concentration in the tumor. The porous media model predictions resulted in smaller absolute error (< 0.02 mM) than the two compartment model at the final time point.

Optimized porous media simulations showed similar spatial trends to the experimental data (Figure 3-12 and 3-13). Both simulated and experimental Gd-DTPA concentration profiles depicted the trend of reduced uptake within the center of tumor; the concentration of Gd-DTPA increased at the boundaries. For the tumor with the highest washout rate (KHT-1), concentration simulations showed reduced uptake (50% less) within the tumor at early time points when compared with periphery (Figure 3-12A). The higher washout rate lead to the largest decrease (50 %) in Gd-DTPA concentration in tumor over the experimental and simulated time courses when compared with the other tumors. At later time points (Figure 3-12B), the concentration difference across the tumor boundary was less pronounced (42% less). All of the tumor

simulations resulted in more flattening of the concentration curve within the tumor over time than the experimental data. The greatest flattening of the concentration curve within the tumor occurred in KHT-3 (Figure 3-13) where the relative difference in peak and base concentration in the tumor was < 10% for the simulation and 85% for the experiment.

3.4 Discussion and Conclusions

This chapter presents the application of the image-based model to multiple small non-necrotic tumors ($\leq 120 \text{ mm}^3$) for the prediction of interstitial fluid and solute transport with heterogeneous leakiness. These models predict interstitial hypertension and increased velocities at the host tissue-tumor interface like the model presented in chapter 2. While chapter 2 showed the importance of porosity upon the distribution of Gd-DTPA concentration in tissue over time, this chapter presented models using a fixed porosity. A fixed porosity was necessary for two reasons. Most importantly, the uptake rate within tumor tissue was too slow to obtain a physiologically relevant value by using the two-compartment model to fit early time points of concentration data. Secondly, porosity values obtained in chapter 2 ranged (0.05–0.15) lower than values measured by DCE-MRI-independent methods (0.2). Fixing the porosity also allowed Gd-DTPA clearance in the tumor due to interstitial fluid motion and not a low extracellular volume fraction. The simulations with fixed porosity showed the ability of interstitial fluid to transport extravasated solute out of the tumor. Transient behavior of average Gd-DTPA in the tumor showed agreement between the simulation and experiment. The establishment of a model that accounts for convection, diffusion, and transvascular

exchange underscores these phenomena role in solute transient behavior and distribution in tissue.

The importance of the porous media model for small molecular weight solutes as well as the potential effects of interstitial fluid flow on perceived MRI-measured values of K^{trans} and ϕ was demonstrated in this chapter. This is best illustrated by assuming pure transvascular exchange over the entire course of the experiment to obtain these parameters, which is often assumed in literature [30, 31, 83]. In this limited case, results of the model lead to K^{trans} (inflow of tracer from the blood into the interstitial space) that are much smaller than outflow (tracer entering back into blood pool from the interstitial space). A common consequence is small, non-physiologically relevant ϕ values (< 5%) within the tumor. Similar average values for ϕ have been reported before for this experimental tumor type (KHT sarcoma) using the standard kinetic model [83]. While the H&E stains of the KHT sarcoma in the work of Nielsen et al. qualitatively revealed densely packed cells throughout most of the tumors, 5% is on the extreme low end of previously measured cell densities in grafted tumors [84]. A porosity of 5% was measured in specific locations within the tumor and did not represent the average porosity of the whole tumor in the work of Jakobsen et al. The H&E staining of the KHT sarcomas presented in this chapter showed cell packing similar to that of Nielsen et al; hence it was reasonable to use a porosity of 0.2 which represented the low end of average porosity in tumors [85]. The large difference in inflow and outflow, which can result in unrealistic ϕ implies other physiological phenomena aid clearance of Gd-DTPA in tumors. This observation has been made in the DCE-MRI pressure measurement work of Y. Hassid et al. (2006 and 2008). Hassid and cohorts suggested that the

apparently low ϕ values were not physiologically representative of the extracellular volume fraction itself, but that interstitial fluid flow is likely responsible for the clearance behavior within the tumor.

The application of the porous media model to determine average Gd-DTPA concentration in the tumor reduced the absolute error when compared with the two-compartment model using a fixed porosity. This concept was apparent in both Figure 3-10 and Figure 3-11. Furthermore, the importance of interstitial fluid flow on the overall transient behavior in the tumor can be illustrated by using the two-compartment model to simultaneously fit K^{trans} and ϕ over the course of the simulations presented in this chapter. Even though the porosity was fixed at 0.20, KHT-1 and KHT-2 resulted in porosity values less than 0.06 while KHT-3 resulted in average porosity values less than 0.10 in the optimized, scaled K^{trans} cases. These low values misrepresent the extracellular volume fraction used in the simulations and underscore the importance of the porous media model's ability to account for the effects of interstitial fluid on tracer clearance in tumor. Models with low leakiness (K^{trans}) could benefit from DCE-MRI independent imaging methods of obtaining porosity. Current imaging methods do not allow for the porosity measurements, but T_1 - or T_2 - weighted images may be a way to approximate porosity pattern.

The interstitial fluid flow pattern resulted in an average Peclet number of approximately 2–5 revealing that Gd-DTPA transport is slightly more convective than diffusive. This range of Peclet numbers has been presented in previous tumor models [20]. Peclet number was defined by, $Pe = vL/D_{\text{eff}}$ where v is the velocity magnitude and L is characteristic length of 1 mm. The outward direction of the convective transport

aided in movement of extravasated solute to the boundaries of the tumor of the entire time course of the simulation and experiment. Not only does this phenomenon contribute to a reduced apparent porosity as described earlier, but also a reduced K^{trans} . The measured K^{trans} value in a given voxel could be lower than the actual K^{trans} value because of extravasated solute transported out of the voxel due to convective interstitial flow. The convective transport in the tumor may be responsible for the slower uptake seen in the experimental tumors in this study. This was the motivation for scaling K^{trans} values within the tumor to determine optimal transient behavior. MECA-32 staining confirmed prevalence of vessels throughout the tumor, but these vessels could have reduced leakiness due to vessel remodeling and thickening of vessel walls that can occur in maturing tumors [86]. This remodeling may have also contributed to differences in early uptake rates seen in the tumor in chapter 2 and those in this chapter.

This study showed that there is not a particular set of parameters that can be applied to all tumors. In other words, there is no one-size-fits-all approach to modeling interstitial and solute transport in the presented KHT sarcomas. In the case of vessels with low leakiness, the porous media model can be used to account for the interstitial fluid flow and the potential misrepresentation of K^{trans} and ϕ that are important physiological inputs into the model. Fitting K^{trans} values with a fixed, reasonable ϕ at early time points, then using those values to predict concentration in tumor at later time points using a two-compartment model grossly overestimates concentration. The use of a baseline porous media model to make that same prediction underestimates the concentration of solute in tumor at later time points, but allows for more accurate transient behavior than the two-compartment model because it accounts for the effects

of the interstitial fluid flow. Scaling K^{trans} values to account for reduction in measured leakiness due to convection does provide a path to more accurate predictions of concentration in tumor with low leakiness.

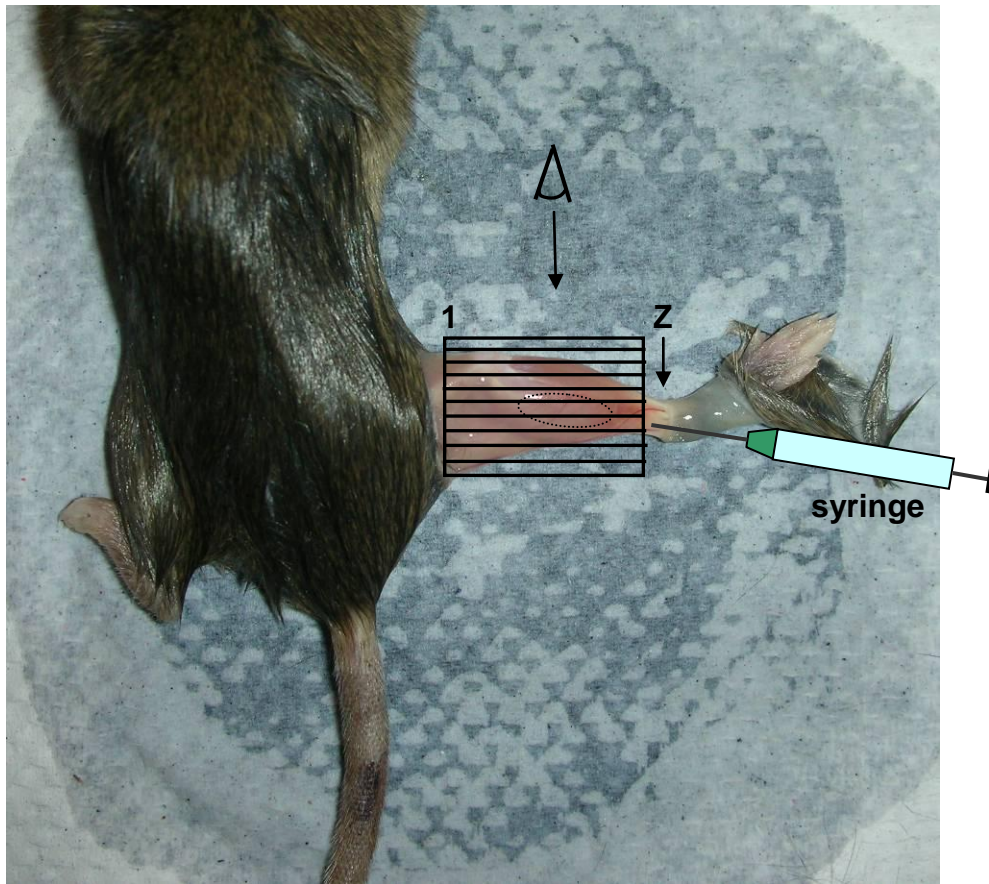


Figure 3-1. Orientation of MR slices with respect to the mouse anatomy (top view). The first slice of MR data is labeled 1. Point of view of the MR slices is shown. Syringe shows the location of the inoculation. The dotted line shows the approximate location of the grafted tumors.

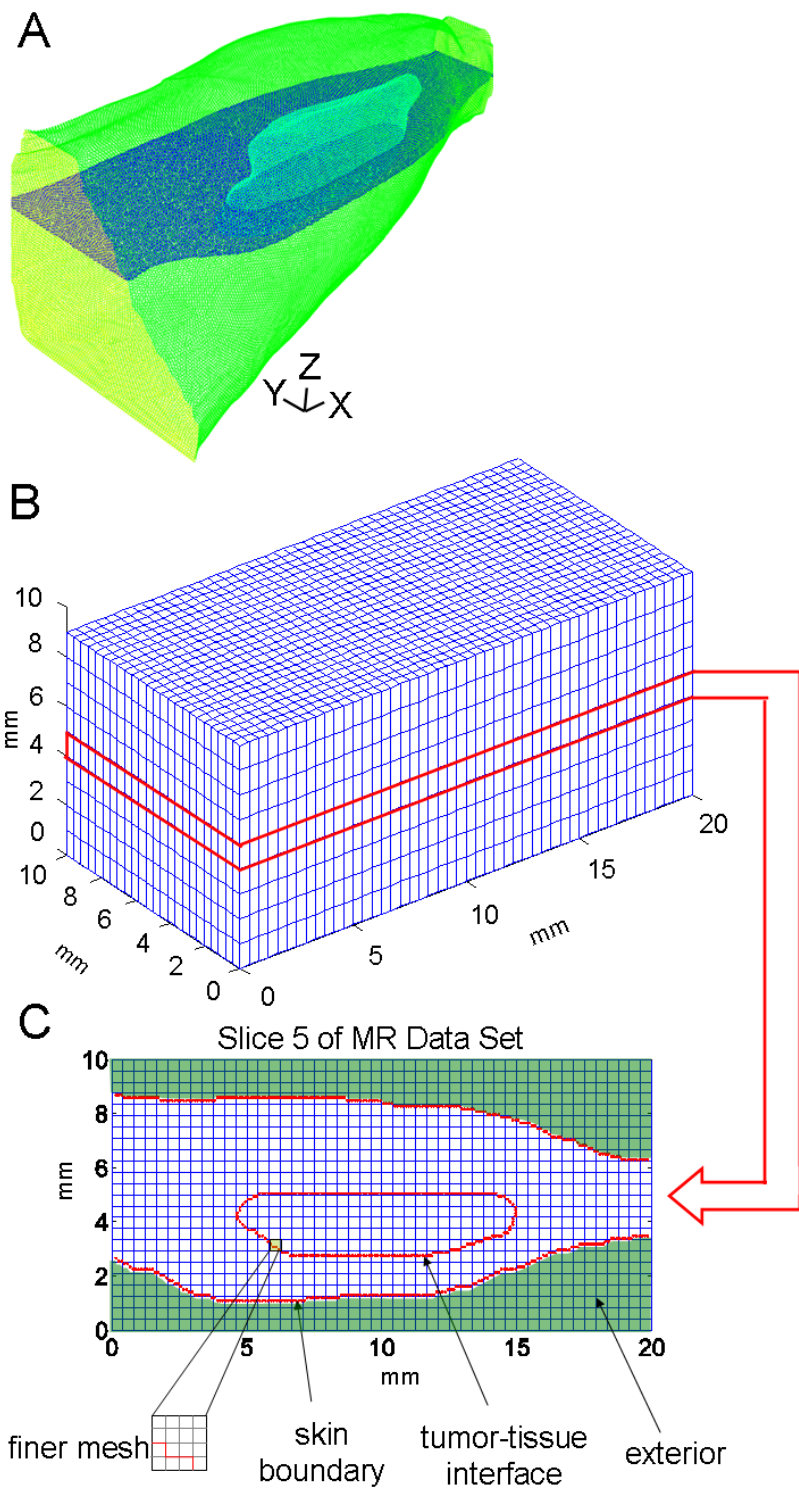


Figure 3-2. CFD compatible meshes. A) Unstructured mesh of reconstructed hind limb from Figure 2-2B simplified to B) a voxelized (Cartesian) mesh and C) detailed view of a segmented slice.

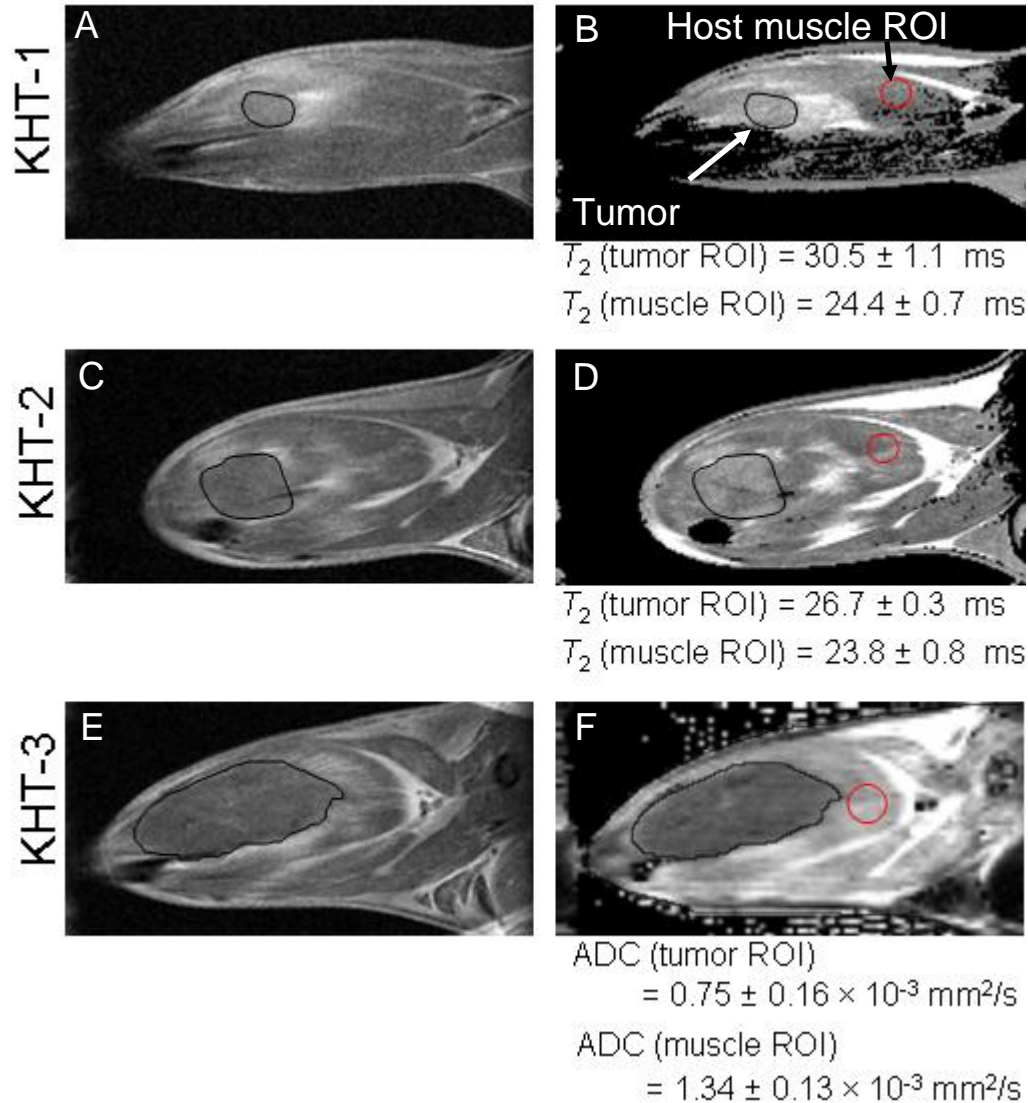


Figure 3-4. Tumor segmentation of MRI data for small KHT sarcomas. Segmentation for KHT-1 based on A) early DCE-MRI enhancement and B) T_2 values. Segmented tumor boundary (*black*) and host muscle region of interest (*red*) shown with corresponding T_2 values for these regions. Segmentation for KHT-2 based on C) early DCE-MRI enhancement and D) T_2 values with measured values for tumor and host muscle ROI. Segmentation for KHT-3 based on E) early DCE-MRI enhancement and F) ADC values. ADC values for tumor (*black*) and normal host muscle ROI (*red*) are shown.

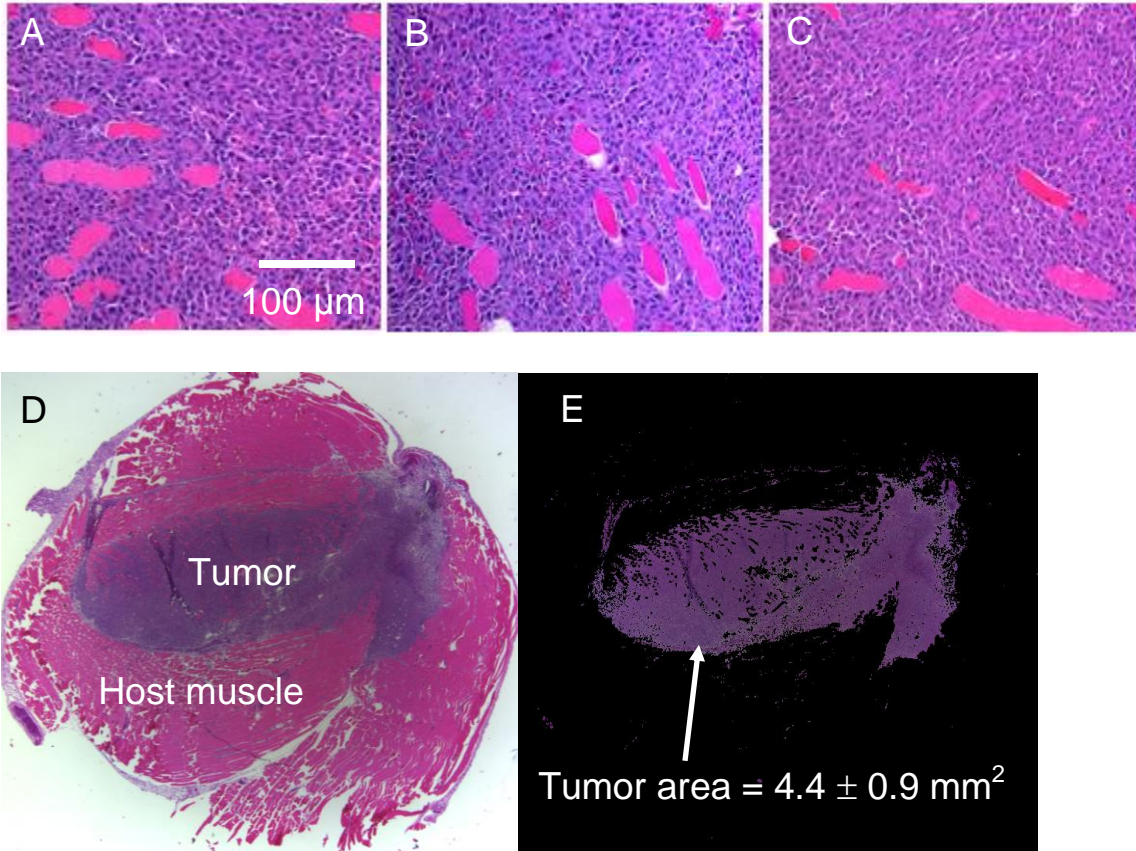


Figure 3-5. H&E staining and example of estimating tumor area. Dense cellular regions in the tumor of A) KHT-1, B) KHT-2, and C) KHT-3. D) KHT-3 H&E-stained with corresponding E) segmented H&E stain.

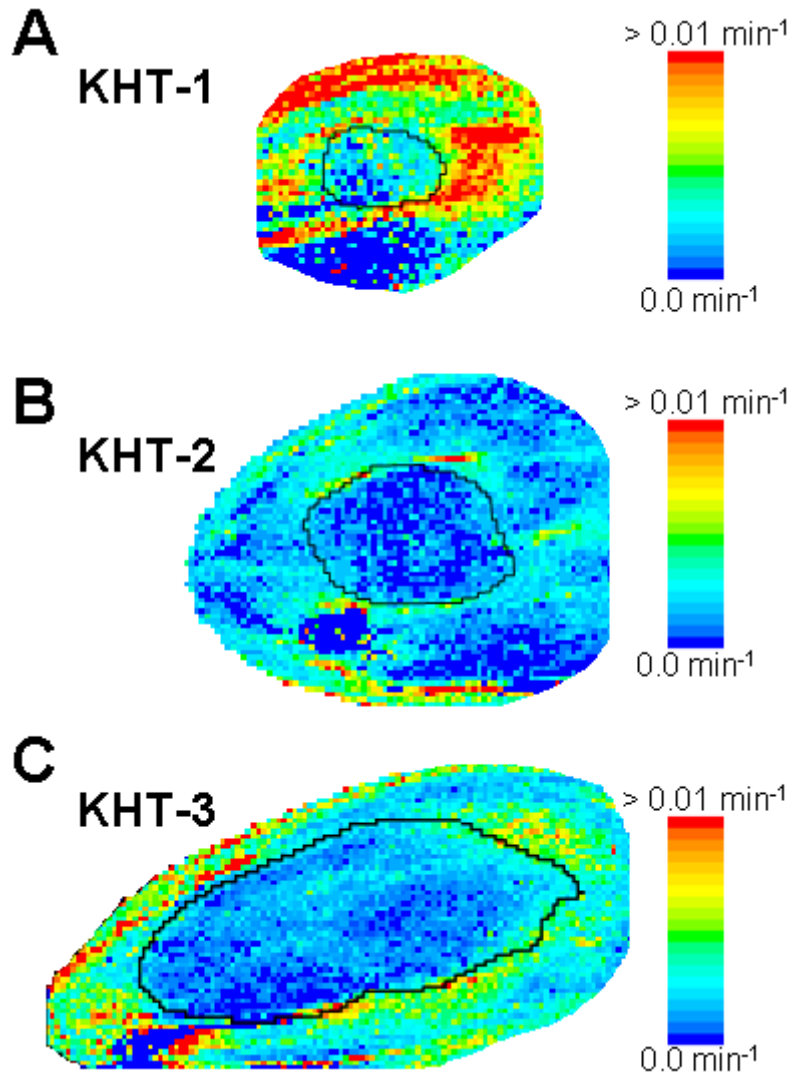


Figure 3-6. Leakiness (K^{trans}) maps of small KHT sarcomas. Maps for A) KHT-1, B) KHT-2, and C) KHT-3. Leakiness outside the tumor boundary (*black line*) is higher than inside the tumor boundary.

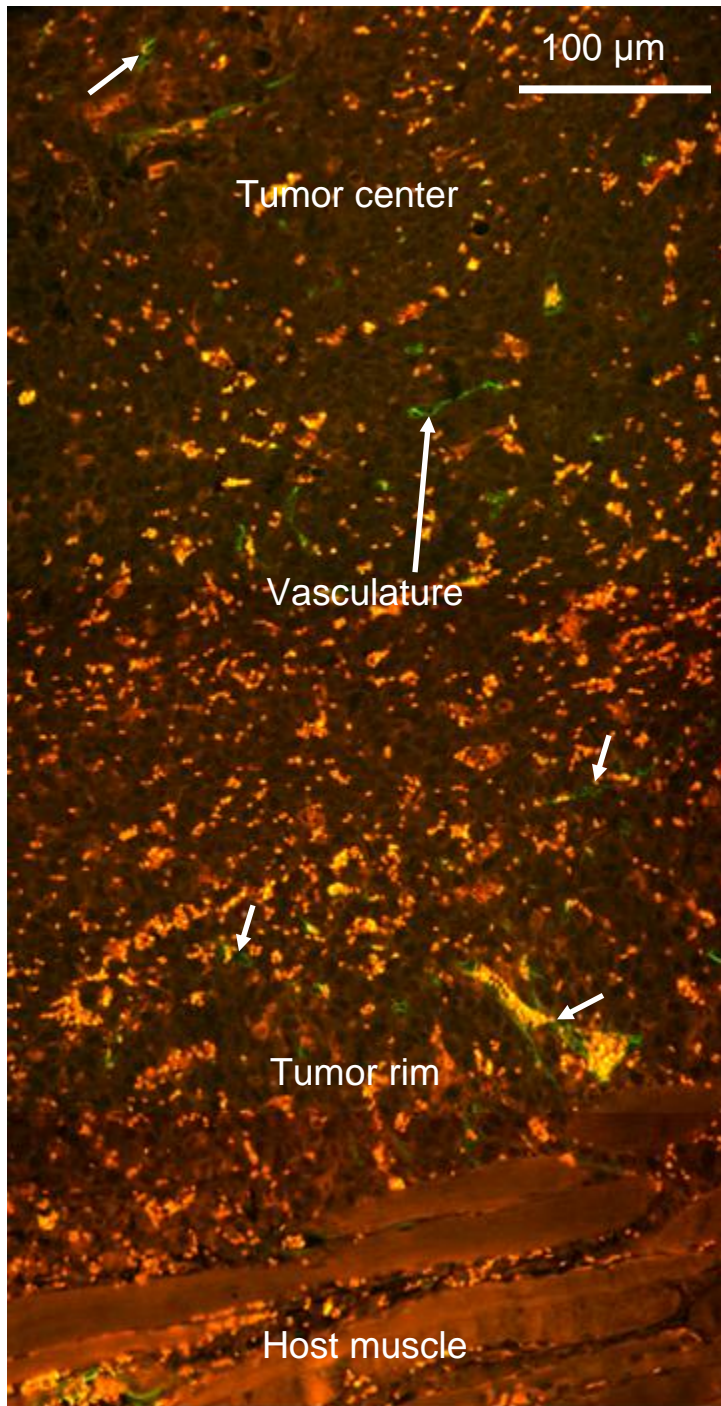


Figure 3-7. Example of MECA-32 staining for KHT-3. A continuous region of tissue is shown that shows the extent of vascularization at the tumor rim and tumor center at $\times 20$ magnification. The fluorescently green labeled areas (*arrows*) are the endothelial cells that line the vasculature.

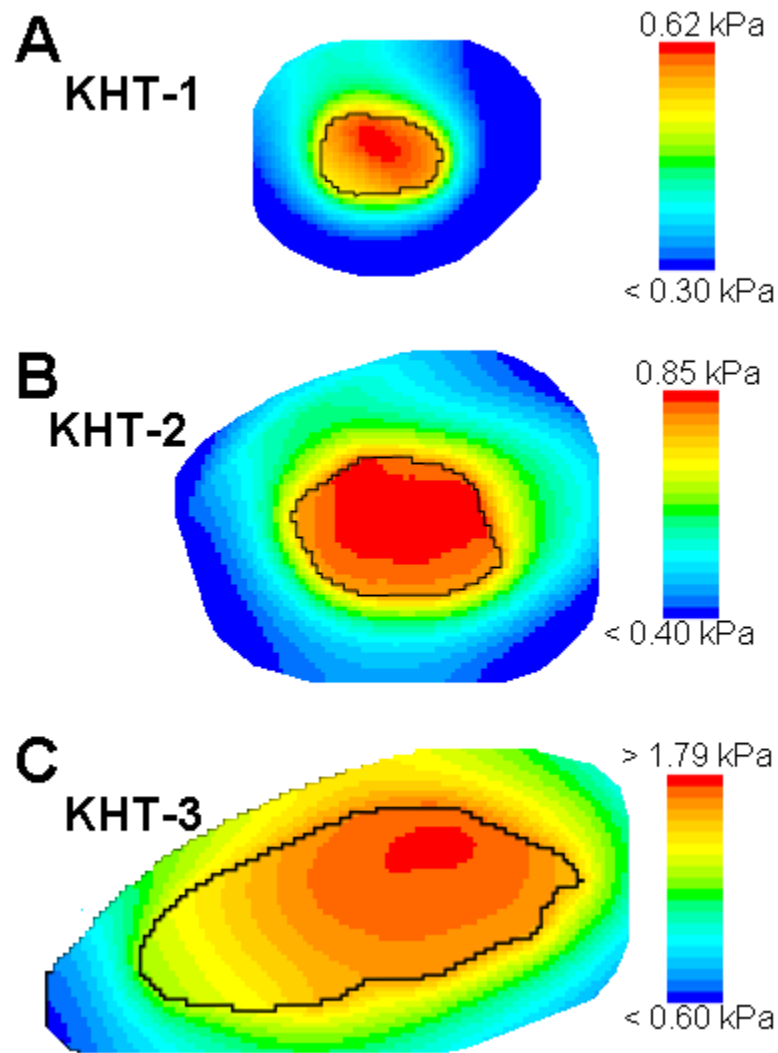


Figure 3-8. Interstitial fluid pressure for small KHT sarcomas. Pressure contours near tumor boundary (*black line*) of A) KHT-1, B) KHT-2, and C) KHT-3.

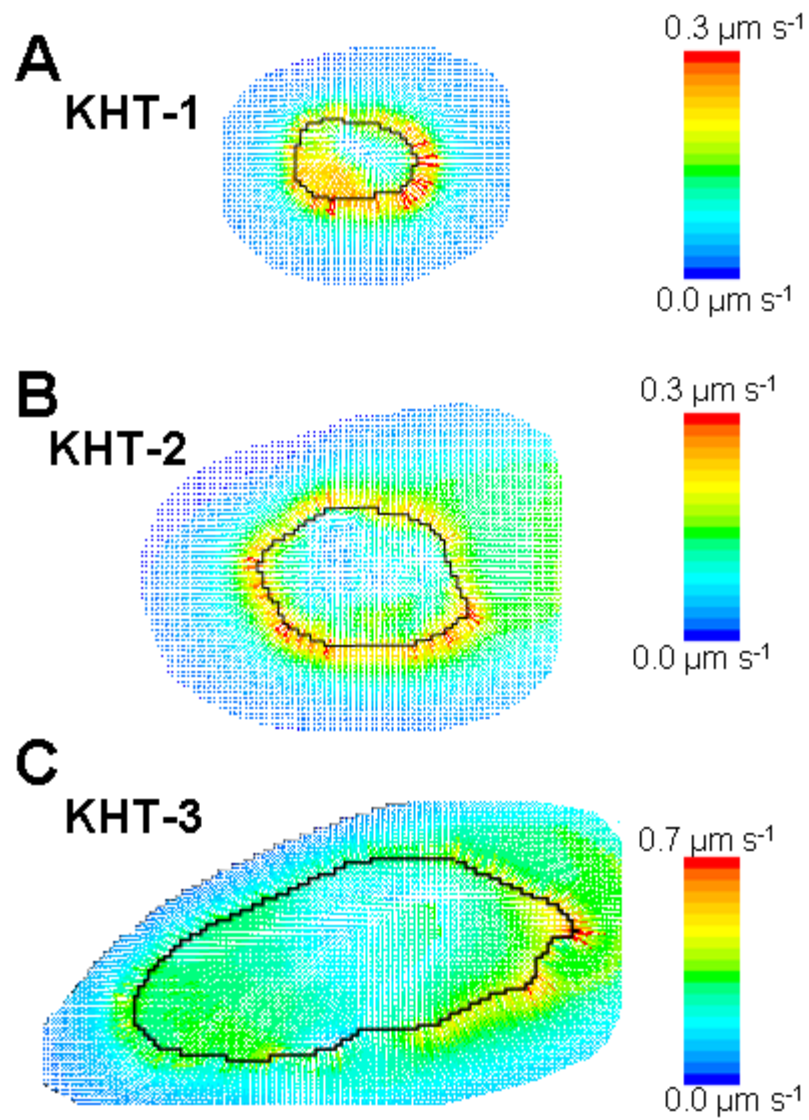


Figure 3-9. Interstitial fluid velocity for small KHT sarcomas. Velocity contours near tumor boundary (*black line*) of A) KHT-1, B) KHT-2, and C) KHT-3.

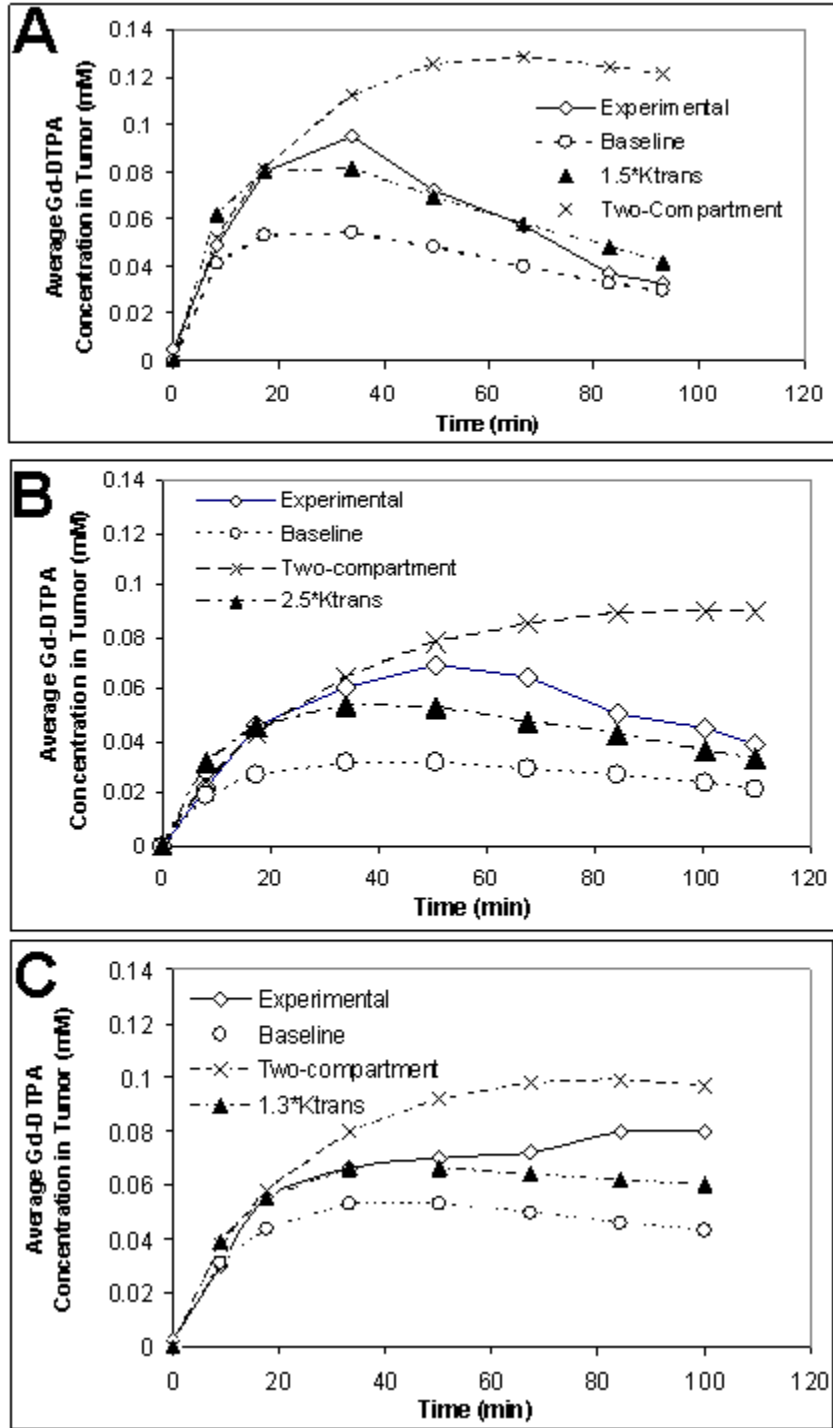


Figure 3-10. Comparison of simulated and experimental average Gd-DTPA in tumor. Time course of average concentration curves shown for A) KHT-1, B) KHT-2, and C) KHT-3. Porous media model and two-compartment model computed with $\phi = 0.2$.

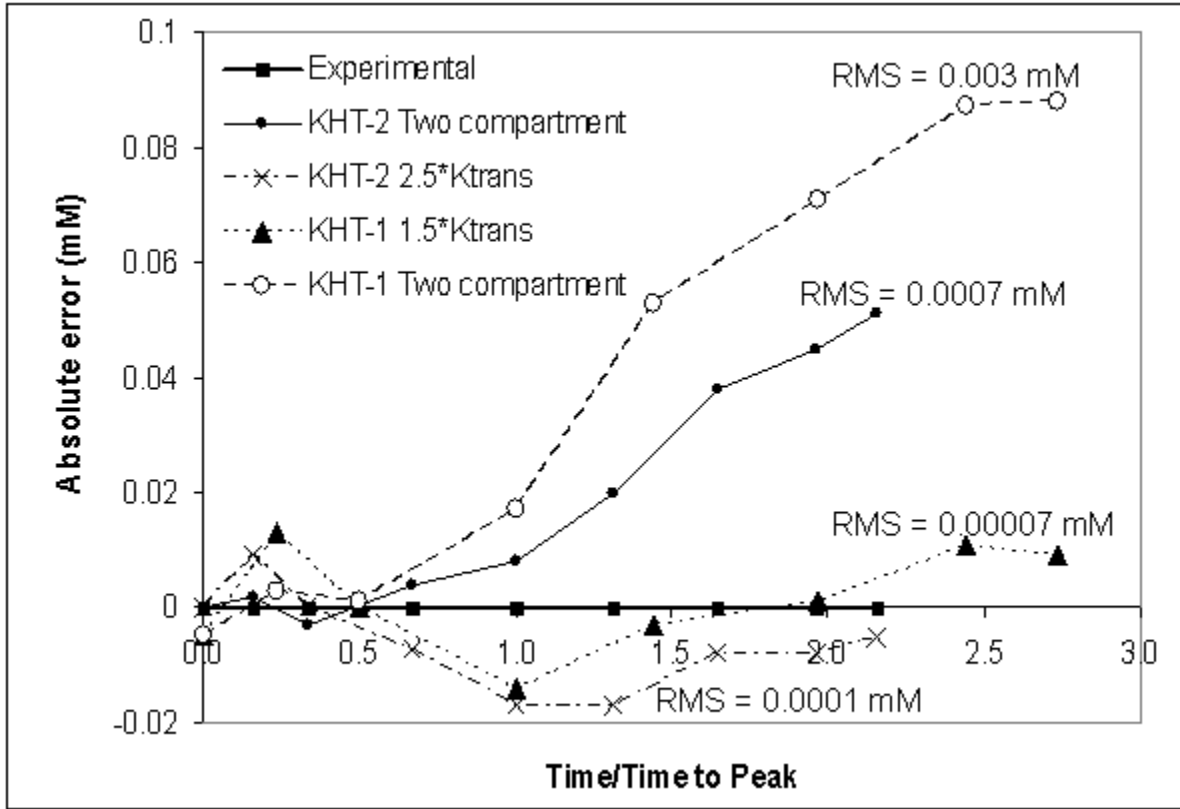


Figure 3-11. Comparison of error versus time quantified for simulations and experiment for KHT sarcomas. Root mean square (RMS) error is quantified. Porous media simulations resulted in lower RMS than the two-compartment model for KHT-1 and KHT-2. Absolute error versus time for KHT-3 is not shown (RMS = 0.1×10^{-3} for $1.3 \cdot K^{trans}$ case; RMS = 0.3×10^{-3} for two-compartment case).

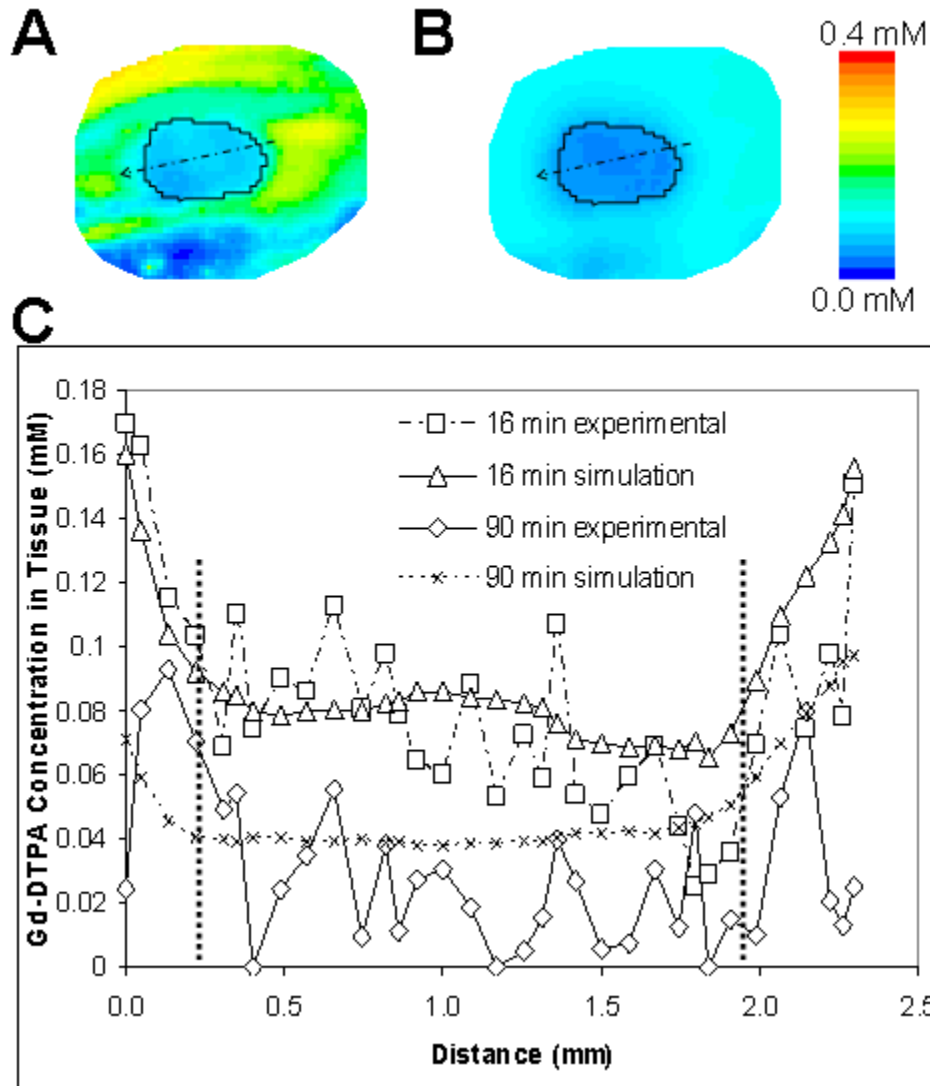


Figure 3-12. Simulated tracer transport for small KHT sarcoma (KHT-1). A) Gd-DTPA concentration distribution contours in KHT-1 (*black*) at an early time point ($t = 16$ min) and B) later time point ($t = 90$ min). C) Gd-DTPA concentration profile (*along dashed arrow*) comparing simulated and experimental tracer at an early and later time point across tumor boundary (*dotted line*).

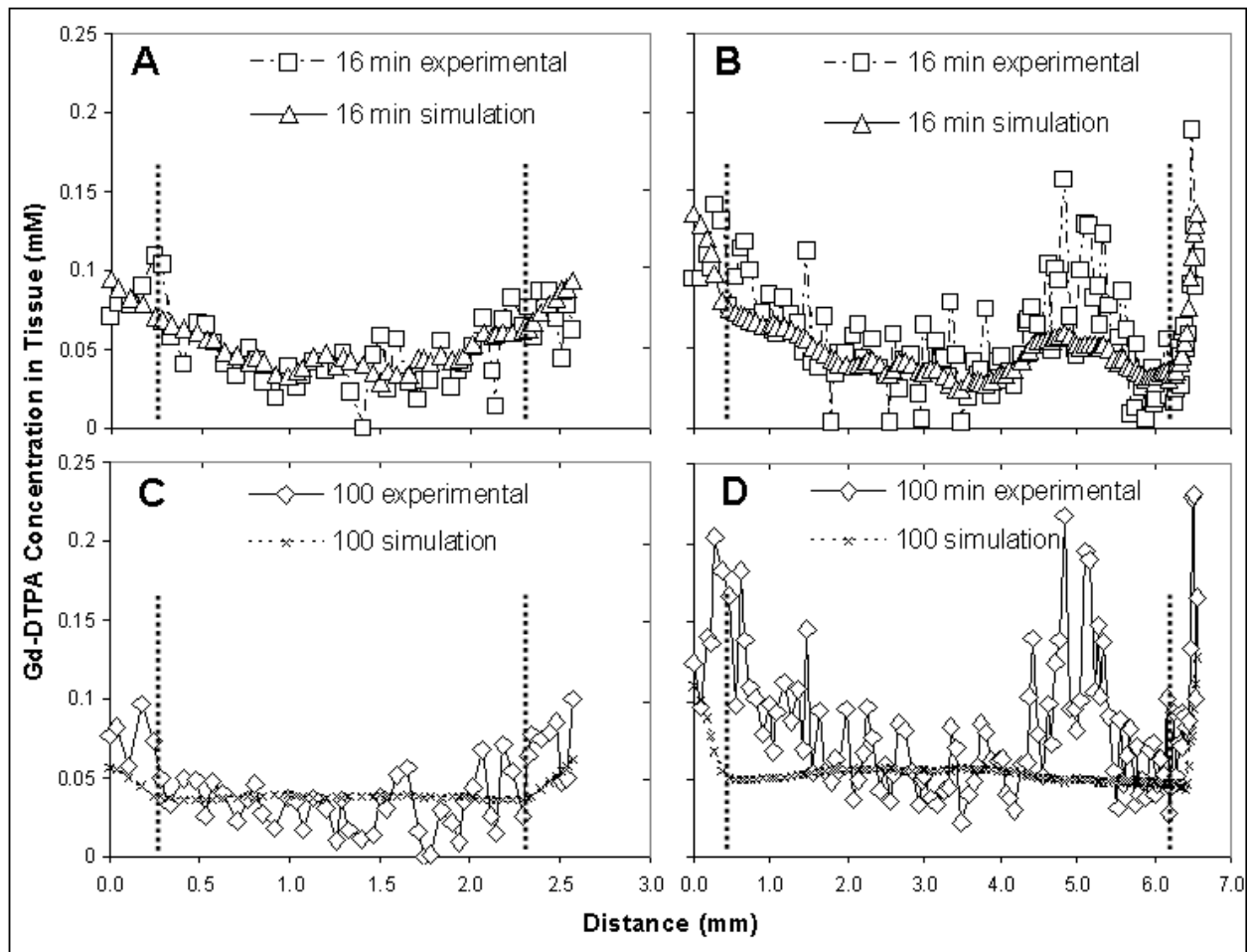


Figure 3-13. Comparison of experimental and simulated concentration profiles across small KHT sarcomas. Gd-DTPA distribution at early time points ($t = 16$ min) for A) KHT-2 and B) KHT-3 with the tumor boundary labeled (*dotted line*). Gd-DTPA distribution at later time points ($t = 100$ min) C) KHT-2 and D) KHT-3.

CHAPTER 4 PATIENT-SPECIFIC COMPUTATIONAL MODELS OF LARGE SOLID TUMORS: AN EXPERIMENTAL COMPARISON

4.1 Introduction

The previous chapter presented a validation study of a patient-specific tumor model for predicting interstitial fluid and tracer transport within small, non-necrotic tumors with low leakiness. This result revealed the importance of the 3D porous media model by accounting for the effects of convection and diffusion. Convection played an important role on the transient Gd-DTPA concentration behavior within tumors with low leakiness and constant porosities. The porous media model provided better peak and transient concentration behavior than the two compartment model when the modeled porosity was fixed at physiological value of 0.2. Furthermore, the interstitial fluid flow's role on reducing measured values of K^{trans} and porosity was elucidated. This chapter aims to investigate the application of the 3D porous media model in larger KHT sarcoma with greater tissue heterogeneity ($\geq 160 \text{ mm}^3$).

Larger tumors can complicate drug delivery due to the evolving nature of the tissue structure. As a tumor matures and grows larger, the vasculature at the tumor boundary has a more difficult time supplying distant cells in less vascularized regions with the proper concentration of oxygen and nutrients. The lack of oxygen and nutrients compromises the cell viability. An early study on this topic demonstrated the distance between vessels and cells to be a limiting factor for cell viability due to the increase diffusional distance required for oxygen and nutrients [87]. The lack of proper cell maintenance can often lead to necrosis. Necrosis is a slow cell death in which groups of cells swell to the point of bursting the cellular membrane leading to the discharge of cytotoxic intracellular content into the tumor environment causing an inflammatory

response in nearby tissue [88]. With healthy cells, phagocytes (white blood cells that ingest foreign particles) are signaled to clean up such harmful products, but necrotic cell death lacks these signaling capabilities leading to the accumulation of cellular debris. This cascade of events due to a growing tumor exacerbates the non-uniformity of the tumor environment.

The drug delivery difficulties that arise due to necrosis have been studied using mathematical models. Baxter and Jain predicted the effects that a necrotic core would have on interstitial and solute transport in spherical tumor geometry [13]. Because necrotic regions in tumor tissue can be described by lack of functioning blood vessels and lymph vessels, there is no transvascular exchange in these regions. This requires that necrotic tissue regions gain access to drug molecules from nearby vascularized viable tissue. Baxter and Jain's model demonstrated important phenomena. First, necrosis did not significantly reduce the central interstitial pressure of the tumor. Second, concentration of distributed solute was reduced in the tumor as a whole due to the necrotic region. Third, there existed a reservoir effect. At early times, there was little solute in the necrotic core. At later times, the outer tumor region had less solute concentration than the central necrotic region; solute in the outer tumor region was cleared by functional transvascular exchange and convection. Experimentally, the reservoir effect has been seen in lower molecular weight drugs (methotrexate, MW ~ 450) [89, 90], which have a shorter time scale for uptake, distribution, and washout than larger macromolecules. The importance of necrosis upon drug delivery was studied using a non-systemic delivery scenario by Smith and Humphrey [18]. They modeled infusion into a brain tumor with a necrotic core. The necrotic core lacked functioning

vasculature; hence, there was no transvascular exchange. Their model suggested that the presence of a necrotic core substantially increased the convective fluid velocity in its vicinity. More intuitive drug delivery difficulties in larger tumors have been shown by sparser solute sources that results in less dense K^{trans} maps [66, 91]. In many experimental cases, these sparser solute sources are indicative of reduced solute distribution to the tumor.

Magnetic resonance imaging (MRI) has been used to detect necrosis and associated phenomena. Necrotic regions have been characterized by T_2 relaxation time [92] as well as by using diffusion-weighted imaging (DWI) to calculate the apparent diffusion coefficient (ADC) [21, 67, 92, 93]. DWI allows for structural tissue information to be probed with the self-diffusion of water molecules. Expressly, DWI is an MRI technique that exploits the reduction in MR signal in biological tissues as water molecules move along a field gradient. DWI has been implemented for a number of tumor related applications: (1) the detection of tumors [94], (2) ability to distinguish tumor from surroundings [95], and (3) ability to differentiate viable and necrotic regions of tumors [67-69]. Non-MR methods of investigating tissue has shown reduced integrity of cells in necrotic regions [63]. The degradation of the cell matrix may increase the ability for water molecules to diffuse. Dynamic contrast enhanced (DCE)-MRI has been used to show the delayed and increased presence of MR visible tracer in necrotic regions [91].

This chapter aims to create an image-based model that accounts for patient-specific necrotic regions in conjunction with vascular permeability maps of the tumor rim. For the study in this chapter, heterogeneous tissue transport properties have been

accounted for by incorporating vascular permeability maps for an additional four large KHT sarcomas. Permeability maps and porosity maps were created based on uptake of Gd-DTPA in tissue at early time points using DCE-MRI. Segmentation of tumor boundaries was conducted based on ADC maps. ADC maps will be fluid-filled necrotic regions by which solute reduction and reservoir effects may be assessed for individual tumors with regions of necroses. MR determined tumor infiltration of the hind limb muscle and leakiness were assessed via histology, H&E and MECA 32 staining, respectively. A voxelized modeling approach was used to solve interstitial fluid and tracer transport for each of these specific tumors. As a part of this chapter, simulated tracer transport was compared to experimental tracer transport. Tracer transport was compared by quantifying peak tumor concentration, spatial distribution, and average uptake and washout behavior within the tumor. Larger tumors are susceptible to a wider variety of tissue heterogeneities than smaller tumors. Because of each tumor has unique characteristics such as size and leakiness, there is the potential to elucidate the role that such characteristics such might have on the relative importance of convection, diffusion, and transvascular exchange within the tumor.

4.2 Materials and Methods

4.2.1 Animal Preparation

Four C3H/HeJ female mice (Jackson Laboratories, Bar Harbor, ME) were inoculated with between 1×10^5 to 2×10^5 murine KHT sarcoma cells in the gastrocnemius muscle. Murine KHT sarcoma cells were provided by Dr. Dietmar Siemann's laboratory (University of Florida, Gainesville, FL). The tumor was grown for 8 to 9 days. During animal preparation and imaging, the mouse was anesthetized using a gas mixture of 98% oxygen, 2% isoflurane. The lateral tail vein was catheterized using a

Terumo SurFlo 24 Gauge $\times \frac{3}{4}$ " I.V. Catheter (Terumo Medical Corporation, Somerset, NJ) and given a 0.25 mmol/kg of body weight (bw) bolus tail vein injection of Gd-DTPA (Omniscan, GE Healthcare Inc., Princeton, NJ) CA at a constant rate (~ 0.4 ml/min, 0.23 ml). The animal experiment was governed by the principles of the Guide for the Care and Use of Laboratory Animals and approved by the University of Florida Institutional Animal Care and Use Committee (IACUC).

4.2.2 Magnetic Resonance Imaging (MRI)

The MRI experiment was performed using a Bruker Avance imaging console (Bruker NMR Instruments, Billerica, MA) connected to Magnex Scientific 11.1 T horizontal bore magnet system (Varian, Inc., Magnex Scientific Products, Walnut Creek California). Tumor-bearing hind limbs of four mice were placed in a 1.5 cm inside diameter transmit and receive, volume coil. A variable time for recovery (TR) SE sequence (TR = 5000, 2000, 1000, 500 and 350 ms, TE = 15 ms), was acquired for calculation of native tissue T_1 values used in CA concentration calculations. Serial DCE-MR images, consisting of T_1 -weighted SE sequence (2 averages, TR/TE, field of view (FOV), slices, matrix size, and, total acquisition time in table 4-1) were collected before and after CA administration.

DWI allows for structural tissue information to be probed with the self-diffusion of water molecules. For DWI, a diffusion-weighted SE sequence was used with the parameters in table 4-2 and two averages. Low-diffusion-weighted data were acquired in 6 directions, defined by the tessellation of an icosahedron on a unit hemisphere, and high-diffusion-weighted data were acquired in 21 directions. MR data was obtained at the Advanced Magnetic Resonance Imaging and Spectroscopy (AMRIS) facility in the McKnight Brain Institute (MBI) of the University of Florida.

Multiple-linear regression [96] was used to fit multi-slice diffusion-weighted images to obtain the water translational diffusion tensor, \mathbf{D}_e . A single component of the diffusion tensor, D_{eij} was determined by,

$$\ln[S(b)/S(0)] = -\sum b_{ij}D_{eij} \quad (4-1)$$

where b_{ij} is the diffusion weight factor; $S(b)$ is the b -dependent signal intensity; $S(0)$ is T_2 -weighted, proton-density dependent signal intensity in the absence of diffusion weighting. ADC was solved in each voxel by solving,

$$ADC = \frac{Tr(\mathbf{D}_e)}{3}. \quad (4-2)$$

4.2.3 Histology

After imaging sessions were completed, mice were euthanized and the tumor tissue on the lateral side of the tibia and fibula was resected. The histology and image acquisition protocol was followed as described in the histology section 3.2.3. Histology was conducted at the MBI Cell & Tissue Analysis Core (CTAC) with the aid of Marda Jorgensen and Jingya Zhang.

4.2.4 Image Segmentation

Segmentation of tumor tissue for the computational model was manually conducted (MATLAB v.7, Natick, MA) based on contrast differences in ADC maps ($n = 4$) from DWI. Tumor boundary was demarcated in ADC maps based on the observed ADC differences between tumor and muscle [67]. All of the tissue regions outside of the tumor were designated as host muscle in the model. High ADC regions ($\sim 1.59 \times 10^{-3} \text{ mm}^2 \text{ s}^{-1}$) within the tumor boundary were segmented [92].

4.2.5 Arterial Input Function, Vascular Permeability Maps, and Porosity Maps

Arterial input function, vascular leakiness (K^{trans}), and porosity was described based upon method in section 3.2.5.

4.2.6 3D Porous Media Mathematical and Computational Model

The 3D porous media mathematical model presented in chapter 2.2.4 was used to predict the steady-state interstitial fluid flow and transient Gd-DTPA distribution assuming the tissue as porous media.

Voxelized (Cartesian) meshes were used to store the spatially discretized porous media transport solutions (Figure 3-2). Rectangular volumes were created (Gambit, Fluent, Lebanon, NH) that corresponded to the exact dimensions of DCE-MRI data (field of view correspond to those in Table 4-1). Eight-node brick elements were used to create meshes between 205,931 (10 slices of MR data) and 383,910 (12 slices of MR data) nodal points. CFD software package (FLUENT 6.3, Fluent, Lebanon, NH) was used to solve porous media transport.

Tissue and transport properties in tumor and host muscle were assigned according to baseline values (Table 2-1) in FLUENT. Prediction of tumor tracer distribution was a two-step process. First, steady-state interstitial plasma fluid flow was solved (Equation 2-6). Then, tracer transport (Equation 2-8) was solved at later time points. No flux of interstitial fluid at the skin boundary was maintained by low hydraulic conductivity (two orders lower than muscle) and zero diffusivity, respectively, in the exterior cells (Figure 3-2C). Segmented regions of high ADC were assumed to be fluid-filled necrotic regions. They were considered to have no functioning blood or lymphatic vessels [13]. High ADC regions were defined with an increased diffusion coefficient ($1 \times$

$10^{-9} \text{ m}^2 \text{ s}^{-1}$) based on MRI diffusion experiments of Gd-DTPA in necrotic cyst fluid [91] and increased porosity (0.5).

4.3 Results

4.3.1 Segmentation, Leakiness, and Histology

The heterogeneous tissue structure of large KHT sarcomas was illustrated by the range of ADC values measured in regions of interest. ADC values in the tumor rim regions of interest (ROIs) for all subjects were lower than normal muscle and high ADC ROIs (Figure 4-1). High ADC regions ($\text{ADC} \geq 1.59 \times 10^{-3} \text{ mm}^2 \text{ s}^{-1}$) were present in all tumors but one tumor (KHT-5). Two large KHT sarcomas (KHT-4 and KHT-6) developed high ADC regions at the center of the tumor while one (KHT-7) developed an additional high ADC regions at the tumor rim. High ADC regions accounted for < 6% the total tumor volume. KHT-7 was found to be the largest (most mature tumor) of the four based on total segmented volume (895 mm^3) and most tumor infiltration observed in the H&E stain (area = $19.2 \pm 2.3 \text{ mm}^2$) in Figure 4-2. KHT-4, KHT-5, and KHT-6 showed less tumor infiltration in both the total segmented tumor volume (KHT-4: 557 mm^3 ; KHT-5: 160 mm^3 ; KHT-6: 392 mm^3) and area of tumor in the H&E stained-sections (KHT-4: $17.0 \pm 2.0 \text{ mm}^2$; KHT-5: $6.8 \pm 1.2 \text{ mm}^2$; KHT-6: $18.9 \pm 2.1 \text{ mm}^2$).

K^{trans} maps showed increased leakiness around the perimeter for all tumors, but leakiness was patchy within the tumor. Percentage of fitted voxel within tumors was (< 15%) for all tumors. Increased leakiness density (46% voxels were fitted) was observed near fluid-filled, high ADC regions subjects KHT-6 and KHT-7 (the high ADC region near the rim). MECA-32 staining revealed KHT-6 to have the most extensive vascularization, which showed higher vascular density towards the center (132 ± 91

vessels per mm^2) of the tumor than at the rim (18 ± 18 vessels per mm^2) (Figure 4-3). KHT-4 showed the opposite trend with higher vascularization observed at the tumor rim (23 ± 6 vessels per mm^2) than the tumor center (5 ± 8 vessels per mm^2). Labeled endothelial cells were sparse in tumors KHT-5 and KHT-7.

4.3.2 Interstitial Fluid Transport

Highest regions of interstitial fluid pressure were predicted to be within the tumor all four subjects (Figure 4-5). Peak pressures ranged from 1.9kPa (KHT-5) to 2.6 kPa (KHT-7). Broader regions of higher intratumoral pressure ($> 2.0\text{kPa}$) were predicted in three of the tumors (Figure 4-5A, 4-5C, and 4-5D). Additional localized tumor peaks were predicted within the tumors (Figure 4-5B and 4-5D) as well. These peaks ranged from 50–100% the magnitude of the broader pressure peaks. Pressure decreased from peak pressure regions with a gradient $0.10\text{--}0.15 \text{ kPa mm}^{-1}$ for all tumors.

Unique interstitial fluid flow patterns were observed in each tumor (Figure 4-6). All tumors showed increased fluid velocity ($0.7\text{--}0.8 \mu\text{m s}^{-1}$) and outward convection along the tumor boundary. One large sarcoma (KHT-6) showed a single central region (Figure 4-6C) of lower interstitial fluid velocity ($0.1 \mu\text{m s}^{-1}$) than the higher boundary velocities. The three other tumors (Figure 4-6A, 4-6B, and 4-6D) showed more complex interstitial flow patterns. Namely, these tumors had multiple low velocity regions within the tumor. Within the boundaries of these tumors there were distinct “point source” locations from where interstitial fluid radially emanated.

4.3.3 Tracer Transport

Experimental Gd-DTPA concentration behavior demonstrated the unique patterns of tracer distribution as well as some of the difficulties of systemic delivery to larger

tumors. All four subjects showed early uptake ($t \cong 5$ min) in the tumor periphery when compared with the tumor region. However, all tumors shared similar patterns of uptake in the tumor periphery, which was slow with the peak concentration (0.10–0.25 mM) being reached at $t \cong 40$ min. Within the tumor, peak concentration behavior showed more variation for a given tumor and between tumor experiments (Figure 4-7).

All experimental tumors showed regions where a peak concentration was reached followed by washout ($t > 50$ min). Peak concentrations were reached at $t \sim 50$ min for KHT-4 (Figure 4-7A) and KHT-5 (Figure 4-7B). A small region of KHT-4 (4% of tumor volume) showed slow and low uptake ($C_t \leq 0.01$ mM) with no washout over the course of the experiment. The highest and most homogeneous Gd-DTPA coverage (0.089 ± 0.051 mM) was observed in the smallest tumor of this animal group (KHT-5; Figure 4-7B). Gd-DTPA concentration within tumor tissue was lower and not as homogeneous for KHT-6 (0.031 ± 0.020 mM; Figure 4-7C) and KHT-7 (0.014 ± 0.038 mM; Figure 4-7D). Accumulation of Gd-DTPA was observed in the high ADC, necrotic regions within these lower uptake tumors (KHT-6 and KHT-7). Accumulation of tracer in the peripheral high ADC region of KHT-7 occurred immediately after the bolus injection where as accumulation occurred later ($t = 9$ min) in the central high ADC region of KHT-6. Peak concentrations were achieved at later time points ($t > 65$ min) than surrounding tissue in these high ADC regions for both KHT-6 (0.24 ± 0.17 mM at peak) and KHT-7 (0.22 ± 0.10 mM at peak).

Like the experimental tumor data, the porous media simulations showed noticeable uptake at the tumor periphery at early time points ($t = 5$ min). This was particularly true for KHT-4, KHT-5, and KHT-7 (Figure 4-8A, 4-8B, and 4-8D,

respectively). These tumors were predicted to contain large regions where the concentration was very low (< 0.005 mM) while peripheral concentration was higher (> 0.01 mM). Peripheral tissue concentration was high (> 0.01 mM) at early time points in KHT-6, but concentrations were also high in nearly all locations within the tumor (Figure 4-8C). Peak concentration at the tumor periphery was reached later ($t \cong 50$ min) than in experiment for all cases except one, KHT-7, at $t < 5$ min.

Simulations of the four tumors showed distinctive distribution characteristics. Because of the low concentrations in the center of the tumor at early time points, three of the tumors (KHT-4, KHT-5 and KHT-7) showed inward diffusion from the tumor rim towards the center. This type of inward diffusion was not visible in the experimental data. Over the course of 90 min, tissue concentration in the low concentration central regions increased to ~ 0.02 mM. KHT-5 had the most homogeneous coverage in the tumor with a 65% relative difference in peak (0.033 mM) and minimum concentration; however, the peak concentration in the tumor was underpredicted by more than twofold. Coverage was less complete for KHT-4. Even at the last simulated time point ($t = 90$ min), concentration in more than half the tumor was < 0.005 mM). No washout within the tumor of KHT-4 or KHT-5 was predicted over 90 min; however the washout outside the tumor boundary occurred at a rate of 0.07 mM min^{-1} . Inward diffusion was less significant for KHT-7. At $t = 90$ min, concentrations above 0.01 mM were predicted 3 mm from the tumor boundary. A growing circular concentration front was predicted within this tumor as well. This was an anomaly related to the high velocity point source predicted in the interstitial fluid flow (Figure 4-6D).

Accumulation of Gd-DTPA was underpredicted in the high ADC regions of KHT-6. Over the course of the 90 min simulation, concentration reached 0.04 mM. This tissue concentration was about 200% higher than the predicted tissue concentration in the surrounding tissue, but was 83% lower than the experimental measurement. Washout ($\sim 0.3 \text{ mM min}^{-1}$) occurred $t > 50 \text{ min}$ in the tissue surrounding the high ADC region but like the experiment, there was no washout. Unlike the experimental data, accumulation in the high ADC regions of KHT-4 and KHT-7 was not observed.

4.4 Discussion and Conclusions

Chapter 4 presents the application of the MR image-based model for multiple ($n = 4$) large necrotic tumors ($\geq 160 \text{ mm}^3$). Drug delivery modeling challenges are elucidated by the heterogeneous nature of the tissue structure as well as decreased density of solute sources (sparser K^{trans} maps). The tissue heterogeneity present in this tumor series is observed by ADC maps, which is indicative of heterogeneous water content within the tumor. Higher ADC regions were assumed to have a higher effective diffusivity and porosity due to the increased water content. While intratumoral K^{trans} maps were sparser than those in chapters 2 and 3, these models account for heterogeneous leakiness to predict interstitial hypertension and interstitial fluid motion. Interstitial fluid motion was directed outwards from the tumor boundary, but inward diffusion was observed in the porous media models. The porous media models underpredicted the Gd-DTPA concentrations within the tumors due in part to the sparseness of K^{trans} , which reduced the number of leaky sources within the tumor.

The model predicted inward diffusion in three of the tumors. In the model, regions of non-zero K^{trans} were Gd-DTPA sources within the tumor boundary, at the tumor rim.

Over time, the Gd-DTPA diffused inwards, in the opposite direction of outward flux of interstitial fluid motion. The interstitial velocity in the central region was low ($<0.1 \mu\text{m s}^{-1}$) such that transport of solute was diffusion dominant. It was difficult to confirm this phenomenon experimentally with these particular KHT sarcomas because of the noise present in the data, which made complicated the delineation of diffusion front. However, this phenomenon was observed in other DCE-MRI experiments with CAKI-1 renal cell carcinomas conducted by our group and in experimental tumors of other researchers [91].

The difference in magnitudes between predicted and experimental concentrations was a roadblock for validation. The large errors in concentration magnitude were likely due to the sparseness of K^{trans} mapping. The sparseness of the maps resulted in an underprediction of tracer sources, which lead to a reduced Gd-DTPA concentration within the tumor. Leakiness maps for larger KHT sarcomas were expected to be less dense towards the center of the tumor. Additionally, MECA-32 staining revealed low microvascular vessel density in these tumors; however, experimental Gd-DTPA distribution suggested the possibility of more tracer sources than the K^{trans} maps predicted. This factor could be compounded by underpredictions K^{trans} , which would lead to less uptake and slower transvascular washout. Noise in the concentration data was the likely culprit of the reduced properly fitted K^{trans} values. These model inputs are affected by the number of averages as well as the temporal and spatial resolution of the DCE-MRI sequence. Spatial and temporal resolution should be tailored to the expected behavior of the contrast agent. In the case of these low leakiness tumors, the number of averages of each scan can be increased to decrease noise.

Table 4-1. Dynamic contrast-enhanced magnetic resonance imaging parameters

Subject	Field of view (cm ³)	Slices	Matrix size	TR/TE (ms ms ⁻¹)
4	2.0 × 1.4 × 1.4	14	190 × 133	430/9.4
5	2.0 × 1.0 × 1.0	10	192 × 96	330/9.4
6	2.0 × 1.4 × 1.1	11	190 × 133	337/9.4
7	2.0 × 1.4 × 1.4	14	190 × 133	430/9.4

Table 4-2. Diffusion weighted imaging parameters

Subject	Field of View (cm ³)	Slices	Matrix Size	TE (ms)	Total acquisition time (min)	Low b (s mm ⁻²)	High b (s mm ⁻²)
4	2.0×1.4×1.4	14	190 × 133	31.7	89.8	77	583
5	2.0×1.0×1.0	10	100 × 50	21.5	33.8	70	520
6	2.0×1.4×1.1	11	100 × 70	21.5	47.3	70	520
7	2.0×1.4×1.4	14	100 × 70	21.5	47.3	70	520

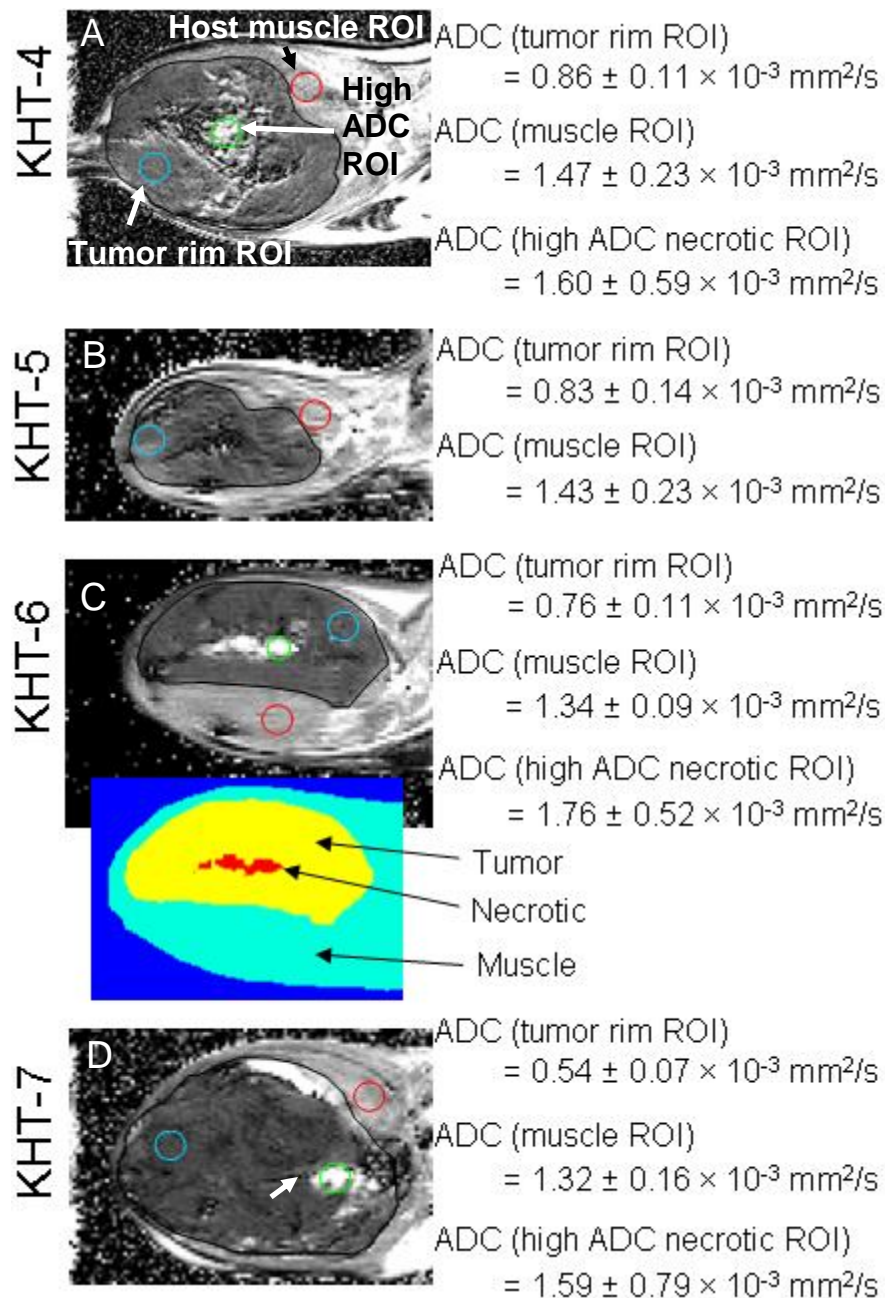


Figure 4-1. Tumor segmentation with corresponding H&E staining of small KHT sarcomas. Segmentation and H&E staining for A) KHT-4, B) KHT-5, C) KHT-6 with an example of segmented tissue zones, and D) KHT-7 with ADC values for tumor rim ROI (*blue*), high ADC necrotic ROI (*green*), and normal muscle (*red*). Tumors outlined in black. For H&E stains the purple indicates tumor cells, while the pink indicates host muscle.

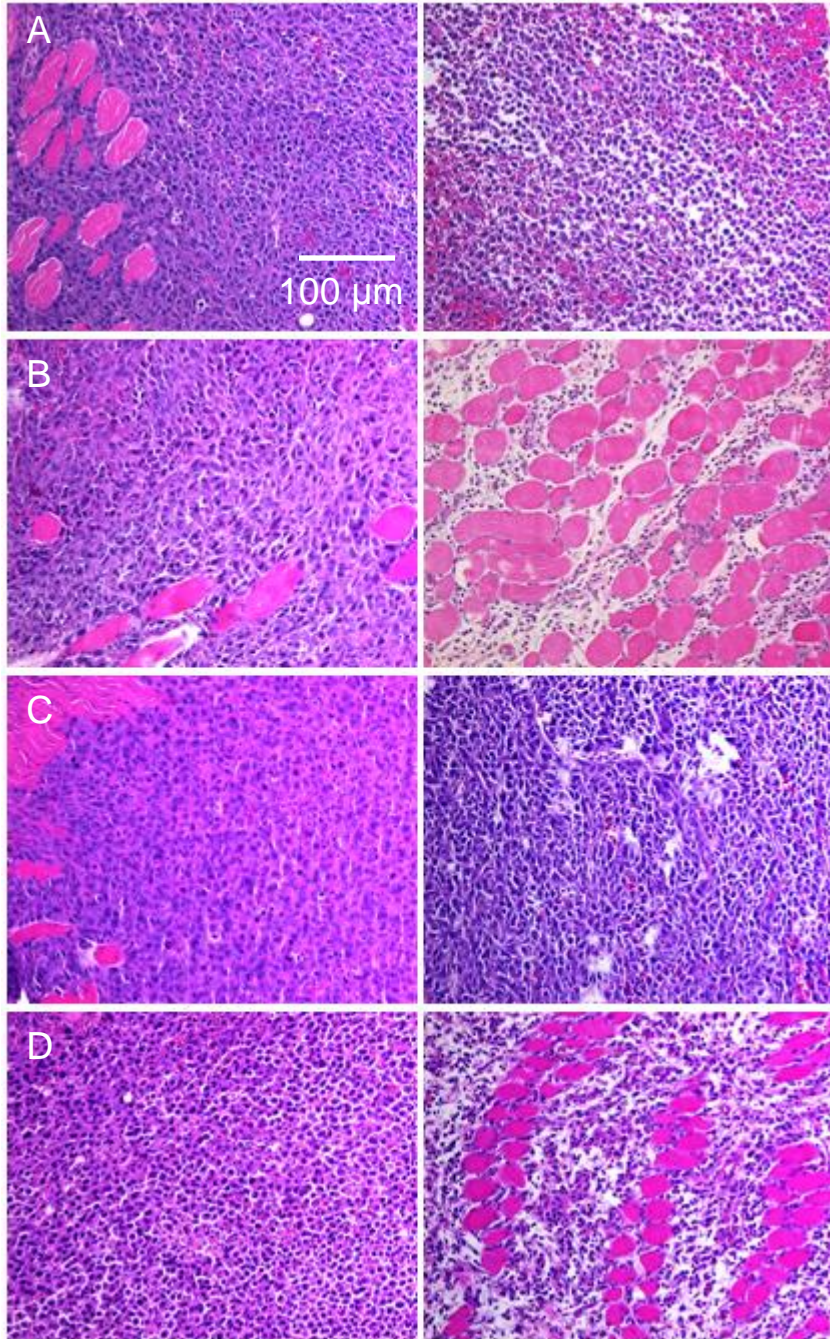


Figure 4-2. H&E staining of large KHT sarcomas for A) KHT-4, B) KHT-5, C) KHT-6, and D) KHT-7. Showing stained sections of the dense cellular tumor rim (*left panel*) and less dense regions toward the center (*right panel*).

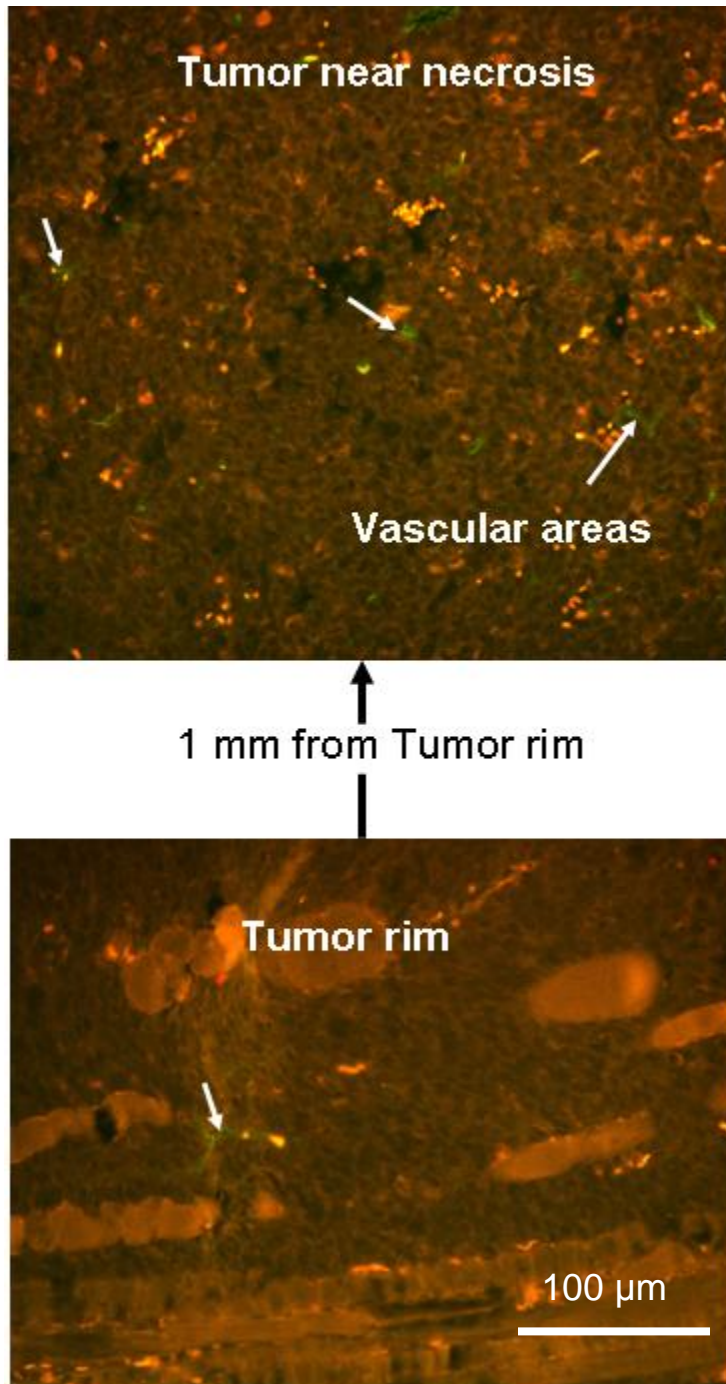


Figure 4-3. Example of MECA-32 staining for KHT-6. Two regions (near necrotic core and tumor rim) is shown that depicts the extent of vascularization in these regions at $\times 20$ magnification. The fluorescently green labeled areas (*arrows*) are the endothelial cells that line the vasculature. Region near the necrosis is more vascularized than the tumor rim.

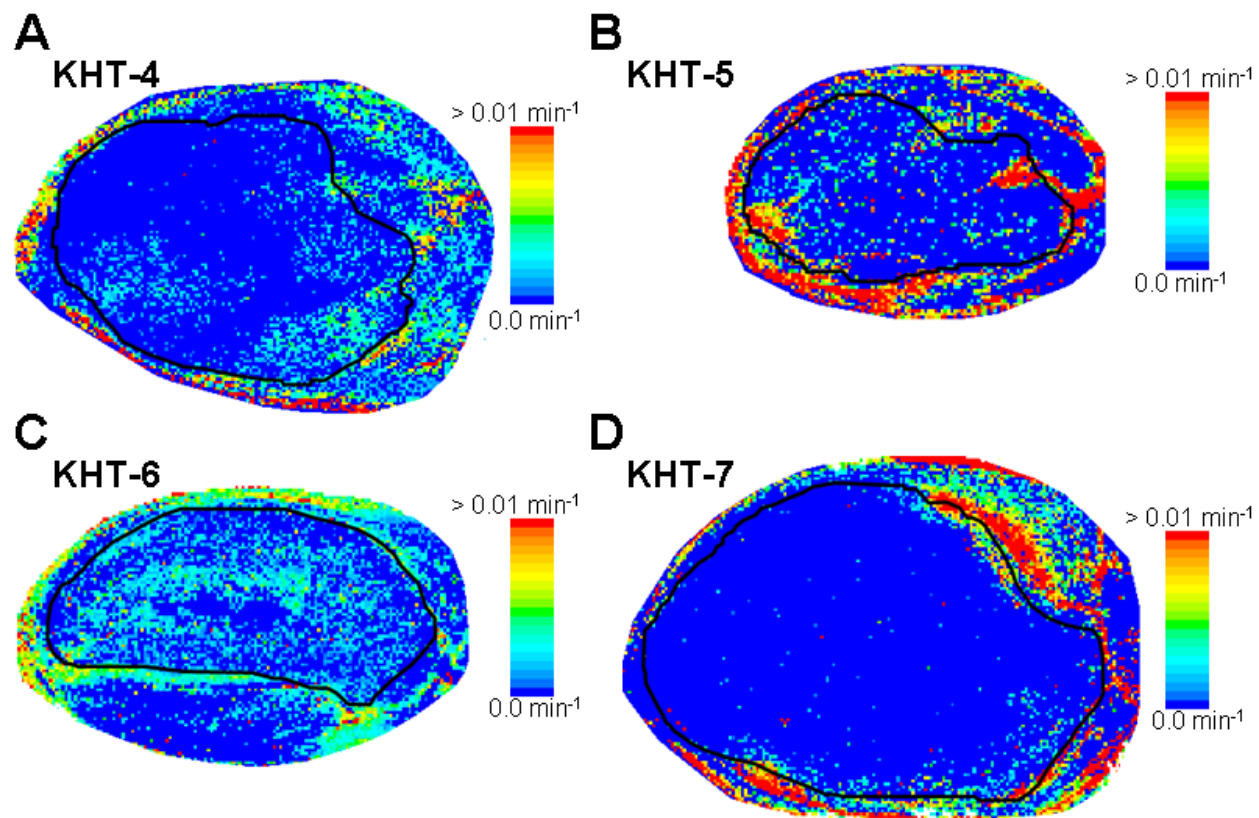


Figure 4-4. Leakiness (K^{trans}) maps of large KHT sarcomas. Maps for A) KHT-4, B) KHT-5, C) KHT-6, and D) KHT-7. Leakiness outside the tumor boundary (*black line*) is higher than inside the tumor boundary.

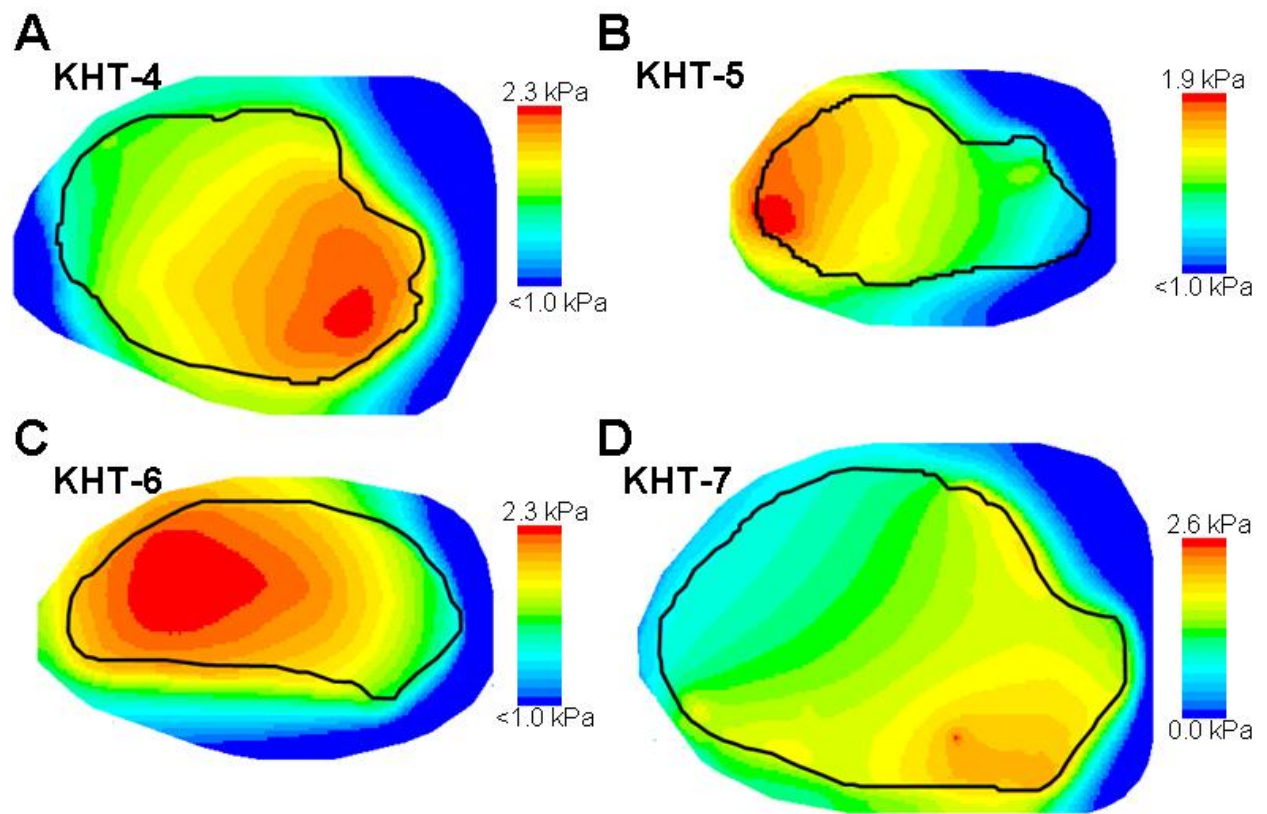


Figure 4-5. Interstitial fluid pressure for large KHT sarcomas. Pressure contours near tumor boundary (*black line*) of A) KHT-4, B) KHT-5, C) KHT-6, and D) KHT-7.

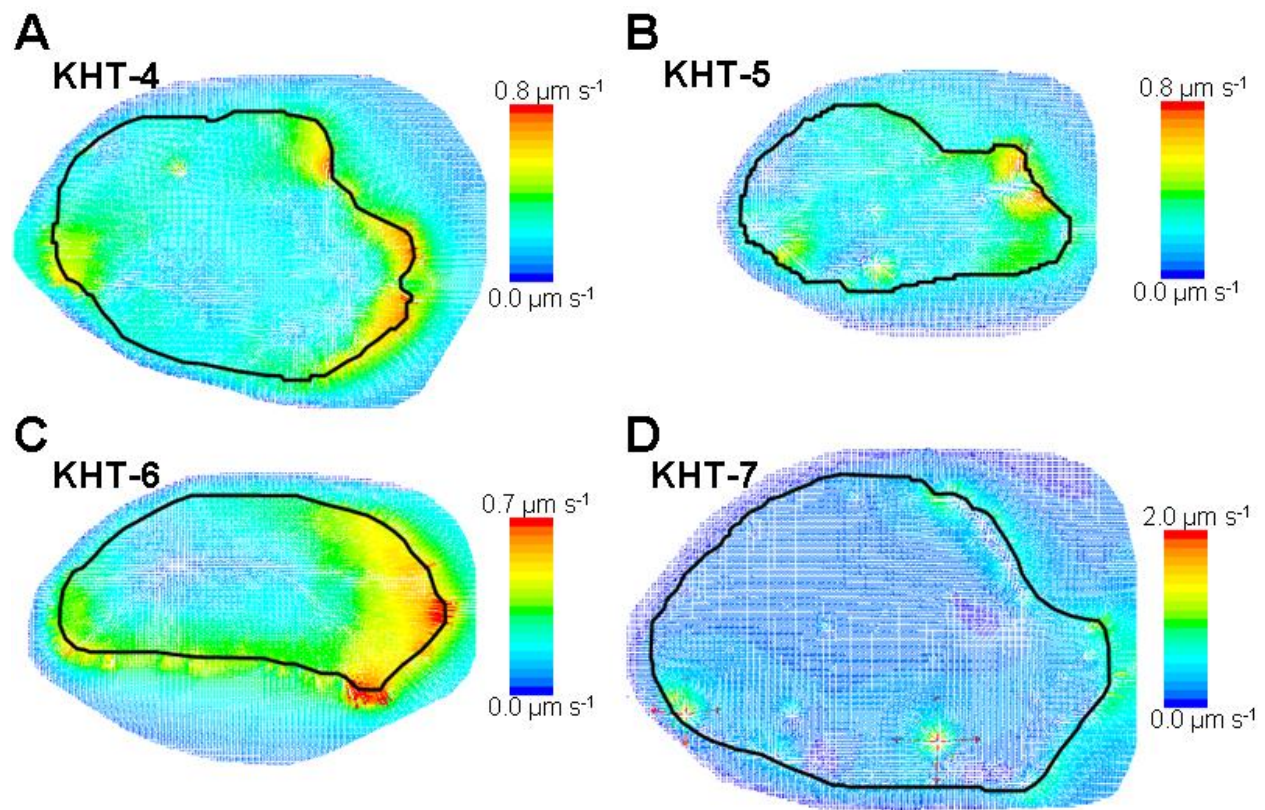


Figure 4-6. Interstitial fluid velocity for large KHT sarcomas. Velocity contours near tumor boundary (*black line*) of A) KHT-4, B) KHT-5, C) KHT-6, and D) KHT-7. A), B), and D) show complex pattern of interstitial fluid flow that occur due to localized point sources in the K^{trans} maps. C) shows a more conventional interstitial fluid flow patten with a region of low velocity near the central region and increasing velocity toward the tumor boundary.

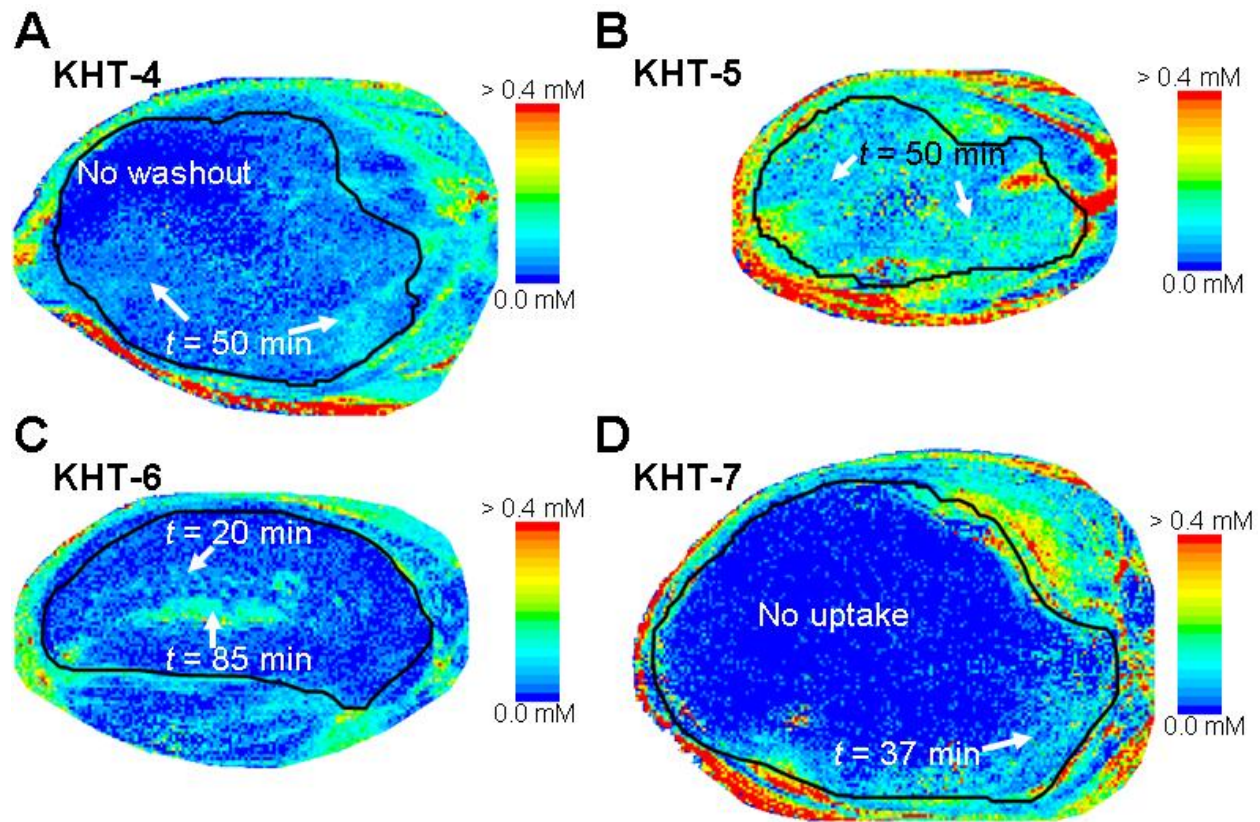


Figure 4-7. Experimental Gd-DTPA concentration, C_t , distribution in large KHT sarcomas at time equals 30 min. Peak times and locations shown within the tumor (*black line*) for A) KHT-4, B) KHT-5, C) KHT-6, and D) KHT-7. A) A tumor region of KHT-4 (4% of tumor volume) showed slow and low uptake ($C_t \leq 0.01$ mM) with no washout over the course of the experiment. B) The highest and most homogeneous coverage of Gd-DTPA concentration in the tumor (0.089 ± 0.051 mM) at peak concentration was observed in KHT-5. C) The high ADC region of KHT-6 accumulated tracer over the course of the experiment and reached a peak C_t (0.24 ± 0.17 mM). D) Significant region of no uptake (average $C_t < 0.008$ mM) was observed in tumor KHT-7 (20% of tumor volume).

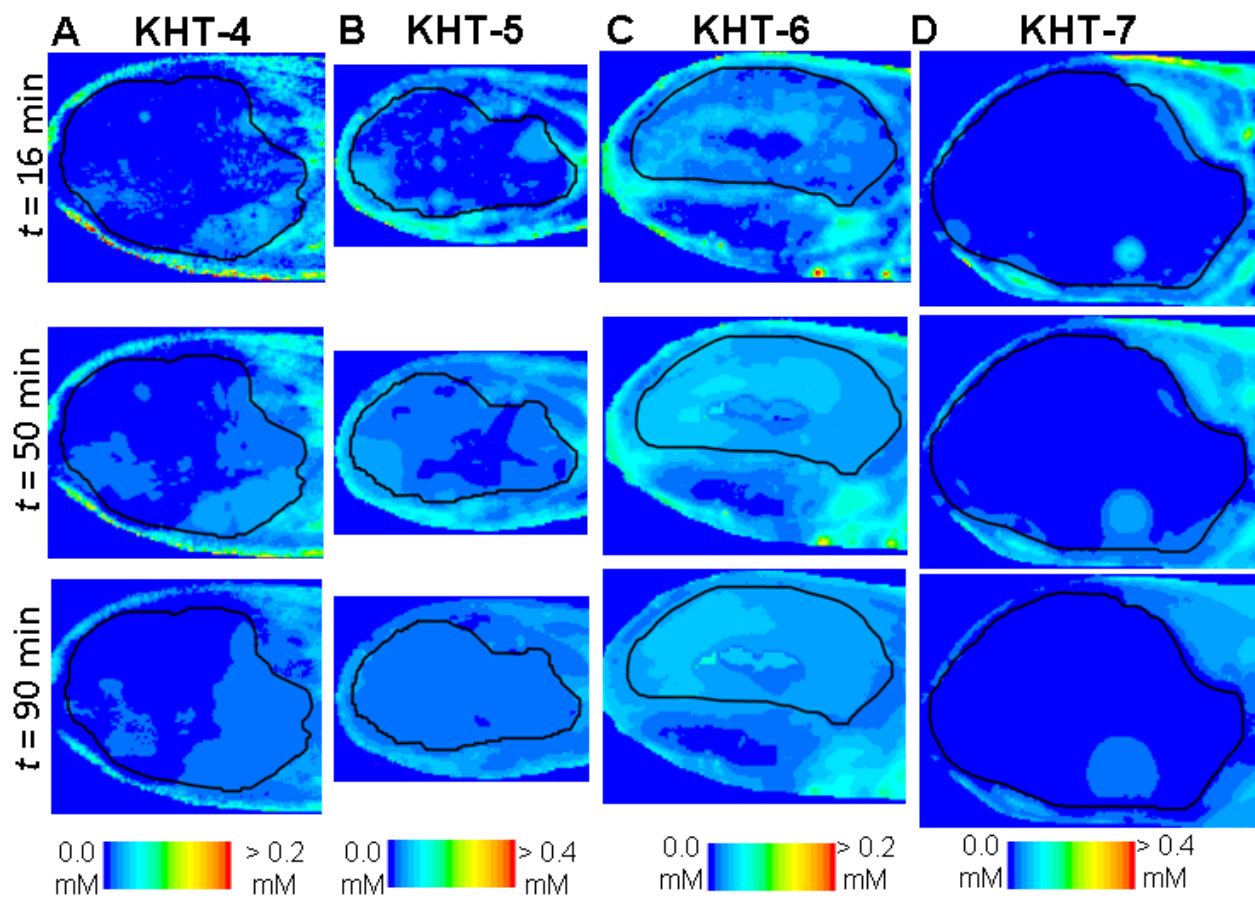


Figure 4-8. Simulated tracer transport for large KHT sarcomas. Distribution of Gd-DTPA within tumor boundary (*black*) at early ($t = 16$ min), intermediate ($t = 50$ min), and later ($t = 90$ min) time points for A) KHT-4, B) KHT-5 C) KHT-6, and D) KHT-7.

CHAPTER 5 CONCLUSIONS AND FUTURE WORK

The intent of this chapter is to recapitulate and unite the key concepts and contributions of the image-based modeling approach for solid tumors. An image-based solid tumor model may be used to optimize and evaluate treatment strategies for patient-specific therapies. An MRI-based porous media model has the ability to mathematically incorporate physiologically relevant transport characteristics such as spatially-varying transvascular exchange, diffusion, and convection, which affect the therapeutic levels of systemically drugs in both time and space. Because both the model and reality are the confluence of many physiological behaviors, it was the goal of the dissertation to investigate and validate positive predictive qualities of the image-based model as well as to delineate areas of refinement. The use of experimental data is quite a stride for the development of tumor models because it allows for the assessment of tracer distribution and transient behavior. These are the first necessary steps toward building more accurate models for clinical application.

The dissertation first presented a methodology for the first MRI-based tumor model that accounts for non-uniform distribution of solute by incorporating heterogeneous leakiness and extravascular volume fraction in a small KHT sarcoma with high leakiness. An appropriate arterial input function (AIF) was selected based on tumor volume-averaged Gd-DTPA uptake and washout behavior. The selection process showed that a slow AIF provided consistency between experimental and simulated uptake and washout in the tumor. The slow washout of Gd-DTPA in the plasma compartment was observed in this experimental setup using dynamic contrast enhanced magnetic resonance imaging (DCE-MRI). Sensitivity analysis was also

conducted on tissue and vascular transport parameters. The sensitivity analysis revealed that interstitial fluid pressure and velocity was more sensitive to changes in parameters than tracer transport for this KHT sarcoma, which implied the dominance of transvascular exchange. The model that was developed using one animal was used to simulate interstitial fluid and tracer transport for two additional KHT sarcomas. By comparing simulated and experimental Gd-DTPA distribution, concentration profiles were validated over the course of the experiment; however, there were concentration magnitude discrepancies at later time points, which was likely due to incorrect later time point AIF behavior or inaccurate predictions of interstitial flow. Even though errors in concentration magnitude existed, the overall transient behavior and concentration profiles were superior to previously presented image-based tumor models from our group. This promising result was contributed to the inclusion of porosity maps. It should be noted that DCE-MRI-derived porosity maps are susceptible to errors because the underlying interstitial fluid flow can affect the distribution and transient behavior of the MRI-calculated concentration curves leading to a possible underestimation of porosity. This concern is likely to be more significant with more mature tumors.

Small KHT sarcomas with more mature vasculature were observed to have slower leakiness. Slower leakiness made it difficult to obtain porosity maps by simultaneously fitting K^{trans} and ϕ with early time points ($t < 19$ min) of MR-derived *in vivo* concentration data. In order to have leakiness maps based on early time points, a fixed porosity was required. This is a potential limitation of using this “early time point” approach to obtaining K^{trans} and ϕ . As such, it was appropriate to understand and adapt the porous media model for this low leakiness scenario. Additionally, it allowed for the

model to be examined independent of spatial porosity changes or potentially erroneous porosities. In other words, it allowed for a more explicit investigation of the effects of convection and diffusion on tracer transient behavior and distribution.

This study showed a potential strength of the porous media model: the ability to account for clearance of tracer or drug due to convection and diffusion. The two-compartment model overpredicted average Gd-DTPA in the tumors at later time points. The baseline porous media model underpredicted this quantity, which was an important revelation. The underprediction showed that the interstitial fluid flow can affect the perceived values of K^{trans} and ϕ when tumors have low leakiness. This fact, unfortunately, adds more complexity to modeling this scenario, as it may be necessary to account for the decrease in K^{trans} value with a greater than unity scale factor. This highlights the point that there is not a particular set of parameters that can be applied to all tumors. In other words, there is no one-size-fits-all approach to modeling interstitial and solute transport in the presented KHT sarcomas. This study provided a model by which the underpredictions of K^{trans} and ϕ in DCE-MRI can be better understood. Furthermore, the methods employed in the study allow the comparison of experimental data to potentially quantify the underpredictions.

Large KHT sarcomas were observed to have heterogeneous vasculature and tissue. The MRI-based model was further developed to account for regions of high fluid-filled regions. Apparent diffusion coefficient (ADC) maps were used to detect and account for these fluid-filled regions into the model. Lower leakiness in these tumors made it difficult to obtain porosity maps. Furthermore, the decreased K^{trans} density complicated predictions of tracer distribution over time. Future models of larger tumors

that employ K^{trans} would be likely aided by reducing the noise in the data by either decreasing temporal resolutions or number of averages of the DCE-MRI scans. While K^{trans} density is lower in larger tumors than smaller tumors, these changes in MR parameters will lead to more accurate K^{trans} mapping and tumor interstitial fluid and tracer sources within the tumor.

This dissertation showed the development and application of an image-based modeling approach that incorporates more reality than previously presented models. The model was applied to three distinctly unique tumor scenarios: 1) small tumors with high leakiness, 2) small tumors with low leakiness, and 3) larger tumors with greater tissue heterogeneity. Positive steps have been made towards better understanding and predicting tracer transport in smaller tumors. At this point, models of larger tumors require greater refinement.

Despite some modeling shortcomings, this is the first attempt to test the porous media approach to modeling tumors and comparing predictions with experimental data. The study contained in this dissertation stands at a place where short-, intermediate-, and long-term goals should be established. For the short term, animal numbers for the small low leakiness tumors should be increased. Currently, a method for this tumor scenario has been developed. Increased animal numbers would help to determine the ability of the model to account for the potential underestimation of K^{trans} and ϕ at that particular stage of tumor growth. Currently, the model was validated for distribution of Gd-DTPA along a line through the tumor for young (6–7 days) KHT sarcomas. Transient response was validated for slightly more mature tumors (7–8 days). It is necessary to validate both spatial and transient behavior within a tumor. Two things will be necessary

to accomplish this. First, it is likely that animal-specific AIFs will be required. It may be sufficient to use the method of choosing AIF as presented in this dissertation. That is to vary the AIF, simulate transport for early time points, and select the best one based on average uptake and washout characteristics. It may be easier to obtain animal specific AIFs using MRI, though this too has its pitfalls. Obtaining animal-specific AIFs was attempted several times during experimental MR data acquisition for this dissertation. Major vessels in the tail and leg were imaged to little success. The MR spatial resolution of the mouse-tail was too low to discern a tail vein region of interest for AIF. Only one of many imaging sessions revealed vessel signal enhancement curves in the leg. Second, DCE-MRI independent methods for determining porosity distribution will be useful. Assuming a constant porosity throughout the tumor, due to the slow leakiness limitation, in chapter 3 decreased the detail of the Gd-DTPA concentration distribution curve along a bisecting tumor line. This made comparison of experimental and simulated distribution difficult. Employing ADC maps or T_2 maps will not provide quantitative porosity values but may provide the relative distribution of extravascular volume fraction. These porosity distribution patterns may be scaled to a realistic value (0.2–0.4) to provide more detail of the distribution curve.

The developed model utilized a low molecular weight tracer. An appropriate intermediate goal would be to employ the methods presented in this dissertation for large molecular weight tracer (e.g., Gd-Albumin). Larger molecular weight tracers will give clues into the transport characteristics of larger molecular weight drugs (e.g., monoclonal antibodies). Substituting a bolus injection of Gd-DTPA with Gd-Albumin could identically follow the methodology presented in this dissertation. Several

preliminary experiments using Gd-Albumin were conducted. Minimal extravasation of Gd-Albumin was observed with the KHT sarcomas on a thirty-minute time scale. It is recommended to use a different tumor model (e.g., MCF-7 breast cancer cell line) or to increase the time scale of observation (~2 h).

While the model requires further validation for all tumors sizes, a road map for a patient-specific model has been established. This road map gives promise to a long-term ambition: a clinical model that would customize chemotherapeutic dose based on an individual's tumor environment. This requires an addition of a binding degradation term in solute transport. The benefit is that a predictive model would allow for the reduction of imaging time, which can be expensive and uncomfortable. Additionally, cardiotoxicity and other negative systemic consequences could be limited and dose efficacy maximized.

LIST OF REFERENCES

- [1] Society, A. C., 2010, "Cancer Facts & Figures 2010," American Cancer Society, Atlanta, GA.
- [2] Dreher, M. R., Liu, W. G., Michelich, C. R., Dewhirst, M. W., Yuan, F., and Chilkoti, A., 2006, "Tumor Vascular Permeability, Accumulation, and Penetration of Macromolecular Drug Carriers," *J. Natl. Cancer Inst.*, **98**(5), pp. 335-344.
- [3] Young, J. S., Lumsden, C. E., and Stalker, A. L., 1950, "The Significance of the Tissue Pressure of Normal Testicular and of Neoplastic (Brown-Pearce Carcinoma) Tissue in the Rabbit," *J. Pathol. Bacteriol.*, **62**(3), pp. 313-333.
- [4] Boucher, Y., Baxter, L. T., and Jain, R. K., 1990, "Interstitial Pressure-Gradients in Tissue-Isolated and Subcutaneous Tumors - Implications for Therapy," *Cancer Res.*, **50**(15), pp. 4478-4484.
- [5] Boucher, Y., Kirkwood, J. M., Opacic, D., Desantis, M., and Jain, R. K., 1991, "Interstitial Hypertension in Superficial Metastatic Melanomas in Humans," *Cancer Res.*, **51**(24), pp. 6691-6694.
- [6] Gutmann, R., Leunig, M., Feyh, J., Goetz, A. E., Messmer, K., Kastenbauer, E., and Jain, R. K., 1992, "Interstitial Hypertension in Head and Neck Tumors in Patients - Correlation with Tumor Size," *Cancer Res.*, **52**(7), pp. 1993-1995.
- [7] Nathanson, S. D., and Nelson, L., 1994, "Interstitial Fluid Pressure in Breast-Cancer, Benign Breast Conditions, and Breast Parenchyma," *Ann. Surg. Oncol.*, **1**(4), pp. 333-338.
- [8] Milosevic, M. F., Fyles, A. W., and Hill, R. P., 1999, "The Relationship between Elevated Interstitial Fluid Pressure and Blood Flow in Tumors: A Bioengineering Analysis," *Int. J. Radiat. Oncol. Biol. Phys.*, **43**(5), pp. 1111-1123.
- [9] Heldin, C. H., Rubin, K., Pietras, K., and Ostman, A., 2004, "High Interstitial Fluid Pressure - An Obstacle in Cancer Therapy," *Nat. Rev. Cancer*, **4**(10), pp. 806-813.
- [10] Fyles, A., Milosevic, M., Pintilie, M., Syed, A., Levin, W., Manchul, L., and Hill, R. P., 2006, "Long-Term Performance of Hypoxia and IFP as Prognostic Factors in Cervix Cancer," *Radiother. Oncol.*, **80**(2), pp. 132-137.
- [11] Jain, R. K., and Baxter, L. T., 1988, "Mechanisms of Heterogeneous Distribution of Monoclonal-Antibodies and Other Macromolecules in Tumors - Significance of Elevated Interstitial Pressure," *Cancer Res.*, **48**(24), pp. 7022-7032.

- [12] Baxter, L. T., and Jain, R. K., 1989, "Transport of Fluid and Macromolecules in Tumors .1. Role of Interstitial Pressure and Convection," *Microvasc. Res.*, **37**(1), pp. 77-104.
- [13] Baxter, L. T., and Jain, R. K., 1990, "Transport of Fluid and Macromolecules in Tumors .2. Role of Heterogeneous Perfusion and Lymphatics," *Microvasc. Res.*, **40**(2), pp. 246-263.
- [14] Konerding, M. A., Miodonski, A. J., and Lametschwandtner, A., 1995, "Microvascular Corrosion Casting in the Study of Tumor Vascularity: A Review," *Scanning Microsc.*, **9**(4), pp. 1233-1243; discussion 1243-1244.
- [15] Swabb, E. A., Wei, J., and Gullino, P. M., 1974, "Diffusion and Convection in Normal and Neoplastic Tissues," *Cancer Res.*, **34**(10), pp. 2814-2822.
- [16] Elkareh, A. W., and Secomb, T. W., 1995, "Effect of Increasing Vascular Hydraulic Conductivity on Delivery of Macromolecular Drugs to Tumor-Cells," *Int. J. Radiat. Oncol. Biol. Phys.*, **32**(5), pp. 1419-1423.
- [17] Eikenberry, S., 2009, "A Tumor Cord Model for Doxorubicin Delivery and Dose Optimization in Solid Tumors," *Theor. Biol. Med. Model.*, **6**(16).
- [18] Smith, J. H., and Humphrey, J. A. C., 2007, "Interstitial Transport and Transvascular Fluid Exchange During Infusion into Brain and Tumor Tissue," *Microvasc. Res.*, **73**(1), pp. 58-73.
- [19] Tan, W. H. K., Wang, F. J., Lee, T., and Wang, C. H., 2003, "Computer Simulation of the Selivery of Etanidazole to Brain Tumor from PLGA Wafers: Comparison between Linear and Double Burst Release Systems," *Biotechnol. Bioeng.*, **82**(3), pp. 278-288.
- [20] Zhao, J., Salmon, H., and Sarntinoranont, M., 2007, "Effect of Heterogeneous Vasculature on Interstitial Transport within a Solid Tumor," *Microvasc. Res.*, **73**(3), pp. 224-236.
- [21] Deng, J., Rhee, T. K., Sato, K. T., Salem, R., Haines, K., Paunesku, T., Mulcahy, M. F., Miller, F. H., Omary, R. A., and Larson, A. C., 2006, "In Vivo Diffusion-Weighted Imaging of Liver Tumor Necrosis in the VX2 Rabbit Model at 1.5 Tesla," *Invest. Radiol.*, **41**(4), pp. 410-414.
- [22] Baudalet, C., Ansiaux, R., Jordan, B. F., Havaux, X., Macq, B., and Gallez, B., 2004, "Physiological Noise in Murine Solid Tumours Using T2*-Weighted Gradient-Echo Imaging: A Marker of Tumour Acute Hypoxia?," *Phys. Med. Biol.*, **49**(15), pp. 3389-3411.

- [23] Chen, X. M., Astarý, G. W., Sepulveda, H., Mareci, T. H., and Sarntinoranont, M., 2008, "Quantitative Assessment of Macromolecular Concentration During Direct Infusion into an Agarose Hydrogel Phantom using Contrast-Enhanced MRI," *Magn. Reson. Imaging*, **26**(10), pp. 1433-1441.
- [24] Radjenovic, A., Ridgway, J. P., and Smith, M. A., 2006, "A Method for Pharmacokinetic Modelling of Dynamic Contrast Enhanced MRI Studies of Rapidly Enhancing Lesions Acquired in a Clinical Setting," *Phys. Med. Biol.*, **51**(9), pp. N187-197.
- [25] Rozijn, T. H., van der Sanden, B. P., Heerschap, A., Creyghton, J. H., and Bovee, W. M., 1999, "Determination of In Vivo Rat Muscle Gd-DTPA Relaxivity at 6.3 T," *Magn. Reson. Mater. Phys.*, **9**(1-2), pp. 65-71.
- [26] Tofts, P. S., and Kermode, A. G., 1991, "Measurement of the Blood-Brain-Barrier Permeability and Leakage Space Using Dynamic MR Imaging .1. Fundamental-Concepts," *Magn. Reson. Med.*, **17**(2), pp. 357-367.
- [27] Khaled, A. R. A., and Vafai, K., 2003, "The Role of Porous Media in Modeling Flow and Heat Transfer in Biological Tissues," *Int. J. Heat Mass Tran.*, **46**(26), pp. 4989-5003.
- [28] Truskey, G. A., F. Yuan, and D.F. Katz, 2004, *Transport Phenomena in Biological Systems*, Pearson Prentice-Hall, Upper Saddle River, NJ, p. 710.
- [29] Pusenjak, J., and Miklavcic, D., 2000, "Modeling of Interstitial Fluid Pressure in Solid Tumor," *Simulat. Pract. Theory*, **8**(1-2), pp. 17-24.
- [30] Heilmann, M., Walczak, C., Vautier, J., Dimicoli, J. L., Thomas, C. D., Lupu, M., Mispelter, J., and Volk, A., 2007, "Simultaneous Dynamic T1 and T2* Measurement for AIF Assessment Combined with DCE MRI in a Mouse Tumor Model," *Magn. Reson. Mater. Phys.*, **20**(4), pp. 193-203.
- [31] Aref, M., Brechbiel, M., and Wiener, E. C., 2002, "Identifying Tumor Vascular Permeability Heterogeneity with Magnetic Resonance Imaging Contrast Agents," *Invest. Radiol.*, **37**(4), pp. 178-192.
- [32] Weinmann, H. J., Laniado, M., and Mutzel, W., 1984, "Pharmacokinetics of GdDTPA/Dimeglumine after Intravenous-Injection into Healthy-Volunteers," *Physiol. Chem. Phys. Med. N.M.R.*, **16**(2), pp. 167-172.
- [33] Diehl, K. H., Hull, R., Morton, D., Pfister, R., Rabemampianina, Y., Smith, D., Vidal, J. M., and van de Vorstenbosch, C., 2001, "A Good Practice Guide to the Administration of Substances and Removal of Blood, Including Routes and Volumes," *J. Appl. Toxicol.*, **21**(1), pp. 15-23.

- [34] Znati, C. A., Rosenstein, M., McKee, T. D., Brown, E., Turner, D., Bloomer, W. D., Watkins, S., Jain, R. K., and Boucher, Y., 2003, "Irradiation Reduces Interstitial Fluid Transport and Increases the Collagen Content in Tumors," *Clin. Cancer Res.*, **9**(15), pp. 5508-5513.
- [35] Boucher, Y., Brekken, C., Netti, P. A., Baxter, L. T., and Jain, R. K., 1998, "Intratumoral Infusion of Fluid: Estimation of Hydraulic Conductivity and Implications for the Delivery of Therapeutic Agents," *Brit. J. Cancer*, **78**(11), pp. 1442-1448.
- [36] Netti, P. A., Berk, D. A., Swartz, M. A., Grodzinsky, A. J., and Jain, R. K., 2000, "Role of Extracellular Matrix Assembly in Interstitial Transport in Solid Tumors," *Cancer Res.*, **60**(9), pp. 2497-2503.
- [37] Zhang, X. Y., Luck, J., Dewhirst, M. W., and Yuan, F., 2000, "Interstitial Hydraulic Conductivity in a Fibrosarcoma," *Am. J. Physiol.-Heart C.*, **279**(6), pp. H2726-H2734.
- [38] Guyton, A. C., Granger, H. J., and Taylor, A. E., 1971, "Interstitial Fluid Pressure," *Physiol. Rev.*, **51**(3), pp. 527-563.
- [39] Baish, J. W., Netti, P. A., and Jain, R. K., 1997, "Transmural Coupling of Fluid Flow in Microcirculatory Network and Interstitium in Tumors," *Microvasc. Res.*, **53**(2), pp. 128-141.
- [40] Zakaria, E. R., Lofthouse, J., and Flessner, M. F., 1997, "Fluid Loss from the Peritoneal Cavity is Dependent on Dilution and Washout of the Interstitial Matrix.," *J. Am. Soc. Nephrol.*, **8**, pp. A1350-A1350.
- [41] Guyton, A. C., Scheel, K., and Murphree, D., 1966, "Interstitial Fluid Pressure .3. Its Effect on Resistance to Tissue Fluid Mobility," *Cir. Res.*, **19**(2), pp. 412-419.
- [42] Fleischman, G. J., Secomb, T. W., and Gross, J. F., 1986, "Effect of Extravascular Pressure-Gradients on Capillary Fluid Exchange," *Math. Biosci.*, **81**(2), pp. 145-164.
- [43] Sevick, E. M., and Jain, R. K., 1991, "Measurement of Capillary Filtration Coefficient in a Solid Tumor," *Cancer Res.*, **51**(4), pp. 1352-1355.
- [44] Jain, R. K., Tong, R. T., and Munn, L. L., 2007, "Effect of Vascular Normalization by Antiangiogenic Therapy on Interstitial Hypertension, Peritumor Edema, and Lymphatic Metastasis: Insights from a Mathematical Model," *Cancer Res.*, **67**(6), pp. 2729-2735.
- [45] Fensterm, J. D., and Johnson, J. A., 1966, "Filtration and Reflection Coefficients of Rabbit Blood-Brain Barrier," *Am. J. Physiol.*, **211**(2), pp. 341-346.

- [46] Paulson, O. B., Hertz, M. M., Bolwig, T. G., and Lassen, N. A., 1977, "Filtration and Diffusion of Water Across the Blood-Brain Barrier in Man," *Microvasc. Res.*, **13**(1), pp. 113-124.
- [47] Fraser, P. A., Dallas, A. D., and Davies, S., 1990, "Measurement of Filtration Coefficient in Single Cerebral Microvessels of the Frog," *J. Physiol.*, **423**, pp. 343-361.
- [48] Kimura, M., Dietrich, H. H., Huxley, V. H., Reichner, D. R., and Dacey, R. G., 1993, "Measurement of Hydraulic Conductivity in Isolated Arterioles of Rat-Brain Cortex," *Am. J. Physiol.*, **264**(6), pp. H1788-H1797.
- [49] Rippe, B., and Haraldsson, B., 1987, "Fluid and Protein Fluxes across Small and Large Pores in the Microvasculature - Application of 2-Pore Equations," *Acta Physiol. Scand.*, **131**(3), pp. 411-428.
- [50] Victorino, G. P., Ramirez, R. M., Chong, T. J., Curran, B., and Sadjadi, J., 2008, "Ischemia-Reperfusion Injury in Rats Affects Hydraulic Conductivity in Two Phases that are Temporally and Mechanistically Separate," *Am. J. Physiol-Heart C.*, **295**(5), pp. H2164-H2171.
- [51] Pappenheimer, J. R., Renkin, E. M., and Borrero, L. M., 1951, "Filtration, Diffusion and Molecular Sieving through Peripheral Capillary Membranes a Contribution to the Pore Theory of Capillary Permeability," *Am. J. Physiol.*, **167**(1), pp. 13-46.
- [52] Bradbury, M. W. B., 1979, *The Concept of a Blood-Brain Barrier*, Wiley, Chichester, NY.
- [53] Hilmas, D. E., and Gillette, E. L., 1974, "Morphometric Analyses of the Microvasculature of Tumors During Growth and After X-Irradiation," *Cancer*, **33**(1), pp. 103-110.
- [54] Yuan, F., Leunig, M., Berk, D. A., and Jain, R. K., 1993, "Microvascular Permeability of Albumin, Vascular Surface Area, and Vascular Volume Measured in Human Adenocarcinoma LS174T Using Dorsal Chamber in SCID Mice," *Microvasc. Res.*, **45**(3), pp. 269-289.
- [55] Nicholson, M. L., Bailey, E., Williams, S., Harris, K. P., and Furness, P. N., 1999, "Computerized Histomorphometric Assessment of Protocol Renal Transplant Biopsy Specimens for Surrogate Markers of Chronic Rejection," *Transplantation*, **68**(2), pp. 236-241.

- [56] Kim, Y. R., Savellano, M. D., Savellano, D. H., Weissleder, R., and Bogdanov, A., Jr., 2004, "Measurement of Tumor Interstitial Volume Fraction: Method and Implication for Drug Delivery," *Magn. Reson. Med.*, **52**(3), pp. 485-494.
- [57] Mazel, T., Simonova, Z., and Sykova, E., 1998, "Diffusion Heterogeneity and Anisotropy in Rat Hippocampus," *Neuroreport*, **9**(7), pp. 1299-1304.
- [58] Donahue, K. M., Weisskoff, R. M., Parmelee, D. J., Callahan, R. J., Wilkinson, R. A., Mandeville, J. B., and Rosen, B. R., 1995, "Dynamic Gd-DTPA Enhanced MRI Measurement of Tissue Cell Volume Fraction," *Magn. Reson. Med.*, **34**(3), pp. 423-432.
- [59] Yankeelov, T. E., Cron, G. O., Addison, C. L., Wallace, J. C., Wilkins, R. C., Pappas, B. A., Santyr, G. E., and Gore, J. C., 2007, "Comparison of a Reference Region Model with Direct Measurement of an AIF in the Analysis of DCE-MRI Data," *Magn. Reson. Med.*, **57**(2), pp. 353-361.
- [60] Foy, B. D., and Blake, J., 2001, "Diffusion of Paramagnetically Labeled Proteins in Cartilage: Enhancement of the 1-D NMR Imaging Technique," *J. Magn. Reson.*, **148**(1), pp. 126-134.
- [61] Gordon, M. J., Chu, K. C., Margaritis, A., Martin, A. J., Ethier, C. R., and Rutt, B. K., 1999, "Measurement of Gd-DTPA Diffusion Through PVA Hydrogel Using a Novel Magnetic Resonance Imaging Method," *Biotechnol. Bioeng.*, **65**(4), pp. 459-467.
- [62] Pozrikidis, C., and Farrow, D. A., 2003, "A Model of Fluid Flow in Solid Tumors," *Ann. Biomed. Eng.*, **31**(2), pp. 181-194.
- [63] Jain, R. K., 1987, "Transport of Molecules Across Tumor Vasculature," *Cancer Metastasis Rev.*, **6**(4), pp. 559-593.
- [64] Hassid, Y., Furman-Haran, E., Margalit, R., Eilam, R., and Degani, H., 2006, "Noninvasive Magnetic Resonance Imaging of Transport and Interstitial Fluid Pressure in Ectopic Human Lung Tumors," *Cancer Res.*, **66**(8), pp. 4159-4166.
- [65] Milosevic, M., Fyles, A., Hedley, D., Pintilie, M., Levin, W., Manchul, L., and Hill, R., 2001, "Interstitial Fluid Pressure Predicts Survival in Patients with Cervix Cancer Independent of Clinical Prognostic Factors and Tumor Oxygen Measurements," *Cancer Res.*, **61**(17), pp. 6400-6405.
- [66] Furman-Haran, E., Grobgeld, D., and Degani, H., 1997, "Dynamic Contrast-Enhanced Imaging and Analysis at High Spatial Resolution of MCF7 Human Breast Tumors," *J. Magn. Reson.*, **128**(2), pp. 161-171.

- [67] Herneth, A. M., Guccione, S., and Bednarski, M., 2003, "Apparent Diffusion Coefficient: A Quantitative Parameter for In Vivo Tumor Characterization," *Eur. J. Radiol.*, **45**(3), pp. 208-213.
- [68] Lyng, H., Haraldseth, O., and Rofstad, E. K., 2000, "Measurement of Cell Density and Necrotic Fraction in Human Melanoma Xenografts by Diffusion Weighted Magnetic Resonance Imaging," *Magn. Reson. Med.*, **43**(6), pp. 828-836.
- [69] Maier, C. F., Paran, Y., Bendel, P., Rutt, B. K., and Degani, H., 1997, "Quantitative Diffusion Imaging in Implanted Human Breast Tumors," *Magn. Reson. Med.*, **37**(4), pp. 576-581.
- [70] Kim, J. H., Astary, G. W., Chen, X., Mareci, T. H., and Sarntinoranont, M., 2009, "Voxelized Model of Interstitial Transport in the Rat Spinal Cord Following Direct Infusion into White Matter," *J. Biomech. Eng.*, **131**(7), p. 071007.
- [71] Linninger, A. A., Somayaji, M. R., Erickson, T., Guo, X., and Penn, R. D., 2008, "Computational Methods for Predicting Drug Transport in Anisotropic and Heterogeneous Brain Tissue," *J. Biomech.*, **41**(10), pp. 2176-2187.
- [72] Sarntinoranont, M., Chen, X. M., Zhao, J. B., and Mareci, T. H., 2006, "Computational Model of Interstitial Transport in the Spinal Cord Using Diffusion Tensor Imaging," *Ann. Biomed. Eng.*, **34**(8), pp. 1304-1321.
- [73] Swartz, M. A., and Fleury, M. E., 2007, "Interstitial Flow and Its Effects in Soft Tissues," *Annu. Rev. Biomed. Eng.*, **9**, pp. 229-256.
- [74] Chang, S. F., Chang, C. A., Lee, D. Y., Lee, P. L., Yeh, Y. M., Yeh, C. R., Cheng, C. K., Chien, S., and Chiu, J. J., 2008, "Tumor Cell Cycle Arrest Induced by Shear Stress: Roles of Integrins and Smad," *Proc. Natl. Acad. Sci. U.S.A.*, **105**(10), pp. 3927-3932.
- [75] Boucher, Y., and Jain, R. K., 1992, "Microvascular Pressure is the Principal Driving Force for Interstitial Hypertension in Solid Tumors: Implications for Vascular Collapse," *Cancer Res.*, **52**(18), pp. 5110-5114.
- [76] Stohrer, M., Boucher, Y., Stangassinger, M., and Jain, R. K., 2000, "Oncotic Pressure in Solid tumors is Elevated," *Cancer Res.*, **60**(15), pp. 4251-4255.
- [77] Pishko, G. L., Astary, G. W., Mareci, T. H., and Sarntinoranont, M., 2009, "A Computational Model of Interstitial Transport in Murine Sarcoma with Heterogeneous Vasculature: A Sensitivity Analysis," ASME Summer Bioengineering Conference 2009, Lake Tahoe, CA.

- [78] Kim, J. H., Mareci, T. H., and Sarntinoranont, M., 2010, "A Voxelized Model of Direct Infusion into the Corpus Callosum and Hippocampus of the Rat Brain: Model Development and Parameter Analysis," *Med. Biol. Eng. Comput.*, **48**(3), pp. 203-214.
- [79] Magdoom-Mohammed, K. N., Pishko, G. L., Astary, G. W., Mareci, T. H., and Sarntinoranont, M., 2011, "Evaluation of a Voxelized Model for Tumor Transport based on DCE-MRI."
- [80] Pishko, G. L., Magdoom-Mohammed, K. N., Astary, G. W., Mareci, T. H., and Sarntinoranont, M., 2010, "MRI-Based Computational Model and Two-Compartment Models of Solid Tumors: Comparison of Predicted Distribution," 2010 BMES Annual Fall Meeting, Austin, TX.
- [81] Zhang, J., Zhang, G., Morrison, B., Mori, S., and Sheikh, K. A., 2008, "Magnetic Resonance Imaging of Mouse Skeletal Muscle to Measure Denervation Atrophy," *Exp. Neurol.*, **212**(2), pp. 448-457.
- [82] Morse, D. L., Galons, J. P., Payne, C. M., Jennings, D. L., Day, S., Xia, G., and Gillies, R. J., 2007, "MRI-Measured Water Mobility Increases in Response to Chemotherapy Via Multiple Cell-Death Mechanisms," *NMR Biomed.*, **20**(6), pp. 602-614.
- [83] Nielsen, T., Murata, R., Maxwell, R. J., Stodkilde-Jorgensen, H., Ostergaard, L., Ley, C. D., Kristjansen, P. E., and Horsman, M. R., 2010, "Non-Invasive Imaging of Combretastatin Activity in Two Tumor Models: Association with Invasive Estimates," *Acta Oncol.*, **49**(7), pp. 906-913.
- [84] Jakobsen, I., Lyng, H., Kaalhus, O., and Rofstad, E. K., 1995, "MRI of Human Tumor Xenografts In Vivo: Proton Relaxation Times and Extracellular Tumor Volume," *Magn. Reson. Imaging*, **13**(5), pp. 693-700.
- [85] Jain, R. K., 1987, "Transport of Molecules in the Tumor Interstitium - A Review," *Cancer Res.*, **47**(12), pp. 3039-3051.
- [86] Carmeliet, P., 2000, "VEGF Gene Therapy: Stimulating Angiogenesis or Angioma-genesis?," *Nat. Med.*, **6**(10), pp. 1102-1103.
- [87] Thomlinson, R. H., and Gray, L. H., 1955, "The Histological Structure of Some Human Lung Cancers and the Possible Implications for Radiotherapy," *Brit. J. Cancer*, **9**(4), pp. 539-549.
- [88] Scaffidi, P., Misteli, T., and Bianchi, M. E., 2002, "Release of Chromatin Protein HMGB1 by Necrotic Cells Triggers Inflammation," *Nature*, **418**(6894), pp. 191-195.

- [89] Goldacre, R. J., and Sylven, B., 1962, "On the Access of Blood-Borne Dyes to Various Tumour Regions," *Brit. J. Cancer*, **16**(2), pp. 306-322.
- [90] Jain, R. K., and Wei, J., 1977, "Dynamics of Drug Transport in Solid Tumors - Distributed Parameter Model," *J. Bioengineering*, **1**(4), pp. 313-329.
- [91] Dadiani, M., Margalit, R., Sela, N., and Degani, H., 2004, "High-Resolution Magnetic Resonance Imaging of Disparities in the Transcapillary Transfer Rates in Orthotopically Inoculated Invasive Breast Tumors," *Cancer Res.*, **64**(9), pp. 3155-3161.
- [92] Carano, R. A., Ross, A. L., Ross, J., Williams, S. P., Koeppen, H., Schwall, R. H., and Van Bruggen, N., 2004, "Quantification of tumor tissue populations by multispectral analysis," *Magn. Reson. Med.*, **51**(3), pp. 542-551.
- [93] Gibbs, P., Liney, G. P., Pickles, M. D., Zelhof, B., Rodrigues, G., and Turnbull, L. W., 2009, "Correlation of ADC and T2 Measurements with Cell Density in Prostate Cancer at 3.0 Tesla," *Invest. Radiol.*, **44**(9), pp. 572-576.
- [94] Ballon, D., Watts, R., Dyke, J. P., Lis, E., Morris, M. J., Scher, H. I., Ulug, A. M., and Jakubowski, A. A., 2004, "Imaging Therapeutic Response in Human Bone Marrow Using Rapid Whole-Body MRI," *Magn. Reson. Med.*, **52**(6), pp. 1234-1238.
- [95] Tsuruda, J. S., Chew, W. M., Moseley, M. E., and Norman, D., 1991, "Diffusion-Weighted MR Imaging of Extraaxial Tumors," *Magn. Reson. Med.*, **19**(2), pp. 316-320.
- [96] Basser, P. J., Mattiello, J., and LeBihan, D., 1994, "MR Diffusion Tensor Spectroscopy and Imaging," *Biophys. J.*, **66**(1), pp. 259-267.
- [97] Yang, C., Karczmar, G. S., Medved, M., and Stadler, W. M., 2004, "Estimating the Arterial Input Function Using Two Reference Tissues in Dynamic Contrast-Enhanced MRI Studies: Fundamental Concepts and Simulations," *Magn. Reson. Med.*, **52**(5), pp. 1110-1117.
- [98] Benjaminsen, I. C., Graff, B. A., Brurberg, K. G., and Rofstad, E. K., 2004, "Assessment of Tumor Blood Perfusion by High-Resolution Dynamic Contrast-Enhanced MRI: A Preclinical Study of Human Melanoma Xenografts," *Magn. Reson. Med.*, **52**(2), pp. 269-276.

BIOGRAPHICAL SKETCH

Greg Pishko spent most of his life in Florida. His formative years were spent at Atlantic Community High School, where he discovered a predilection for science. In 2006, he obtained a B.S. in aerospace engineering from the University of Florida, free from debt, thanks to his great parents and the friendly lottery players.

In graduate school, he took a turn for the bioengineering world, in order to avoid entanglement with the military-industrial complex—mission accomplished.